MANY-BODY DIPOLE INTERACTIONS

Jesús V. Hernández

A Dissertation

Submitted to

the Graduate Faculty of

Auburn University

in Partial Fulfillment of the

Requirements for the

Degree of

Doctor of Philosophy

Auburn, Alabama
August 9, 2008

Many-body dipole interactions

Except where reference is made to the work of others, the work described in this dissertation is my own or was done in collaboration with my advisory committee. This dissertation does not include proprietary or classified information.

Jesús V. Hernández

Certificate of Approval:

Michael S. Pindzola
Professor
Physics

Francis Robicheaux, Chair
Professor
Physics

Allen Landers
Associate Professor
Physics

Stuart Loch
Associate Professor
Physics

George T. Flowers
Interim Dean, Graduate School

Many-body dipole interactions

Jesús V. Hernández

Signature of Author

Date of Graduation

DISSERTATION ABSTRACT

MANY-BODY DIPOLE INTERACTIONS

Jesús V. Hernández

Doctor of Philosophy, August 9, 2008
(B.S., Kansas State University, 2003)

143 Typed Pages

Directed by Francis Robicheaux

This dissertation presents the study of controllable but strong long-range interaction between dipoles. In particular, we investigate the excitation and interaction between atoms in a cold gas where the collisional time is much greater than the interaction time between neighboring Rydberg atoms. In addition to quantum systems, we also examine the excitation properties of a collection of classical electric dipoles created by optically driving metallic nanospheres. We use various theoretical techniques to simulate these systems, including the direct numerical solutions to Schrödinger's equation, a Monte Carlo method, and a simple coupled point-dipole model.

We first perform simulations involving the excitation of a collection of cold atoms to Rydberg states. When the interaction energy between excited atoms is large enough to shift multiply-excited states out of resonance with the tightly tuned excitation laser, the number of atoms able to be excited is suppressed, creating a dipole blockade effect. The blockade effect offers exciting possibilities in the control of quantum bits, which is crucial for the development of quantum computing. We also examined the effects of density variation with respect to the the dipole blockade with three different models.

We then simulate the coherent interactions between Rydberg atoms. If the atoms are excited into states where the dipole-dipole interaction between them allows for resonant energy transfer to occur, then one state can freely hop from one atom to the next via the dipole-dipole interaction. We generated band structures for one, two, and three dimensional lattices and characterized the nature of the coherent hopping. This hopping is also studied in both a perfect and non-perfect lattice case which should be possible to examine experimentally.

Next, we simulate the effect of special excitation pulses on a cold gas of atoms. First a rotary echo sequence is used to examine the coherent nature of a frozen Rydberg gas. If collective excitation and de-excitation is present with little or no source of dephasing, after these pulses the system should be returned to a state with few excitations, and a strong echo signal should occur. We investigate systems that should display a perfect echo and systems where the interaction between atoms reduces the echo signal. A spin echo sequence is also used on a system of coherent hopping excitations, and we simulate how the strength of a spin echo signal is affected by thermal motion.

Finally, we describe the dipole-dipole interactions between a linear array of optically driven metallic nanospheres. These classical model calculations incorporate the full electric field generated by an oscillating electric dipole. The effects due to retardation of the generated electric field must be taken into account and several interesting effects are explored such as the ability to preferentially excite specific nanospheres.

Acknowledgments

First and foremost, I must thank my advisor Prof. Francis Robicheaux for his patience, guidance, and support during all of my graduate work. I would also like to thank him for it making possible for me study and learn physics at a higher level. Without his sincere efforts and willingness to help me whenever I showed up at his door, I doubt I would have this opportunity to thank him now.

I am obliged to the other members of my advisory committee, Prof. Michael S. Pindzola, Prof. Allen Landers, and Prof. Stuart Loch for their time and insightful suggestions towards the completion of this work. I knew during my time at Auburn I could get help from any one of them at any time, and the welcoming atmosphere helped foster a great learning experience.

I would be remiss if I didn't thank my parents Jesús and Debra Hernández for instilling in me a sense of joy in discovery, and for always being there when I needed them. I would also like to thank my sisters, Nica and Julia for putting up with me for all of these years.

I must also thank Jessica Williams for her tireless editing efforts and always believing in me.

Finally I would like to thank the National Science Foundation for their financial support of the research presented in this dissertation.

Style manual or journal used Journals of the American Physical Society (together with the style known as "auphd"). Bibliograpy follows the style used by the American Physical Society.

Computer software used The document preparation package TEX (specifically LATEX) together with the departmental style-file `auphd.sty`.

TABLE OF CONTENTS

LIST OF FIGURES

Chapter 1

Introduction

A Rydberg atom is characterized by the high principal quantum number, n, of the valence electron and its resultant exaggerated properties [1]. Since the size of the electron's orbit increases as n^2, the size of a Rydberg atom can become quite large. This large separation from the nucleus makes the electron highly sensitive to external electric fields and enables Rydberg atoms to support large electric dipole moments. The interplay between the dipole moments of Rydberg atoms has been an active topic of study for the last few decades, from early experiments observing resonant Rydberg-Rydberg collisions [2] and spectral line broadening [3] to its possible use in creating a quantum computer [4–7]. Additional advancements in laser cooling and trapping have also allowed for the investigation of Rydberg-Rydberg interactions without having to compensate for the effects of thermal motion [8, 9] creating a frozen Rydberg gas which has offered unprecedented experimental control over large collections of atoms. The ability to actively control strongly correlated quantum systems allows for the exploration of the fundamental nature of many-body physics and opens the door for various applications in quantum computing [10].

The large charge separation between the highly excited valence electron of a Rydberg atom and positively charged core leads to a large dipole moment that scales as n^2 [1]. If the dipoles are directly induced by a static electric field, the interaction between dipole moments is a first order one. In this case, the potential between dipole moments falls off as $1/R^3$, faster than the $1/R$ nature of the Coulomb potential between charges, however because the dipole moment grows as n^2, the first order interaction between Rydbergs can be increased or decreased by a factor of n^4. In the absence of an electric field it is possible for two excited atoms to experience a second order force (van der Waals) by inducing dipole moments on each other. Using standard second order perturbation theory, the van der Waals interaction will fall off as $1/R^6$ and scale as n^{11} [11]. In either case, experimentalists are able to precisely control the long range forces between cold atoms by changing the density of the trapped gas and the principal quantum number of atoms [12].

1.1 Dipole blockade

Two advantages of the interaction between dipole moments of Rydberg atoms are its controllable strength and long-range nature. Under certain conditions, the finely tuned excitation of a single cold Rydberg atom can even prevent the excitation of many other nearby atoms, which is known as the dipole blockade effect [13]. This is a result of an energy shift due to the dipole-dipole interaction between excited states pushing the multiply-excited state out of resonance [4].

One of the early motivations for developing the dipole blockade was for uses in quantum computing. The strong interaction between Rydberg atoms allows for the swift exchange of information [4], but there are significant technical challenges in placing Rydberg atoms on a regular lattice. A dipole blockade can help ensure that only one Rydberg atom is excited per lattice site. In essence, the dipole blockade offers coherent manipulation over a large collection of atoms, enabling tight macroscopic control over microscopic systems. This ability to precisely interact with quantum systems is critical in the development of quantum computing.

The dipole blockade effect was first observed in 2004 with the excitation of a dense ultracold gas of Rb atoms. By utilizing a second order dipole interaction between Rydberg atoms, a suppression in the total number excited was observed [14–16]. It has also been seen in other experimental setups which use first order dipole interactions [17–19]. The dipole blockade effect has even been explored in highly dense Bose-Einstein condensates [20].

As more and more experiments were able to create a dipole blockade effect, it became important for the underlying physics of the dipole blockade to be well understood. Because the dipole blockade can involve the interaction between many atoms, many-body effects will play a large role. An early simulation of the dipole blockade incorporated a simple mean field model which accounted for the many-body effects in the system by adding an energy shift caused by the other excited atoms to single-atom states [14]. While successful in describing the experimental measurements, the simple mean field model worked well only for high laser intensities and could not give information about the spatial relationships between excited atoms [21]. Later simulations used Monte Carlo approaches [17, 22–24] or a perturbative technique [25]. A drawback of the Monte Carlo models is that they do not contain information that can be obtained by using a wavefunction such as phase shifts or the amplitudes of specific states within the full wavefunction.

In chapter 2 of this dissertation, we studied these many body effects by simulating the many-body wavefunction using a direct numerical solution of Schrödinger's equation. As a result of using the many-body wavefunction we were able to calculate many useful properties of the system such as the fraction excited, the 2D two-particle correlation function between Rydberg atoms, number correlations, how the excitations fill space, and the phase errors accumulated during certain quantum information operations. We also compared our many-body wavefunction model to two other different models against a recent experiment where very large numbers of atoms are blockaded. This study lead to the realization that density variations in the ultracold gas can have a large effect on the excitation dynamics of the system.

1.2 Coherent hopping of excitation

The energy shift created by the dipole-dipole interaction between atoms in a frozen Rydberg gas can make it possible for resonant energy transfer to occur [8]. For example, when an atom in state A interacts via the dipole-dipole potential with an atom in state B the atom in state A is converted to B' while simultaneously the atom in state B is converted to A'. In this case, the energy cost for this transition must be minimal: $E_A + E_B \simeq E_{B'} + E_{A'}$. As a result of this transition it appears as though the characters of the two atoms have switched places or hopped [9]. This coherent hopping of excitation states makes the gas behave more like an amorphous solid than a gas, with excitations moving through the system like phonons, particles, or holes [26].

A major impetus for investigations of resonant energy transfer in a frozen Rydberg gas is the use of neutral atoms in quantum computing. In order to fully understand and control a quantum computer composed of atoms in an ultracold Rydberg gas, the spatial properties and dynamics of the excitations must be carefully explained [27].

Resonant processes in a Rydberg gas were first experimentally observed in 1998 by Mourachko *et al.* [9] and Anderson *et al.* [8] where the energy-transfer resonances in the excitation spectra were substantially broadened. The broadening of the line widths indicated that many-body effects were just as important to the dynamics of the system as two-body effects. Subsequent experiments have also verified the importance of simultaneous multiple atom interactions [28–31]. These complicated many-body interactions have also been studied in experiments investigating the effect of the orientation between dipole moments on the hopping probability [32], and the effects of a magnetic field on line broadening [33].

Since many-body phenomena in these systems are prevalent, the theoretical tools used to study them must also be able to take into account this complicated nature. Quantitative models have been performed to reproduce the major features observed in experiments [8,9,33], but more precise calculations are required to completely explain the measured linewidths. In fact, early models suggested that coherent hopping could not occur unless the temperature of the gas was extraordinarily low [34], but recent models have shown that hopping can occur at temperatures experimentally available [26].

In chapter 3, we studied the coherent hopping of character between Rydberg atoms by employing an essential states model and numerically solving Schrödinger's equation. The essential states model only includes states in the simulation that are degenerate or nearly degenerate. We investigated two separate cases: (1) where a single s atom is placed in a regular array filled with p atoms, and the s state hops from $|spp\cdots p\rangle$ to $|psp\cdots p\rangle$, $|pps\cdots p\rangle$, etc., and (2) where atoms are excited in a static electric field and the hopping occurs among the highest Stark states. Our calculations were able to produce band structures, and the effect of slight irregularities of the lattice on coherent hopping.

1.3 The effects of rotary and spin echo sequences on a Rydberg gas

In chapter 2, it will be shown that when the van der Waals interaction between Rydberg atoms is large enough it can push the excited states out of resonance with the laser. A Rydberg atom will block other excited states from occurring within a radius r_b. Within r_b the excitation cannot be pinned to a single atom, but rather it is de-localized over all N_b atoms inside the blockaded region. These so called "superatoms" [35] then collectively oscillate at a rate dependent on the $\sqrt{N_b}$. In section 2.7.1 of this dissertation we investigated the impacts of density variation on the collective oscillation rate and found that inhomogeneities in the density of the frozen Rydberg gas lead to inhomogeneities in the collective oscillation rates. The coherent nature of the system is therefore hidden to simple measurements that integrate over the entire signal [36]. Luckily echo techniques from nuclear magnetic resonance physics have been developed to overcome analogous inhomogeneities in oscillations due to irregular magnetic fields [37, 38]. A strong rotary spin echo signal is seen when the sign of the excitation amplitude is reversed exactly half-way through the total excitation time if no dephasing occurs aside from the excitation source [38].

In section 3.4, a coherent hopping of excitation is proposed between slightly irregular lattice sites. An experiment with clearly separated excitation regions should be able to detect the spatial nature of the coherent hopping. This type of spatially resolved measurement would be impossible in regular gas, and the coherent nature of the hopping would be hidden as the rate of hopping between atoms would be as inhomogeneous due to the irregularity in spacing between atoms (the hopping time between atoms is related to the inverse of the interaction energy between them: $t_{hop} \propto R^3/n^4$) [26]. This inhomogeneity due to spatial arrangement can also be overcome by an echo technique; this time a regular spin echo signal can be observed when the sample is excited via a special pulse sequence and outside sources of coherence such as temperature are small [37].

There has been a recent experiment which excited ground state atoms to Rydberg states in a very strongly interacting regime and proved the coherence of the system by using the rotary echo technique [36]. They were able to flip the excitation amplitude by using an RF field to shift the phase of the pulse by π. There has also been an experiment which used a regular spin echo technique to control the dephasing of a single ^{87}Rb atom [39].

In chapter 4, we investigated the effects of using echo sequences on collections of Rydberg atoms by using the many-body wavefunction approach to numerically solve Schrödinger's equation. Since our approach in chapter 2 took into account the spatial correlations between Rydberg states and employed a pseudoparticle approach similar to the superatom picture, our model was able to correctly reproduce the echo signal seen experimentally that a simple mean field approach could not. Our simulations demonstrated a perfect rotary echo when within the perfect blockade limit, and illustrated the effects of increasing density on the strength of the rotary echo signal. We also look at an ideal case where the sign of the entire Hamiltonian is reversed, thus in effect perfectly reversing the time evolution of the system. We next examined the effect of a spin echo sequence on the coherent hopping of excitation in a gas of Rydberg atoms. When the temperature is 0 μK, a system with only one hopper will perfectly echo, regardless of the inhomogeneity of the gas. We also examined the effect of nonzero temperatures on the coherence of the system.

1.4 Interactions between classical dipole moments: nanospheres

When excited by light, the electrons in a metallic nanosphere oscillate strongly and coherently. This resonant behavior is a consequence of the finite size of the nanoparticle and the restoring force of the nuclei [40]. The collective oscillation of the electrons is known as the dipole plasmon resonance of the nanoparticle. In fact, the optical excitation of plasmons is the most efficient process by which light interacts with matter [41]. These driven nanoparticles behave like oscillating classical dipole moments, creating their own time-dependent electric fields. In turn, these generated electric fields interact with nearby nanoparticles and thus couple collections of nanoparticles together producing coherent waves of oscillating dipole moments.

The study of metallic nanoparticles has been active for well over a century, dating as far back as the research done by Michael Faraday [42]. There have since been several models made to describe the optical properties of a single metallic nanosphere, from the exact solution to Maxwell's equations by Mie to the Drude model of dielectrics [40]. More recent studies have focused on the optical response of collections of nanoparticle and their uses in nanolithography [43], as efficient light-guiding nanolenses [44], spasers (surface plasmon amplification by stimulated emission of radiation) that generate intense local nanoscale optical-frequency fields [45], and other various possible uses as subwavelength optical devices.

Modern fabrication techniques using electron-beam lithography have allowed for the precise control over the location and particle size of nanoparticles [46]. Because a linear array is one of the easiest configurations to set up experimentally and theoretically, it has been extensively studied. Theoretical analyses of the optical response of a linear array of nanoparticles have been performed in variety of ways including the discrete dipole approximation [47], the multiple multipole model [48], the finite difference time domain method [46], and the T-matrix method [49].

In chapter 5, we described the dipole-dipole interactions between a linear array of optically driven silver nanospheres by using a coupled dipole approximation model that used the full electric field of an oscillating dipole. Using this model, each nanosphere is represented by a single point dipole that responds linearly to a driving electric field. By using classical electrodynamics and the Drude model to model the response of the nanospheres to light, we created self-consistent equations of motion for the oscillating electric dipoles. By solving these coupled equations we could determine the size of the dipole moment (and the ohmic power absorbed and radiated) of each nanosphere. Our simulations emphasized the importance of using the full field in the calculations and the resulting asymmetric response observed as a result of the retarded scattered light.

CHAPTER 2

DIPOLE BLOCKADE

2.1 Introduction

Atoms excited into Rydberg states are large in size and thus able to support large dipole moments. The long range interactions between these large dipoles have been a popular topic of study over the last several years. [3, 8, 9, 14, 15, 19, 20, 23, 24] When an ultracold gas of Rydberg atoms is suffiently cold and dense enough, the effect of the motion of the atoms is small compared to the possibly large interactions between them. These relatively strong and long range interactions between dipole moments should dominate the physics in this ultracold regime, making it possible to study interesting many-body effects in detail. One such effect is seen when the interaction energy between Rydberg atoms is large enough to shift multiply-excited states out of resonance with a tightly tuned excitation laser. With multiple excitation states now blocked from occurring, the number of atoms able to be excited is suppressed. This suppression in the number of excited atoms is known as the dipole blockade effect [13].

The dipole blockade effect, was first described in Ref. [4] as a method for the macroscopic control and operation of quantum logic gates. Jaksch *et al.* proposed for the blockade to be generated by utilizing the first order interactions between dipole moments created by exciting a gas of ultracold alkali atoms in a static electric-field. With recent advancements in cooling and trapping, the first order static dipole-dipole (SDD) interaction described in that proposal has been experimentally verified to produce a dipole blockade in a gas of ultracold cesium atoms [17] . In Ref. [13] the proposed interaction was between Rydberg atoms at Förster resonance and a successful dipole blockade was observed for this configuration as well [18]. A blockade using the second order van der Waals (vdW) interaction has also been seen in various experiments [14–16, 19, 50]. In this chapter we investigate both the first order SDD and second order vdW interactions between large numbers of atoms. In both cases, the initial state is coherent; in other words we do not allow the ground level to decay or be repopulated. If a narrow enough bandwith laser is used to drive atoms from the ground state to a high Rydberg state ($n > 40$) on resonance, the dominant process will be the dipole allowed transition [51] and each atom can be treated as a strictly two-level system.

The possibly large and long range interaction between pairs of Rydberg atoms implies that any theoretical study of a large collection of N atoms must be able to take into account the many-body nature of the system. The effect of many-bodies has been modeled using a mean field [14], a Monté Carlo approach [17, 22, 23], and a perturbative approach [25]. By a direct numerical solution of Schrödinger's equation we were able to compute and retain various interesting properties of the many-body wavefunction. Although the Monte Carlo procedures require less computational effort, they cannot be used to probe quantities such as phase shifts or the amplitudes of certain pieces of the full wavefunction useful for quantum computing. The use of a mean field in [14] works well for high laser powers, but is unable to give information about the spatial correlations that can develop within the excited gas. Unless otherwise noted, atomic units will be used throughout this paper.

2.2 The many-body wavefunction

In this section we will describe the techniques involved in the direct numerical solution to the many-atom wavefunction. We will also discuss how we solved for the wavefunction in a manner that allowed us to check for convergence. Once the wavefunction has been propagated, it is possible to compute the number of excited atoms and various correlation functions.

We begin by treating each atom as a purely two-level system with one level being the initial tightly bound, non-decaying ground state $|g\rangle$, and the other being a highly excited Rydberg state $|e\rangle$. For the purposes of this chapter the locations of the atoms will be fixed in space. This is a reasonable approximation if the temperature of the gas is low enough and the time duration of the exciting laser pulse is short enough. The motion of the atoms must be small compared to distances where the interaction strength between dipoles is dominant. For example, using conditions similar to the experiment in Ref. [51], where the temperature of the gas is around 100 μK and the peak density is 10^{11} cm^{-3}, the simulation time must be $\lessapprox$ 200 ns in order to effectively ignore the motion of the atoms. We expanded the wavefunction onto product states of two-level systems ($|a\rangle_1 \otimes |b\rangle_2 = |ab\rangle$, etc):

$$\begin{aligned}
|\Psi(t)\rangle &= a_{gg...g}(t)|gg...g\rangle + a_{eg...g}(t)|eg...g\rangle + \\
\cdots & +a_{ee...g}(t)|ee...g\rangle + a_{ee...e}(t)|ee...e\rangle \qquad (2.1) \\
&= \sum_{\alpha} a_{\alpha}(t)|\alpha\rangle.
\end{aligned}$$

Quite clearly the number of basis states needed to completely describe the wavefunction increases as 2^N and becomes prohibitively large when $N > 15$. As it would be impractical to do otherwise, we did not use all of the basis states in the expansion but recursively eliminated them using the pseudoparticle approach described by Ref. [21]. These pseudoparticles have an interaction strength with the laser $\sqrt{W}$ times bigger than the single atom case, where the weight W is the number of atoms in each pseudoparticle. In this method, real atoms (pseudoparticles with weight equal to one) were randomly placed within a volume large enough to cover the region of correlation; then these strongly blockaded atoms were recursively grouped together to form pseudoparticles until the number of real atoms, N, was reduced down to the desired number of pseudoparticles, N_p. The recursion was as follows: (1) the nearest neighbors j and k were found, (2) these two "atoms" were joined and replaced by a pseudoparticle i located at the center of mass position $\vec{r}_i = (W_j\vec{r}_j + W_k\vec{r}_k)/(W_j + W_k)$, and (3) the weight of the created pseudoparticle is increased to $W_i = W_j + W_k$ while removing j and k from the simulation. The errors created by forcing correlations between atoms can be controlled by increasing the number of pseudoparticles.

Now the interaction between excited pseudoparticles j and k, can be calculated by averaging over the interactions V between all of the pairs of associated atoms:

$$V_{jk} = \frac{1}{W_j W_k} \sum_{n \in j} \sum_{m \in k} V_{nm}(R_{nm}), \tag{2.2}$$

where R_{nm} is the distance between atoms n and m, which belong to pseudoparticles j and k respectively. Another way to calculate the interaction would be to simply use the positions of the pseudoparticles themselves. Now $V_{jk} = V(R_{jk})$. Clearly as the number of pseudoparticles is increased the two different methods will give the same interaction energies. We used the latter approach in our calculations because it converged faster with respect to random geometries as long as enough pseudoparticles were used.

2.3 The Hamiltonian

The Hamiltonian of this system is:

$$\begin{aligned} \hat{H}(t) &= \sum_j \hat{H}_j^{(1)}(t) + \sum_{j<k} V_{jk} |e_j e_k\rangle\langle e_j e_k| \\ \hat{H}_j^{(1)}(t) &= -\left(\Delta\omega(t) + \varepsilon(t)\right) |e_j\rangle\langle e_j| + \mathcal{F}(t) \frac{\Omega_0}{2} \sqrt{W_j} \left(|g_j\rangle\langle e_j| + |e_j\rangle\langle g_j|\right) \end{aligned} \tag{2.3}$$

where V_{jk} is the interaction between two excited states for a pseudoparticle pair (j, k). The detuning of the laser is $\Delta\omega(t)$, and $\varepsilon(t)$ is a mean field energy shift due to excited atoms outside of the simulated volume. Since our simulation box size cannot be accurately approximated as infinite, we need to try to reduce erroneous edge effects when attempting to model the entire gas. We accomplished this by employing wrap boundary conditions, which also help to hasten convergence. The single atom Rabi frequency between states $|g\rangle$ and $|e\rangle$ is Ω_0, and the number of atoms in each pseudoparticle j, is W_j. $\mathcal{F}(t)$ describes the time dependence of the shape of the laser amplitude. Equation 2.3 was also obtained by using the rotating wave approximation. If we use parameters similar to [14], the laser frequency is in the UV range and at a relatively low intensity, allowing for the rotating wave approximation to be a good one. If, however, the parameters in [52] are used and a microwave transfer pulse is introduced then careful consideration must be used when applying this approximation. If the detuning is set to zero, the mean field is negligible, and the system is perfectly blockaded (*i.e.* at most one excitation is possible), then a system of N atoms evolves in an oscillatory manner between all the atoms in the ground state and a symmetrical state with only one excited Rydberg atom. The frequency of this oscillation is $\sqrt{N}\Omega_0$. The dynamics of this two level system can be given as:

$$\begin{bmatrix} a_g(t) \\ a_e(t) \end{bmatrix} = \begin{bmatrix} \cos(\theta(t)/2) & -i\sin(\theta(t)/2) \\ -i\sin(\theta(t)/2) & \cos(\theta(t)/2) \end{bmatrix} \begin{bmatrix} a_g(0) \\ a_e(0) \end{bmatrix}, \tag{2.4}$$

where $\theta(t) = 2\sqrt{N}\Omega_0 \int_{t_0}^{t} \mathcal{F}(t')\, dt'$. The probability of being in the excited state at the end of the laser pulse is $\sin^2(\theta(t)/2)$.

In order to solve Schrödinger's Equation numerically, we use the split operator method:

$$|\Psi(t+\delta t)\rangle = e^{-i\hat{H}_{diag}(t)\delta t/2} e^{-i\hat{H}_{off}\delta t} e^{-i\hat{H}_{diag}(t)\delta t/2} |\Psi(t)\rangle, \tag{2.5}$$

where $\hat{H}_{diag}$ is the matrix of diagonal elements (Rydberg-Rydberg interaction) of $\hat{H}$ and $\hat{H}_{off}$ is the matrix of off-diagonal elements (laser interaction) of $\hat{H}$, such that $\hat{H} = \hat{H}_{diag} + \hat{H}_{off}$. At this point, the laser part of the interaction is approximated via the second order Runge-Kutta method. The single time step error introduced by using the split operator is of $O(\delta t^3)$, and by using second order Runge-Kutta the norm $\langle \Psi(t)|\Psi(t)\rangle$ is no longer conserved. By using small enough time steps we are able to minimize this error.

2.3.1 First order interaction

For a group of cold Rydberg atoms in a static electric-field $\mathcal{E}$, the SDD interaction between atoms j and k can be written as:

$$V_{jk} = \frac{\vec{d_j} \cdot \vec{d_k} - 3(\vec{d_j} \cdot \hat{R}_{jk})(\vec{d_k} \cdot \hat{R}_{jk})}{R_{jk}^3}, \tag{2.6}$$

where $\vec{d_j}$ is the dipole matrix element for atom j. If the electric field is in the $\hat{z}$ direction and the atoms are excited to the highest energy Stark state, then the dipole matrix elements are: $\vec{d} = (3/2)n^2\hat{z}$. Finally, Eq. 2.6 can be rewritten as:

$$V_{jk} = \frac{9n^4}{4}\frac{1-3\cos^2(\theta_{jk})}{R_{jk}^3}, \tag{2.7}$$

where θ_{jk} is the angle formed between the vector pointing from atom j to k and the direction of the electric field. Clearly the SDD interaction is proportional to $1/R^3$ and scales like n^4. When using the SDD interaction It is also important to take into account the relative orientation between atoms, at least in the spherical polar direction.

2.3.2 Second order interaction (van Der Waals)

With no electric field, a second order interaction between two atoms in states ν_0 and μ_0 respectively, takes place:

$$V_{jk} = \frac{1}{R_{jk}^6}\sum_{\nu,\mu}\frac{|\langle\nu|\langle\mu|\vec{r}_j\cdot\vec{r}_k - 3(\vec{r}_j\cdot\hat{R}_{jk})(\vec{r}_k\cdot\hat{R}_{jk})|\nu_0\rangle|\mu_0\rangle|^2}{E_\nu + E_\mu - (E_{\nu_0}+E_{\mu_0})}. \tag{2.8}$$

This can be more concisely written as $V_{jk} = -C_6/R_{jk}^6$ and the C_6 coefficient is proportional to n^{11}. There are several standard methods of the calculating the C_6 [53, 54]. We calculated the C_6 coefficient while taking into account the spin-orbit interaction by using second order perturbation theory and quantum defect theory. The necessary wavefunctions were generated by direct numerical integration in the radial direction using a square root mesh and the quantum defects given by Ref. [55], and the angular depedence was found using angular momentum relationships outlined in Ref. [56]. The resulting C_6 was in good agreement with results that did not take into account the spin-orbit interaction [53].

In this chapter we only looked at $ns - ns$ interactions in order to eliminate any directional dependence.

2.4 Correlation

After propagating the wave equation for a period of time, the fraction of excited atoms can be easily determined by projecting the wavefunction onto the states $|\alpha\rangle$:

$$P_e = \sum_{\alpha} \frac{N_\alpha}{N} |\langle\alpha|\Psi\rangle|^2 = \sum_{\alpha} \frac{N_\alpha}{N} |a_\alpha(\infty)|^2, \tag{2.9}$$

where N_α is the number of atoms excited in state $|\alpha\rangle$. It is also possible to calculate a spatial correlation function, which is the probability of finding two excited atoms separated by a distance R divided by the probabilities of each individual atom:

$$C(R) = \frac{P_{ee}(R)}{P(R)P_e^2}. \tag{2.10}$$

$P_{ee}(R)$ is the probability to find two atoms excited a distance R apart:

$$P_{ee}(R) = \sum_{j<k} |\langle\beta_{jk}|\Psi\rangle|^2, \tag{2.11}$$

such that state $|\beta_{jk}\rangle$ has excited atoms j and k a distance R apart. $P(R)$ is the probability of finding a pair of atoms separated by a distance R. By examining this two particle correlation function, we can estimate R_b, the blockade radius [21].

2.4.1 Pair correlation

If we take advantage of the azimuthal symmetry of the Hamiltonian and take a slice in the xz plane, we can look at the 2D pair correlation function. For this simulation we used ten ^{85}Rb atoms and randomly placed them using a uniform spatial distribution in a sphere of radius R_0 with no wrap boundary condition and no mean field. For the vdW case $R_0 = 12.5\ \mu$m and for the SDD case $R_0 = 25\ \mu$m. In both cases we excite via a π pulse for 120 ns that is perfectly on resonance ($\Delta\omega = 0$). A π pulse perfectly tansfers a two level system from the ground state to the excited state. According to Eq. 2.4 when $\theta(t) = \pi$, the system is completely in the excited state. This means that a π pulse can be defined by $2\sqrt{N}\Omega_0 \int_{t_0}^{t} \mathcal{F}(t')\, dt' = \pi$, or

$$\int_{t_0}^{t} \mathcal{F}(t')\, dt' = \frac{\pi}{2\sqrt{N}\Omega_0}. \tag{2.12}$$

The shape of the laser pulse $\mathcal{F}(t)$ is given by:

$$\mathcal{F}(t) = \frac{\mathcal{S}}{\Omega_0 \tau}\, e^{-(t/\tau)^2}, \tag{2.13}$$

where $\mathcal{S}$ is related to the laser amplitude and τ is the pulse duration. Using the above shape of the laser pulse, a π pulse occurs when the laser amplitude

$$\mathcal{S}_\pi = \frac{1}{2}\sqrt{\frac{\pi}{N}}. \tag{2.14}$$

The top plot in Fig. 2.1 is the pair correlation $C(\Delta x, \Delta z)$ for the vdW interaction. As expected, the vdW case is also symmetric in the polar direction. A reasonably accurate blockade region can be defined by R_b. If an atom is excited then all of the other atoms within a distance R_b are blockaded. In the dipole-dipole case (static electric field in the $\hat{z}$ direction) the interaction potential depends on θ_{jk}, the angle between the electric field and the vector connecting atoms j and k. In fact when $\cos(\theta_{jk}) = \pm\sqrt{1/3}$, $V_{jk} = 0$; the interaction vanishes and the two atoms are independent of each other. This can be seen in the bottom plot of Fig. 2.1; along the angle $\cos(\theta_{jk}) = \sqrt{1/3}$ ($\theta_{jk} \approx 55°$), the blockade region is pierced. In order to have a well defined R_b as in the vdW case, the geometry must be set up where $\cos(\theta_{jk}) \neq \pm\sqrt{1/3}$ for as many j, k pairs as possible. This can be accomplished by placing atoms in a thin plate on the xy plane; by decreasing the thickness we can adjust the number of pairs that lie along the critical angle. If the atoms lie in the xy plane, then C is only a function of R, $C \simeq C(R)$.

The value of R_b can be estimated by finding the distance where $V_{jk} \approx \hbar/\tau$. Since the correlation function is not a perfect step function [21], the value of R_b is not exact unless a well-defined criteria is established. In this paper, the blockade radius for a

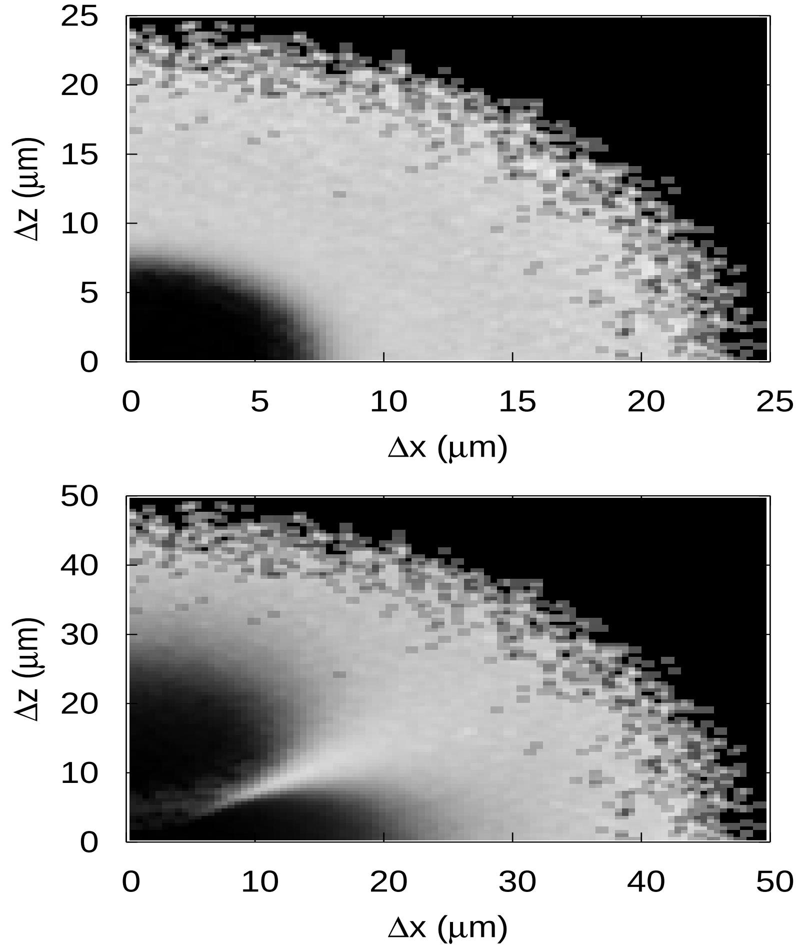

Figure 2.1: The two particle correlation function for a group of Rydberg atoms. The top graph is for the second order (van Der Waals) interaction and the bottom graph is for the first order interaction. The axes are the distances between particles in the x and z direction. The grey-scale indicates the probability of finding a second Rydberg atom at a location with respect to a Rydberg atom at the origin. Black is the smallest probability. The correlation function drops to zero outside of 25 μm in the vdW case and outside of 50 μm for the first order case. This is due to the fact that there are no pairs that exist with distances greater than $2R_0$, where R_0 is the size of the uniformly distributed sphere.

given $\mathcal{S}/\tau$ is defined in the following manner: it was the diameter of the largest sphere where the average maximum number of excited atoms within that sphere was 1.01. As a test of our definition of R_b, we computed the probability of being in the blockade state $(|egg...g\rangle + |geg...g\rangle + \cdots + |ggg...e\rangle)/\sqrt{N}$, and the phase of the amplitude of the blockade state. When $\langle N_e \rangle = 1.01$, then the probability of being in the blockade state is approximately 98%, and the phase shift is about 0.52π; for a perfect blockade these should be 100% and $\pi/2$.

2.4.2 Number correlation

When a collection of cold atoms is in a blockade configuration (i.e. the physical parameters are such that the interaction energy between two Rydberg atoms is large enough to shift the pair out of the two excitation resonance), the number of atoms that can be excited (N_e) is suppressed. By taking repeated measurements of N_e, we can find the relationship between the mean $\langle N_e \rangle$ and the variance $\langle N_e^2 \rangle - \langle N_e \rangle^2$. The Mandel Q-parameter, $Q \equiv \frac{\langle N_e^2 \rangle - \langle N_e \rangle^2}{\langle N_e \rangle} - 1$, is a useful quantity to compare the atom counting statistics to a Poissonian distribution [57]. For a Poissonian distribution the mean is equal to the variance, so $Q = 0$. In the case of blockaded atoms Q should be less than zero; this corresponds to a sub-Poissonian distribution. The Q parameter reflects the measure of how efficiently the system is blockaded. Recent experiments have been able to measure Q values [19], and in this section we will present the results of our simulations of Q. By time propogating the many-body wave function, Q is readily found. For a collection of N completely independent quantum atoms with a probability P_e of being excited:

$$\langle N_e \rangle = \sum_{j=0}^{N} \begin{pmatrix} N \\ j \end{pmatrix} j P_e^j (1 - P_e)^{N-j} = N P_e \tag{2.15}$$

and

$$\begin{aligned} \langle N_e^2 \rangle &= \sum_{j=0}^{N} \begin{pmatrix} N \\ j \end{pmatrix} j^2 P_e^j (1 - P_e)^{N-j} && (2.16) \\ &= (N P_e)^2 + N P_e (1 - P_e). && (2.17) \end{aligned}$$

So for the extreme uncorrelated case, $Q = -P_e$ (i.e. uncorrelated quantum systems do not give $Q = 0$, but minus the fraction excited). The other extreme case is if N_b atoms are located within a blockade region. Now only up to one atom can be excited, thus:

$$\begin{aligned} \langle N_e \rangle &= N_b P_e && (2.18) \\ \langle N_e^2 \rangle &= N_b P_e. && (2.19) \end{aligned}$$

So $Q = -N_b P_e$ for the case of N_b atoms being within the blockade radius. In Fig. 2.2, the Q value is plotted as a function of the fraction of atoms excited for different densities: $\rho_0 \approx 1.3 \times 10^{10}$ cm^{-3}, $\rho_0/8$, $\rho_0/27$, $\rho_0/64$, and $\rho_0/512$. In all cases, 10 atoms were used in the simulation. Figure 2.2.a was generated using the vdW ($1/R^6$) interaction, while Fig. 2.2.b used the dipole-dipole ($1/R^3$). At the lowest density,

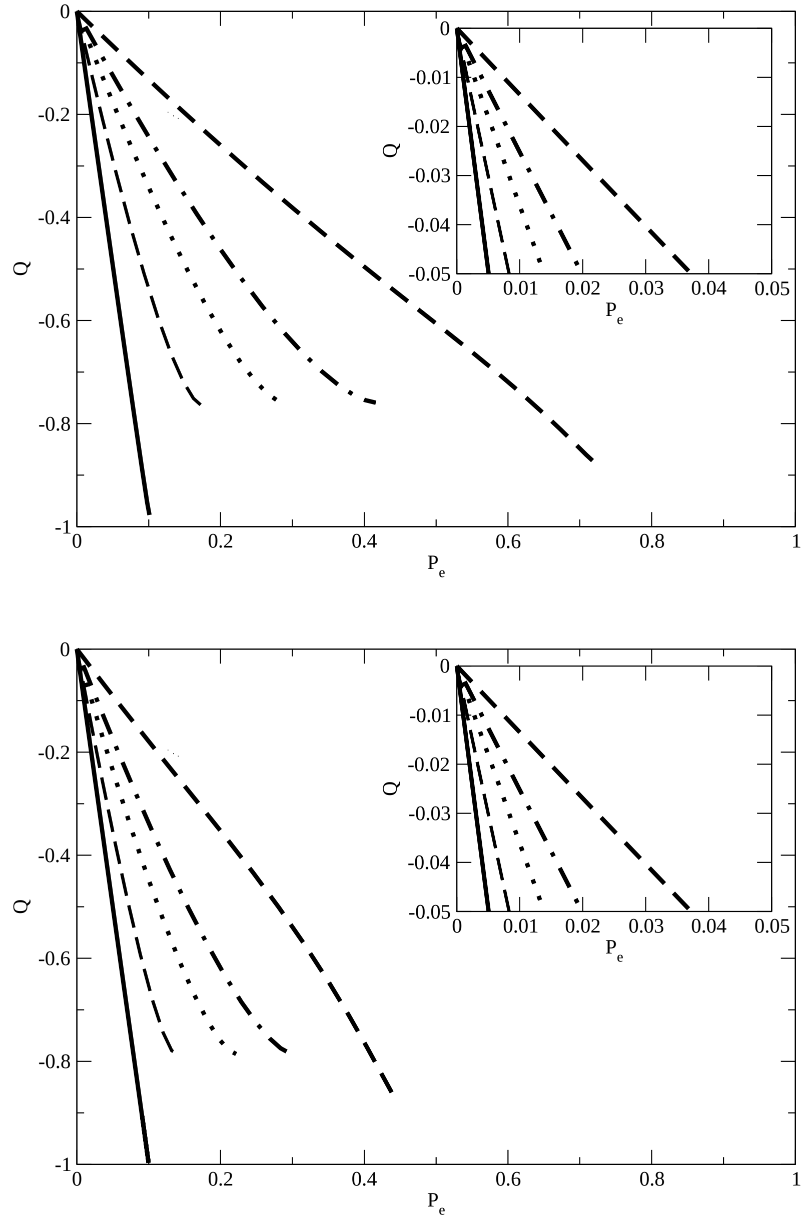

(b)

Figure 2.2: Q values as a function of the fraction excited (P_e) for different densities. The solid line was calculated using a density $\rho_0 \approx 1.3 \times 10^{10}$ cm^{-3}. Moving from left to right, the densities decrease as follows: $\rho_0/8$ (dashed), $\rho_0/27$ (dotted), $\rho_0/64$ (dash-dotted), and $\rho_0/512$ (thick-dashed). The inset is a blowup of the region where there are very few excitations. Figure 3.2.a is for the vdW case and Figure 3.2.b is for the dipole dipole interaction. The line $Q = -P_e$ results when the atoms are uncorrelated.

$Q(P_e) \simeq -1P_e$, indicating a very low level of correlation. In essence, we have a group of isolated two level systems. As the density is increased, the slope of $Q(P_e)$ steepens suggesting the system is becoming more and more highly correlated. Because the dipole-dipole interaction has a longer range than the vdW case, the slope of $Q(P_e)$ is steeper for the former. The inset examines the system at low laser intensities, or equivalently when few atoms are excited. It can been seen that the slope remains relatively constant in both the vdW and dipole-dipole cases, showing the system is still correlated even when few particles are excited. Although the excited atoms are not in a blockade configuration with each other, the blockaded atoms near by certainly are. These blockaded atoms are still conveying the information about the system to the separated excited atoms. They are in the ground state because they are blocked from being excited, not just because the fraction of excitiation is small. It is the initial state of the system which holds information, even before the interactions are turned on. By comparing the slope m of $Q(P_e)$ to the perfectly blockaded case, we can in effect measure how efficient the interaction is at turning the system from a large collection of uncorrelated two level systems to a single two level system. In fact, $-N/m$ gives a rough indication of how many uncorrelated two level systems remain in the collection.

2.5 Filling factor for excitations

If a group of atoms is all within R_b then at most only one excitation is allowed. If every excited atom creates a bubble of radius R_b around itself, then in a given volume the maximum number of excited atoms should be approximately the number of bubbles that can fit into that volume. We examined how the maximum number of allowed excitations increases as the volume containing the atoms is increased while maintaining a fixed density. We focused on the case of the atoms placed in a line because that situation should show the largest effect. We initially placed 5 atoms on a linear lattice 1.7 μm apart and excited the system to the maximum number excited via a pulse 120 ns long. For these parameters $R_b \sim 8.2\ \mu m$. We then increased the number of atoms in the line and again excited to the maximum N_e. If the bubble picture is correct, then the maximum number of excited atoms should remain about 1 until two bubbles of radius R_b can fit into the line; then the number of excitations should jump to 2. We also looked at the non-lattice case where we randomly placed the appropriate number of atoms in the lengths used in the perfect lattice case. In Fig. 2.3a we plotted the maximum $\langle N_e \rangle$ as a function of chain length L for both the perfect lattice case and the random case. In either case, the average number of excited atoms rises fairly linearly with chain length, and as soon as there is room for more than one excitation, $\langle N_e \rangle$ does not jump up to the next integer number excited. The $\langle N_e \rangle$ fills the region rather smoothly, so the bubble picture is not entirely correct. Figs. 2.3.b and 2.3.c illustrate how states with excited atoms become available as L is increased. The solid line is the probability of being in a state with only one atom excited, the dashed line is for being in a state with only two excited, and the dotted line is for three. The smoothness of Fig. 2.3.a can be explained for by looking at the probabilities of being in various excited states. By the time the probability of

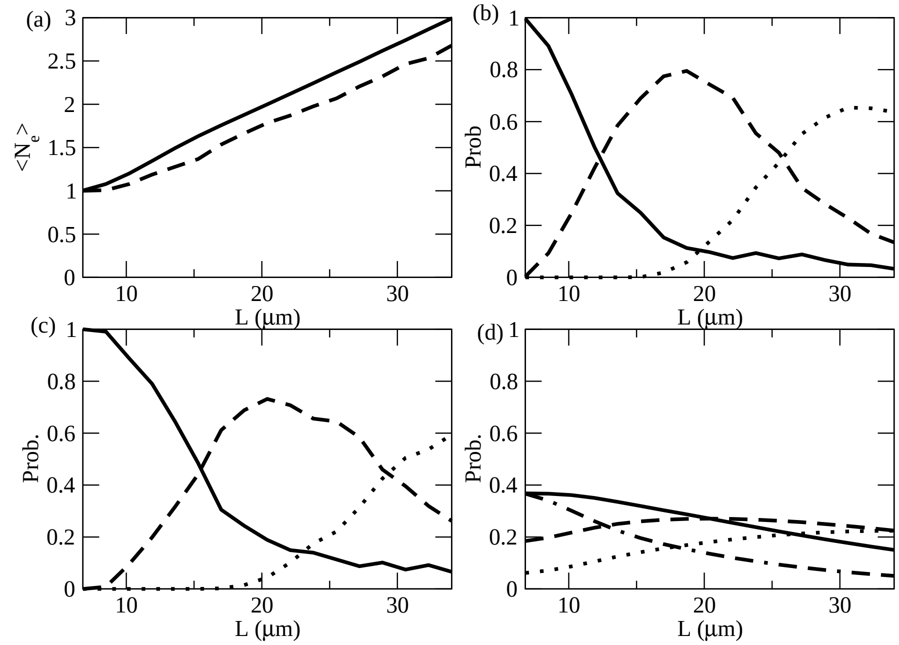

Figure 2.3: Figure 2.3.a is the maximum $\langle N_e \rangle$ for atoms in a line of length L. The solid line is for the perfect lattice case while the dashed line is when the atoms are randomly distributed on the line. In Figure 2.3.b the solid line is the probability of being in a state with exactly one atom excited as a function of the length L for the perfect lattice case. The dashed line is the probability of being in a state with only two atoms excited and the dotted line is the probability of being in a state with three atoms excited; all for the perfect lattice case. Figure 2.3.c is the same plot as 2.3.b except for the randomly distributed geometry. Figure 2.3.d is also the same plot as 2.3.c and 2.3.b except using a Poissonian distribution. The dash-dot line is the probability of zero atoms being excited, the solid is for one excited, the dashed is for two excited, and the dotted is for three excited.

being in a state with only one excited atom is down to around 50%, the probability of being in a state with two excited has risen to about 50%. Figure 2.3.d is similar to Figs. 2.3.b and 2.3.c except that what is plotted here is the probabilities of being in certain states given a Poissonian distribution. As expected, it is quite different from the sub-Poissonian distribution of our correlated system.

2.6 Phase gates

If the system is sufficiently sparse, the Rydberg atoms all act as isolated two level systems or, in the parlance of quantum computing, each atom represents an independent qubit. When a group of atoms is perfectly blockaded, it also forms a single two level system. This group of atoms appears as a two level system, but it is actually a collection of atoms so tightly correlated that they act as a single two level system. If we had two isolated groups of atoms each of the same size and density such that each group was perfectly blockaded, then we would have two qubits. If we made both groups such that they both sat within R_b, then again we would have a single two level system. As we move one group outside of the blockade region, pairs of intergroup atoms will no longer strongly interact with each other allowing the possibility of a third level: both groups containing an excited atom. When the largest intergroup pair distance is greater than R_B, both groups are now independent of each other and we are back to two uncorrelated two level systems. If they are not too far apart, however, $R_{pair,max} \lesssim R_b$, most of the intergroup pairs are still correlated, thus both groups are as well. Being in such a state would be undesirable as it leaves us with neither a single two level system or two uncorrelated two level systems.

A quantum gate transforms an initial state to another state. We created two spheres of cold atoms, each of radius $R_0 = R_b/4$, separated by a center to center distance D. Within each sphere, we randomly placed 8 atoms. The two groups of atoms are then subjected to the following sequence of pulses: group one is excited by a π pulse, group 2 is excited by a 2π pulse ($\mathcal{S}_{2\pi} = 2\mathcal{S}_{\pi}$), and finally group 1 is de-excited by another π pulse. The excited atoms interact via the dipole-dipole or van der Waals interaction, depending on the situation. We varied the mean interaction energy between the two groups by increasing D. In the ideal case we can represent each group as a two level system, so the initial state is the ground state $|gg\rangle$. When the first group is excited by a π pulse $|gg\rangle \longrightarrow -i|eg\rangle$. If both groups are independent of each other then a 2π pulse will take $-i|eg\rangle \longrightarrow i|eg\rangle$, but if the groups are both within R_b then it is impossible to excite the second atom and this pulse leaves the state unaffected: $-i|eg\rangle \longrightarrow -i|eg\rangle$. The final π pulse to the first atom will de-excite it and mupliply the state by $-i$: for the uncorrelated case $i|eg\rangle \longrightarrow |gg\rangle$ and for the blockaded case $-i|eg\rangle \longrightarrow -|gg\rangle$. When the groups are independent, there is no accumulated phase shift; the sequence of pulses leaves the original state unchanged. When the system is blockaded, a phase shift ($\Delta\phi$) of π is acquired, making a phase gate [13].

The top plot in Fig. 2.4 shows the phase shift $\Delta\phi/\pi$ as a function of the average maximum intergroup pair distance, $\langle R_{max}\rangle$,divided by the blockade distance. As D

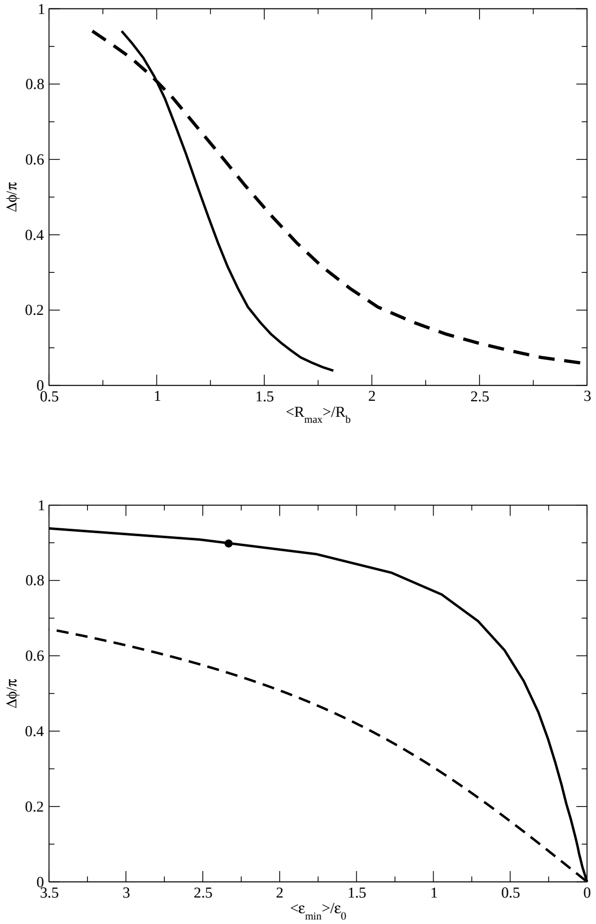

(b)

Figure 2.4: Two regions of equal size and density are excited by a $\pi - 2\pi - \pi$ sequence of pulses in the following manner: group 1 is excited by a π pulse then group 2 is excited by a 2π pulse and finally group 1 is de-excited by another π pulse. Figure 2.4.a shows the phase shift $\Delta\phi/\pi$ as a function of the average maximum intergroup pair distance, $\langle R_{max} \rangle$,divided by the blockade distance R_b. The solid line is for the vdW case ($1/R^6$), while the dashed line is for the dipole-dipole case ($1/R^3$). Figure 2.4.b is $\Delta\phi/\pi$ as a function of $\langle \varepsilon_{min} \rangle / \varepsilon_0$, where ε_0 is the pair energy of two excited atoms separated by R_b. The solid line is for the many atom case. The dot indicates a phase shift of 0.9π. The dashed line is for the perfect two particle case, where the two atoms are in the center of each sphere.

is increased, the distance between the two furthest pairs will also increase beyond R_b. This allows for the possibility of more than one atom to be excited, thus introducing an error into phase shift. The solid line in Fig. 2.4.a is for the vdW case and the dashed is for the dipole-dipole interaction. The rapid $1/R^6$ scaling of the vdW interaction can be seen in the steep drop of the phase shift with increasing $\langle R_{max} \rangle$. As expected, when $\langle R_{max} \rangle$ is small $\Delta\phi/\pi$ approaches 1, and when $\langle R_{max} \rangle$ is large $\Delta\phi/\pi$ tends to 0. With every intergroup distance an intergroup pair energy can be calculated, so with each average maximum intergroup pair distance there is an associated average minimum intergroup energy, $\langle \varepsilon_{min} \rangle$, where $\varepsilon = V\tau/\hbar$. The solid line in Fig. 2.4.b is $\Delta\phi/\pi$ as a function of $\langle \varepsilon_{min} \rangle / \varepsilon_0$, where ε_0 is the pair energy of two excited atoms separated by R_b. The dot indicates a phase shift of 0.9π. The dashed line is for the perfect two particle case where the two atoms are in the center of each sphere. If a phase error of less than 10% is desired, then the average minimum pair energy must be greater than about 2.5. If phase error of less than 5%, is required then $\langle \varepsilon_{min} \rangle > 3.5$. The difficulty in reducing the error is evident in the flatness of the curve in Fig. 2.4.b as $\Delta\phi/\pi$ goes to 1.

2.7 Dipole blockade at higher densities

This section focuses on calculations regarding Rydberg excitation of ultracold atoms at higher densities than previously discussed. We simulated the physical setup similar to Ref. [50]. In that experiment, a two-photon excitation scheme is employed from the $5S_{1/2}$ to $5P_{3/2}$ and finally to $43S_{1/2}$. Due to a large detuning to the blue on the $5S_{1/2}$ to $5P_{3/2}$ transition, the three levels can be reduced to an effective two level system [50]. So for all intents and purposes, we will consider each atom as a strictly two-level system: a tightly bound, non-decaying ground state, $|g\rangle$ ($5S_{1/2}$), and an excited Rydberg state, $|e\rangle$ ($43S_{1/2}$). The atoms are excited by a narrow bandwidth laser which is quickly and smoothly switched on for an excitation time $\tau < 20\mu$s. In previous sections the time scale for collective excitation was governed by the shape of the laser pulse, but in this case the time scales are set by the energies involved in the many-body interactions. To match the experiment, we will take the density distribution of ground state atoms to be Gaussian:

$$\rho(r, x, y, z) = \rho_0 e^{-(x^2+y^2)/\sigma^2 - z^2/\Delta z^2}, \tag{2.20}$$

where ρ_0 is the peak density, $\sigma = 12\mu$m is the width in radial direction, and $\Delta z = 220\mu$m is the width in the axial direction. Since the peak density of the gas is quite high ($\rho \sim 3 \times 10^{12}$ cm^{-3}) and the van der Waals interaction between excited Rydberg atoms can be very large ($C_6 \propto n^{11}$), including many-body effects is important.

We take into account three interactions: the interaction of the laser with the atoms, the van der Waals interaction between two excited Rydberg atoms, and a mean field energy shift between an excited Rydberg atom and excited Rydberg atoms outside of the simulated box. The experimental setup in [50] was able to cool the gas to 3.4 μK. At such a low temperature, the motion of the atoms is still small compared to common blockade radii ($v\tau \sim 0.6\,\mu$m, $R_b \sim 5\,\mu$m), so we fixed the atoms in space.

We again used the expansion of Eq. 2.1 to describe the many-body wavefunction and used a psuedoparticle approach very similar to one used in Ref. [21] to reduce the number of basis states. In Sec. 2.2 the atoms were randomly placed within a volume large enough to cover the region of correlation and then recursively grouped together to form pseudoparticles. The atoms were grouped according to distance, with the nearest neighbors being joined until the appropriate number of pseudoparticles was reached. The location of the pseudoparticle was the center of mass position of the associated atoms. When the number of atoms, N_a, is low, the N_a^2 nature of this recursion is not significant when it comes to computing time. However, when N_a reaches the thousands needed to simulate densities along the lines of Ref. [50], using that recursion relation becomes computationally taxing. Here we took an alternative approach by using a Sobol sequence to place the pseudoparticles first. The Sobol sequence is a quasi-random sequence that fills space in a more uniform manner than uncorrelated random points [58]. It avoids the clumpiness that occurs when filling a space with a random sequence, thus leading to quicker convergence. Once the pseudoparticles are placed, we generate a random position for an atom and, using wrapped boundary conditions, find which pseudoparticle it is nearest. The weight W of that pseudoparticle is then increased by one and the process is repeated until all of the atoms have been accounted for. There will now be a Poissonian distrubution of atoms per pseudoparticle.

The Hamiltonian of the system can be written using Equation 2.3 where $V_{jk} = -C_6/R_{jk}^6$ is the two particle interaction between pseudoparticles j and k. The $43S_{1/2}$

state has a repulsive van der Waals interaction ($C_6 = -1.67 \times 10^{19}$). The detuning of the laser $\Delta\omega(t) = 0$, and for the van der Waals potential $\varepsilon(t) \simeq -P_e(t)\, 20\, C_6\, \rho L^{-3}$, where $P_e(t)$ is the fraction of atoms excited at time t and L^3 is the volume size. The time dependence of the shape of the laser is described by:

$$\mathcal{F}(t) = \begin{cases} e^{-25(t-t_r)^4/t_r^4} & \text{for } t < t_r \\ 1 & \text{for } t_r \leq t \leq \tau \end{cases}, \tag{2.21}$$

where $t_r = 100$ ns $\ll \tau$ is the ramp-on time and τ is the excitation time.

2.7.1 Blockade radius

An atom can be considered blockaded when the two particle van der Waals interaction shifts the doubly excited state out of resonance, $C_6/R^6 > \Omega$. The interaction distance at which this occurs is called the blockade radius, $R_b \sim (C_6/\Omega)^{1/6}$. An ensemble of N_b blockaded atoms oscillates between a ground state and a symmetrical state with one excitation at the frequency $\Omega = \sqrt{N_b}\Omega_0$. At high densities the number of atoms blocked per excited atom, N_b, is large and closely follows a Poissonian distribution. When N_b is small, this increase in frequency is not significant; as $\sqrt{N_b}$ grows large, this effect becomes more important. A simple estimation of N_b depends on the local density and the volume that encloses the ensemble: $N_b \propto \rho R_b^3$. In order to estimate R_b, the number of blockaded atoms must be found. For an ensemble of N_b blockaded atoms, $R_b = (C_6/\sqrt{N_b}\Omega_0)^{1/6}$. In turn, an excited atom blocks all other atoms within a spherical volume $(4/3)\pi R_b^3$, so for a uniform distribution ρ, $N_b = (4/3)\pi R_b^3 \rho$. These two equations can be solved leading to $R_b \propto \rho^{-1/15}$ and $N_b \propto \rho^{4/5}$. The plots in Figure 2.5 are the results for R_b and N_b as a function of density for ranges which are similar to those found in the MOT used by [50]. The lines were generated by the following equation:

$$N_b = \alpha \left(\frac{4\pi}{3} \sqrt{\frac{C_6}{\Omega_0}} \rho \right)^{4/5}, \tag{2.22}$$

where α is a fit parameter to match the data generated by the many body wavefunction calculations. We used an $\alpha = 1.075$. As expected, as the density increases, R_b decreases and the N_b increases. The size of the R_b is dependent on the local density. The difference in R_b from the lowest density edges of the MOT to the peak density in the center is substantial. The difference in N_b from peak to edge densities is also quite large, which means that excited atoms on the edges of the MOT will oscillate many times slower than ones near the center. We introduce a scaled distance $\xi = \sqrt{r_c^2/\sigma^2 + z^2/\Delta z^2}$ from the center of the MOT to study the spacial locations of the excitations within the MOT. The plots in Figure 2.6 are the N_{exc} in a volume $4\pi\xi^2\Delta\xi$ (where $\Delta\xi \ll \xi$) and the N_b at a given scaled distance ξ. Most of the excited atoms occur at about $\xi = \sqrt{5}$, which is about 6.7×10^{-3} times the peak density. The plot in Figure 2.6.b is both N_b and N_{exc} as a function of ξ. As the atoms are found further from the center of the MOT the number of excited atoms per volume generally increases and the number of atoms that are blocked greatly

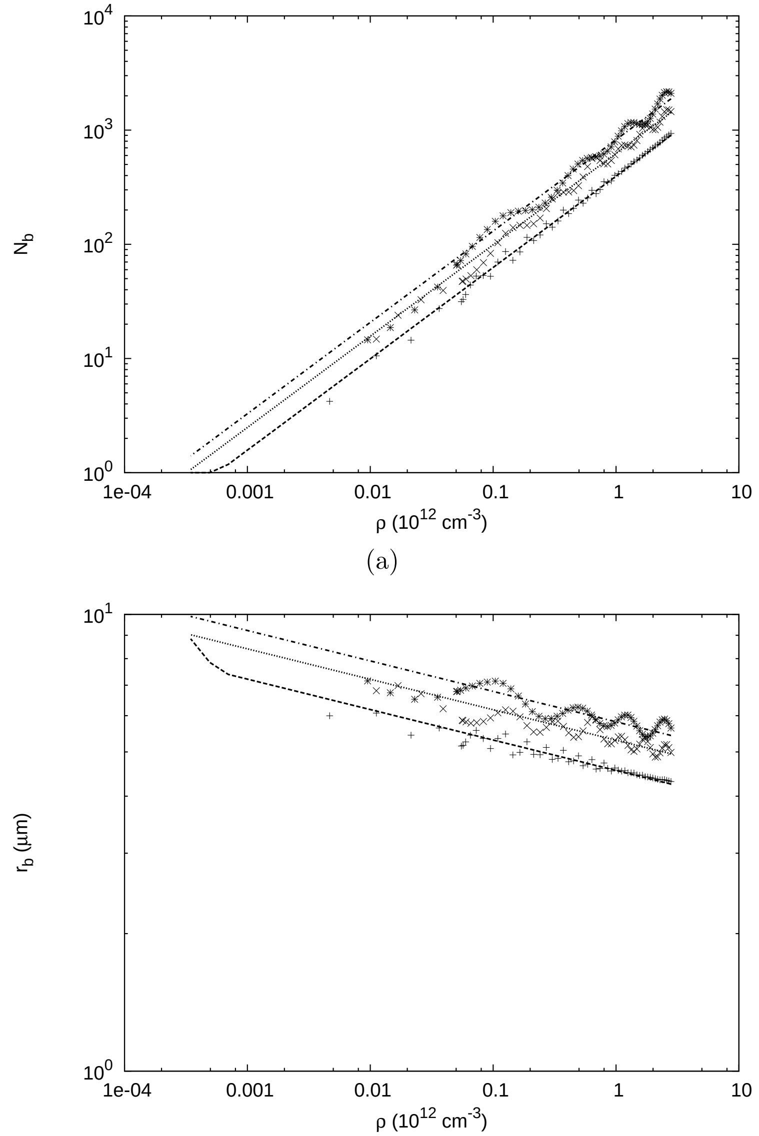

(a)

(b)

Figure 2.5: (a) is the number of blocked atoms per excited atom, N_b, as a function of the density at various Ω_0. (dashed, +) $\Omega_0 = 210$ kHz, (dotted, ×) $\Omega_0 = 210/\pi$ kHz, and (dash-dot, *) $\Omega_0 = 210/(2\pi)$ kHz. The lines were generated using the fact that $N_b \propto \rho^{4/5}$ and the points were generated by the many body wavefunction at $\tau = 20\mu$s. (b) is the blockade radius, R_b, as a function of the density at the same Ω_0's as part (a).

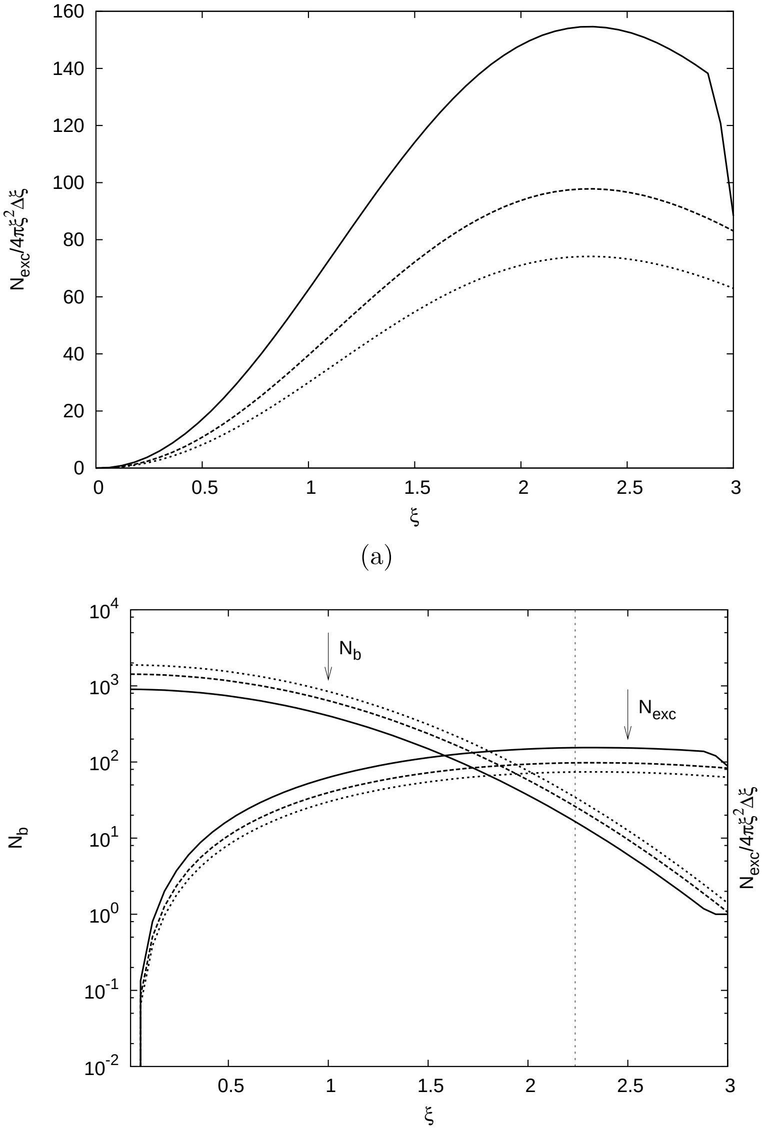

(b)

Figure 2.6: (a) is the number of excited atoms N_{exc} in a volume $4\pi\xi^2\Delta\xi$ found at a scaled distance $\xi = \sqrt{r_c^2/\sigma^2 + z^2/\Delta z^2}$ from the center of the MOT at various Ω_0. (full) $\Omega_0 = 210$ kHz, (dashed) $\Omega_0 = 210/\pi$ kHz, and (dotted) $\Omega_0 = 210/(2\pi)$. $\Omega_0 = 210/(2\pi)$ kHz. (b) is N_b and $N_{exc}/4\pi\xi^2\Delta\xi$ as a function of ξ. (full) $\Omega_0 = 210$ kHz, (dashed) $\Omega_0 = 210/\pi$ kHz, and (dotted) $\Omega_0 = 210/(2\pi)$. The vertical line is at $\xi = \sqrt{5}$, where $N_{exc}/4\pi\xi^2\Delta\xi$ is maximum.

decreases from the N_b at the peak density. At $\xi = 0$, $N_b \sim 10^3$, while at $\xi = \sqrt{5}$, $N_b \sim 10$ which means the majority of the oscillations in the system will be about a factor of ten times slower than oscillations at the peak.

2.7.2 Effects of density variation

Even within a volume contained by R_b, the density can vary enough to have an effect. For example, if $R_b \sim 6\mu$m, the diameter of a blockade is approximately σ. This means that density (and correspondingly N_b) can vary by an order of magnitude within a blockade region. This variation in time scales and R_b indicates that in order to correctly model the entire gas, the non-uniform density distribution of the MOT must be accounted for. In other words, the local fraction excited will depend on the local density ρ and the excitation time τ. Unfortunately, the many-body wavefunction calculations utilize wrapped boundary conditions and a mean field in order to make convergence possible, both of which depend on a constant density across the simulated volume.

Given a density distribution, the total number of atoms excited to a Rydberg state after an excitation time τ will be:

$$N_{exc}(\tau) = \int P_e(\rho, \tau)\rho \, \mathrm{d}V, \tag{2.23}$$

where $P_e(\rho, \tau)$ is the fraction excited after excitation time τ for a density ρ. We calculated $P_e(\rho, \tau)$ for various densities by solving the many-body wavefunction, but in these simulations we assumed that the density does not vary strongly within a blockade region. This condition does not hold up when using the parameters in Ref. [50] and will lead to a loss of accuracy in the calculations, but we still hoped for qualitative agreement with experiment. If, as in our case, the density distribution is Gaussian, this can be rewritten as

$$N_{exc}(\tau) = 2\pi\sigma^2\Delta z \int P_e(\rho,\tau)\sqrt{\ln(\rho_0/\rho)}\,\mathrm{d}\rho. \tag{2.24}$$

In order to accurately integrate numerically over the density, we used a simple linear interpolation to get $P_e(\rho,\tau)$ for values between the calculated values. The accuracy of this integration is determined by the number of calculated density points and the grid size in density.

Simple Sinusoidal Model

As a check, we also developed a simple model based on the idea that a strongly blockaded ensemble of N_b atoms oscillates at $\sqrt{N_b}\Omega_0$. For the large densities looked at in this section, the number of blockaded atoms for a certain density varies in a Poissonian fashion from trial to trial. Using these criteria, an estimate of the fraction excited as a function of ρ and τ can be found:

$$P_{e,est}(\rho,\tau) = \left\langle \frac{1}{N_b(\rho)} \sin^2 \sqrt{N_b(\rho)}\frac{\Omega_0}{2}\tau \right\rangle_{N_b}, \tag{2.25}$$

where the brackets, $\langle \cdots \rangle_{N_b}$, indicate an average over a Poissonian distribution in N_b. Figure 2.7 shows a comparison between the fraction excited versus time for the many-body wavefunction calculation and the simple sinusoidal model. The left figure is for a fixed relatively low density and the right is a fixed high density. As expected, the time dependence of the two models is similar, but the simple model tends to slightly overestimate the fraction excited. The oscillations in the many-body wavefunction calculations are similar to the sinusoidal model, indicating the coherent nature of the system. At a higher density these oscillations are noticeably faster, but still coherent. If the density across the system does not drastically change, the collective Rabi oscillation is evident. If the density does change, the resulting high $\sqrt{N_b}$ fluctuations will mask the collective excitations.

Monte Carlo model

Due to the small fraction of atoms excited to a Rydberg state, people have applied a Monte Carlo (MC) approach toward studying this system. We used a very simple MC model that only allowed for excitations, no de-excitations. We started by randomly placing 15 000 000 atoms in a Gaussian distribution with the same parameters as above. For every time step δt, each atom j has a probability of being excited given by:

$$P_j = \frac{\pi}{2}\Omega_0 \frac{(\Omega_0/2)^2}{(\Omega_0/2)^2 + \bar{V}_j^2}\delta t, \tag{2.26}$$

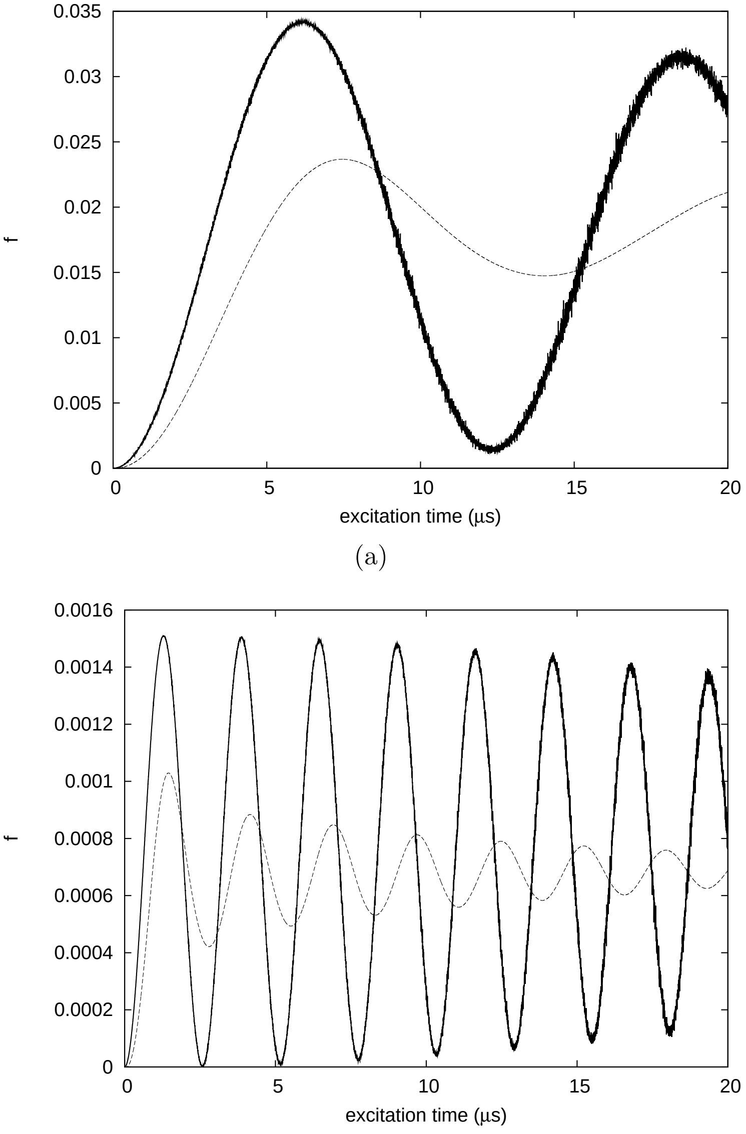

(a)

(b)

Figure 2.7: The fraction excited versus excitation time for the many-body wavefunction calculation (dashed) and the simple $\sin^2$ model (full). (a) is for a low density ($5.6 \times 10^{10}\text{cm}^{-3}$) and (b) is for a high density ($2.8 \times 10^{12}\text{cm}^{-3}$). Both calculations were done using $\Omega_0 = 210/\pi$ kHz

where $\bar{V}_j = \sum_k V_{jk} = \sum_k -C_6/r_{jk}^6$ is the energy shift between atom j and every other excited atom. $\bar{V}_j$ is updated every time a new atom has been excited. This MC model essentially blockades an atom if $|\bar{V}_j| \gg \Omega_0$ which is consistent with the definition of being blockaded as previously described in Secs. 2.4.1 and 2.7.1. The MC model has the advantage of not needing to be convolved, so it can serve as a quantitative check on the previous two methods. The overestimation of the simple $\sin^2$ model is seen when we convolve the simple model over the density distribution as in Figure 2.7.2, but the two calculations reach the saturation number of Rydberg atoms at about the same excitation time.

We also compared the convolved data to recent experimental data [50]. The experiment used a Rabi frequency of $\Omega_0 = 210$ kHz. The simulated results, while having the correct qualitative shape and within about a factor of 2 in the saturated number of excited atoms, is off when it comes to the time scale for saturation. We repeated these calculations using two slower Rabi frequencies in an attempt to match the times cale of the experiment. Unfortunately, as Ω_0 is decreased so does the N_{exc}. This trend was consistent across all three models. We could not perform a calculation that would match both the time dependence and the N_{exc} of the experiment with any of the available adjustable physical parameters. This suggests that only taking into account excited pair interactions and laser interactions while not accounting for a strong variance in density across a blockade region, is not adequate enough to correctly understand this system.

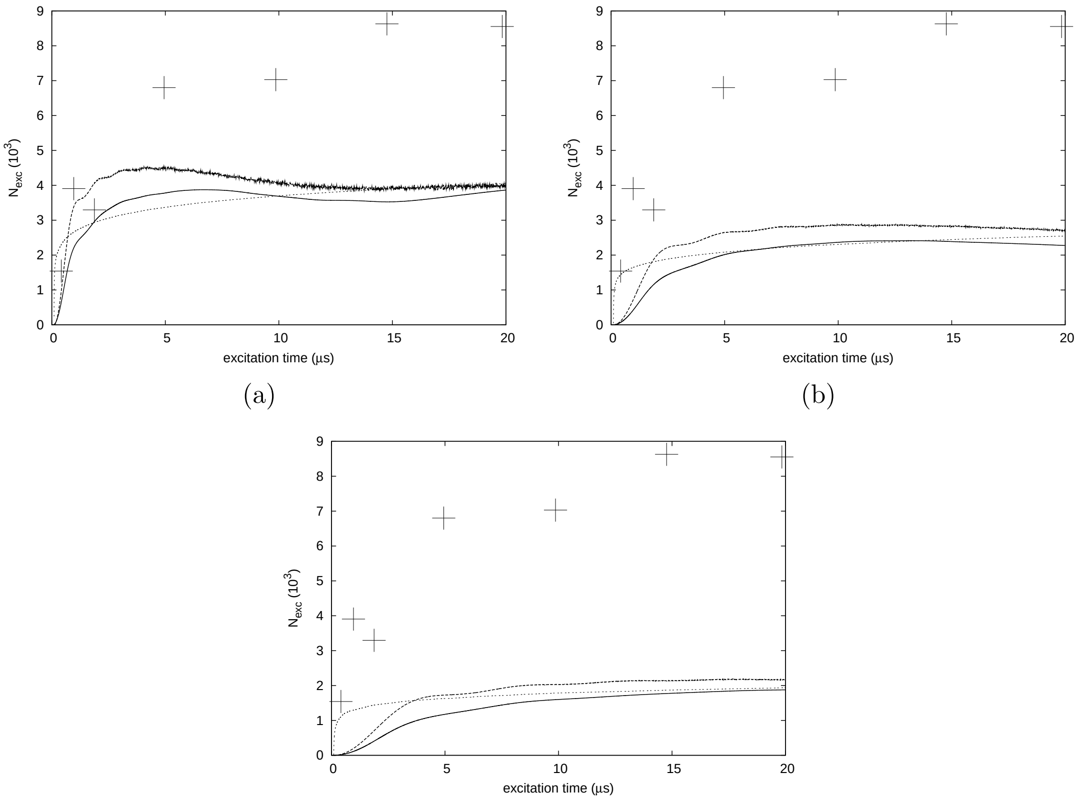

(a) (b)

(c)

Figure 2.8: A comparison between the experimental data and the three models: the number excited versus excitation time for the convolved many-body wavefunction calculation (full), the simple $\sin^2$ model (dashed), and the MC model (dotted). The (+) are experimental data points (Ω_0 = 210 kHz). (a) was calculated using a Rabi frequency Ω_0 = 210 kHz, (b) $\Omega_0 = 210/\pi$ kHz and (c) using $\Omega_0 = 210/(2\pi)$ kHz.

2.8 Conclusions

By solving for the many body wavefunction we were able to calculate many useful quantities such as the 2D two particle correlation function which shows the angular dependence of the first order dipole-dipole interaction. When using the dipole-dipole interaction to investigate the Q parameter or anything else that requires a well defined blockade region, special care is needed to make sure that the critical angle $\theta_{jk} \approx 55^\circ$ is unattainable to pairs of atoms. We also calculated the Mandel Q-parameter, a useful quantity for measuring the degree to which a gas is blockaded. The non-excited atoms within a blockade region still affect atoms outside R_b, thus even when few atoms are excited and the gas is dense enough, the system is still correlated. The Q-parameter can also be used to determine the reduction in the number of two-level systems remaining in the gas. If atoms are placed on a one dimensional lattice, and excited in a manner that maximizes the number excited, the average maximum number excited grows smoothly as a function of the lattice length. The size of R_b can be seen, however, if the probability of finding N_e is plotted as a function of L. Since we solved for the wavefunction, we were able to examine the use of groups of blockaded atoms as phase gates. We calculated the phase accumulated during a sequence of pulses and generated the errors acquired by a non-perfect phase gate as a function of the interaction energy. In order to operate a phase gate that returns $\Delta\phi > 0.9\pi$, a rather large interaction energy is required.

We also performed three very different model calculations that are all in good qualitative agreement with each other. For such a large system of atoms, being within a factor of 2 in both time scale and N_{exc} is encouraging. However, the calculations do not agree well enough with experimental data to suggest that the underlying physics of the system is completely understood. The biggest concern is the different time scales for saturation between the computational models and the experimental data. Since we were not able to take into account the density variations over R_b, the first step towards developing a more accurate model might be to develop a method that can account for this density variance and also converge within feasible limits. This would present a challenge to any mean field calculations, as the value of the mean field energy shift would depend on the location of the pseudoparticle within the MOT. The actual shape of the gas is also very important if accurate models are to be developed; in all of the simulations the time scale is largely determined by the slower oscillations found toward the edges of the MOT where the density is lower.

CHAPTER 3

COHERENT HOPPING OF EXCITATION

3.1 Introduction

There have been many recent experimental and theoretical investigations of the interactions between Rydberg atoms. These possibly strong interactions can lead to interesting many-body effects if the energy separation between excited states is small and outside sources of decoherence are minimized. Since atoms are neutral, the typical interaction potential between them is the dipolar interaction which is proportional to the size of atoms squared divided by the cube of distance between them. Since the size of an atom scales as n^2, where n is the principal quantum number, the interaction scales as $(nn')^2/R^3$. The large size of Rydberg atoms and the density of the atoms determines the relevant energy scales.

There are numerous experiments that have been successful in exciting atoms to Rydberg states that allow for the resonant exchange of energy to occur [2,8,9,29,31, 59,60]. In other words, a pair of atoms in states A and B can interact in a manner that converts $A \rightarrow A'$ and $B \rightarrow B'$. The energy cost for this transition must be very small; in other words energy must be roughly conserved: $E_A + E_B \simeq E_{A'} + E_{B'}$. These experiments were all done in environments cold enough for the motion of the atoms to be minimal, and the transitions were coherent and in both directions. The spectrum of Rydberg atoms that allow these resonant transfers is fundamentally different than the single atom case; some many-body processes are occurring [9, 52].

In this chapter we present the results of simulating a cold Rydberg gas that has been spatially ordered. The atoms are placed in specific areas and are not allowed to move during important time scales. While this is not experimentally realistic, the underlying physics should still be of interest in probing the nature of the coherent energy exchange. For example, we calculated band structures for a single p state Rydberg atom in various arrays of s state Rydberg atoms.

We also investigated finite systems where the location of each atom is not exact, but randomly placed within small regions. These regions are then arranged in regular patterns. Within each region a single atom will start in the state A or B. This setup is experimentally viable as long as the width of an excitation beam is smaller than the distance between the next beam. Our simulations were able to study the effects of defects in the optical lattice.

As in most Rydberg-Rydberg interactions, we employed an essential states picture that includes only the states that are degenerate or nearly degenerate. As long as the separation between energy states is not too small this approximation is accurate. Since the energy difference between two states scales as $1/n^3$, the essential states approximation loses accuracy as n increases. If the transition rate between states is longer than the timescales of the simulation we can effectively ignore these transitions. The applicability of the essential states model is justified in section 3.6. We will use atomic units throughout this chapter except where noted.

3.2 Theory

The Hamiltonian for two interacting Rydberg atoms is

$$\hat{H} = \hat{H}_1 + \hat{H}_2 + V_{12}, \tag{3.1}$$

where $\hat{H}_1$ and $\hat{H}_2$ are the Hamiltonians for the two Rydberg atoms and V is the interaction potential between the two Rydbergs. In order to describe V we define the following coordinates: $\vec{R}_{12}$ (the vector between the nuclei of atoms 1 and 2), $\vec{r}_1$ (the vector between the nucleus and the electron of atom 1), and $\vec{r}_2$ (the vector between the nucleus and the electron of atom 2). We will assume that the Rydberg atoms are not so close that the two electrons will overlap, so we do not have to worry about symmetrization of the wavefunction The interaction potential is now:

$$\begin{aligned} V_{12} &= \frac{1}{R_{12}} - \frac{1}{\left|\vec{R}_{12} - \vec{r}_1\right|} - \frac{1}{\left|\vec{R}_{12} + \vec{r}_2\right|} + \frac{1}{\left|\vec{R}_{12} + \vec{r}_2 - \vec{r}_1\right|} \\ &\simeq \frac{\vec{r}_1 \cdot \vec{r}_2 - 3(\vec{r}_1 \cdot \hat{R}_{12})(\vec{r}_1 \cdot \hat{R}_{12})}{R_{12}^3}. \end{aligned} \tag{3.2}$$

In this chapter we will only look at the lowest order nonzero coupling, which is the dipole-dipole interaction shown in Eq. 3.2.

3.2.1 Field free

If the atoms are excited in a field free environment then eigenstates will have a well defined angular momentum, therefore the coupling should be calculated between states of specific angular momentum on each atom. In order to evaluate these matrix elements we rewrote Eq. 3.2 in terms of separate radial and angular pieces. Using angular momentum relationships

$$V_{12} = -8\pi\sqrt{\frac{2\pi}{15}}\frac{r_1 r_2}{R_{12}^3}\sum_{\mu=-2}^{2}\left[Y_1(\hat{r}_1)Y_1(\hat{r}_2)\right]_\mu^2 Y_{2\mu}^*(\hat{R}_{12}), \tag{3.3}$$

where $Y_{\ell m}$ is a spherical harmonic function, and $\left[Y_1(\hat{r}_1)Y_1(\hat{r}_2)\right]_\mu^2$ means the two spherical harmonics are coupled to a total angular momentum of 2 and the azimuthal μ via the standard Clebsch-Gordon coefficients.

In the absence of an electric field, atoms in states A and B, respectively, are eigenstates of angular momentum. These eigenstates have a degeneracy of $2\ell_A + 1$ and $2\ell_B + 1$. When the two atoms are coupled together through V there are $2(2\ell_A + 1)(2\ell_B + 1)$ available states. The factor of 2 out front is a result of the fact that the two atoms can either be arranged $|AB\rangle$ or $|BA\rangle$. Since the dipolar interaction, V, depends on the first order spherical harmonic Y_1 for each atom, the diagonal terms in the coupling matrix are all zero ($\langle AB|V|AB\rangle = 0$). The Y_1 dependence also means that A couples to B only when $|\ell_A - \ell_B| = 1$, and if we set $\hat{R}_{12} = \hat{z}$, then $m_A + m_B$ is a conserved quantity.

The wavefunction for a Rydberg atom can be written in terms of a radial piece, $R_{n\ell}(r)$, and an angular piece, $Y_{\ell m}(\hat{r})$:

$$\psi_{n\ell m} = \frac{R_{n\ell}(r)}{r} Y_{\ell m}(\hat{r}). \tag{3.4}$$

The matrix element between states $\langle AB|$ and $|B'A'\rangle$ is given by

$$\begin{aligned} V_{AB,B'A'} &= -8\pi\sqrt{\frac{2\pi}{15}}\frac{(d_{n_A\ell_A,n_B\ell_B})^2}{R_{12}^3}\sum_{\mu=-2}^{2} Y_{2\mu}^*(\hat{R}_{12})\langle \ell_A m_A, \ell_B m_B| \\ &\times \; [Y_1(\hat{r}_1)Y_1(\hat{r}_2)]_\mu^2 \, |\ell_B m'_B, \ell_A m'_A\rangle, \end{aligned} \tag{3.5}$$

where $\langle AB|$ means that atom 1 is $\langle n_A \ell_A m_A|$ and atom 2 is $\langle n_B \ell_B m_B|$, and $|B'A'\rangle$ means that atom 1 is $|n_B \ell_B m'_B\rangle$ and atom 2 is $|n_A \ell_A m'_A\rangle$. The dipole matrix element d is defined as

$$d_{n_A\ell_A,n_B\ell_B} = \int_0^\infty r R_{n_A\ell_A}(r) R_{n_B\ell_B}(r)\, dr. \tag{3.6}$$

In this chapter we will focus on the interaction between an s state and a p state. This simplifies the math a great deal, and nonzero matrix elements of the coupling potential now become

$$\begin{aligned} V_{1m,00;001m'} &= \sqrt{\frac{8\pi}{3}}\frac{(d_{n_A1,n_B0})^2}{R_{12}^3}(-1)^{m'} \\ &\times \begin{pmatrix} 1 & 1 & 2 \\ m & -m' & m'-m \end{pmatrix} Y_{2,m'-m}(\hat{R}_{12}), \end{aligned} \tag{3.7}$$

where $(\cdots)$ is the usual $3-j$ coefficient.

3.2.2 Static electric field

Another simple case to look at is the Rydberg-Rydberg interactions in a strong static electric-field pointed in the z direction. This electric field breaks the spherical symmetry and creates states with substantial dipole moments. As opposed to the field free case, there are now nonzero diagonal matrix elements of the coupling potential. Another difference is the number of states that can be coupled together through V. While this can possibily lead to interesting physics, it does complicate the study between two atoms. In this case we will choose two states that couple strong enough to allow us to ignore possible coupling to other states.

The Rydberg atoms in the static electric-field are in Stark states, and the dipole interaction between them causes a mixing with other Stark states within in the same n manifold [11]. This mixing can be suppressed by exciting both of the atoms to the highest (or lowest) energy states of the Stark manifold, and by increasing the separation between atoms. For the rest of the subsection we will only use the highest Stark states so we can label atoms by only the principal quantum number n. As in the previous subsection, the dipole matrix elements between states in different

n-manifolds is of utmost importance:

$$\begin{aligned}
\langle n|z|n\rangle &\simeq \frac{3}{2}n^2 \\
\langle n-1|z|n\rangle &\simeq \frac{1}{3}n^2 \\
\langle n-1|z|n+1\rangle &\simeq \frac{1}{9}n^2 \\
\langle n|x|n'\rangle = \langle n|y|n'\rangle &= 0.
\end{aligned} \tag{3.8}$$

Notice that the x and y components of the dipole interaction are 0 in this approximation. In order to investigate the largest interactions, we will only use the case where the $|n-n'| = 1$.

For two atoms the diagonal elements of the coupling matrix are given by:

$$V_{n,n';n,n'} = V_{n',n;n',n} = \left(\frac{3nn'}{2}\right)^2 \frac{1-3(\hat{R}_{12}\cdot\hat{z})^2}{R_{12}^3}, \tag{3.9}$$

and the off-diagonal elements are given by

$$V_{n,n';n',n} = V_{n',n;n,n'} = \left(\frac{nn'}{3}\right)^2 \frac{1-3(\hat{R}_{12}\cdot\hat{z})^2}{R_{12}^3}. \tag{3.10}$$

3.2.3 Coherence

In order for the coherent hopping of character from one atom to another to occur the electron states of the Rydberg atoms cannot couple to outside degrees of freedom. As long as the simulated system is isolated from free electrons or photons then the only source of decoherence will be the relative motion of the atoms. This source of decoherence can be ignored as long the atoms do not move very much during relevant time periods [26].

3.3 Simple band structures

Coherent hopping can be observed when all of the atoms are on a regular lattice. We started by studying one of the simplest examples: one p atom in a group of s atoms. Since there are three types of p states ($m = -1, 0, 1$), and there is only one p atom in our simulations, the system can be fully described by two quantum numbers: $|\beta m\rangle$. Atom β has p character with an azimuthal quantum number m while all other atoms are in the s state. Since there are three types of p states, this also means that three modes of hopping are possible, so we label each mode by α. Since we have an ordered lattice of atoms, a natural representation of an eigenstate of the system can expressed as a superposition of Bloch-type waves:

$$\psi_{\vec{k},\alpha} = \frac{1}{\sqrt{N}} \sum_{\beta' m'} e^{i\vec{k}\cdot\vec{R}_{\beta'}} U_{m'\alpha}(\vec{k}) |\beta' m'\rangle. \tag{3.11}$$

In Eq. 3.11, $\vec{k}$ is the wavenumber, N is the total number of atoms, $\vec{R}_\beta$ is the position of atom β, and $U_{m\alpha}$ is a unitary matrix for any fixed $\vec{k}$. Using Eq. 3.1 the time-independent Schrödinger equation becomes:

$$\hat{H}\psi_{\vec{k},\alpha} = \epsilon_\alpha(\vec{k})\psi_{\vec{k},\alpha}, \tag{3.12}$$

where $\epsilon_\alpha(\vec{k})$ is the eigenvalue of $\psi_{\vec{k},\alpha}$. Since the diagonal elements of the Hamiltonian are the same for every state they can be removed while still maintaining the relevant physics. By projecting the state $\langle \beta m|$ onto Eq. 3.12 and using the matrix elements from Eq 3.7 we get:

$$\sum_{m'} \mathcal{H}_{mm'}(\vec{k}) U_{m'\alpha}(\vec{k}) = U_{m\alpha}(\vec{k})\epsilon_\alpha(\vec{k}), \tag{3.13}$$

where

$$\begin{aligned} \mathcal{H}_{mm'}(\vec{k}) = & - \gamma \delta x^3 (-1)^{m'} \begin{pmatrix} 1 & 1 & 2 \\ m & -m' & m'-m \end{pmatrix} \\ & \times \sum_{\beta' \neq \beta} e^{-i\vec{k}\cdot\vec{R}_{\beta\beta'}} \frac{Y_{2,m-m'}(\hat{R}_{\beta\beta'})}{R^3_{\beta\beta'}}, \end{aligned} \tag{3.14}$$

with δx being the spacing between atoms and $\vec{R}_{\beta\beta'} = \vec{R}_\beta - \vec{R}_{\beta'}$.

In order to examine the band structure of this system we will have to extend it toward the $N \longrightarrow \infty$ limit. This is accomplished by increasing the number of atoms in the above sum until convergence is achieved.

Since the trace of the $\mathcal{H}_{mm'}$ matrix is 0 for all $\vec{k}$, the sum of the band energies must be 0. So when $\vec{k} \sim \vec{0}$ there must be bands with positive and negative effective mass. A wavepacket centered around $\vec{k}_0$ has the group velocity for band α:

$$\vec{v}_\alpha(\vec{k}_0) = \left[\vec{\nabla}_{\vec{k}} \epsilon_\alpha(\vec{k}) \right]_{\vec{k}=\vec{k}_0}. \tag{3.15}$$

3.3.1 Linear lattice

The simplest lattice is a line of equally spaced atoms. The band structure for this system can be seen in Fig. 3.1. Since it is possible to propagate two different ways in a transverse manner (where the lobes of the p orbital are perpendicular to the line of atoms) two of the bands will be degenerate. When k is small the bands have a quadratic dependence: $\epsilon_\alpha \sim A_\alpha + B_\alpha k^2$. Using Eq. 3.15, the magnitude of the group velocity is proportional to k at small k. Some bands will have a particle character (positive group velocity proportional to $\vec{k}$ for small $\vec{k}$) while others will have hole character (negative group velocity proportional to $\vec{k}$ for small $\vec{k}$).

The two degenerate transverse bands have hole character while the longitudinal band has particle character. This band structure exactly matches the band structure of a linear array of optically driven plasmons in metallic nanoparticles [46]. Since the transverse bands are degenerate and the sum of the band energies must be 0, the two bands will cross each other only at $\epsilon = 0$. If the lattice is perfect then the transverse and longitudinal waves are not coupled to each other; the bands exactly cross. Defects in the lattice could cause a breaking of the degeneracy in the transverse case, and then the exact crossing would be replaced by an avoided crossing. If the effect of imperfections is small then the coupling between transverse and longitudinal bands would be localized to $\vec{k}$ where $\epsilon(\vec{k}) \sim 0$.

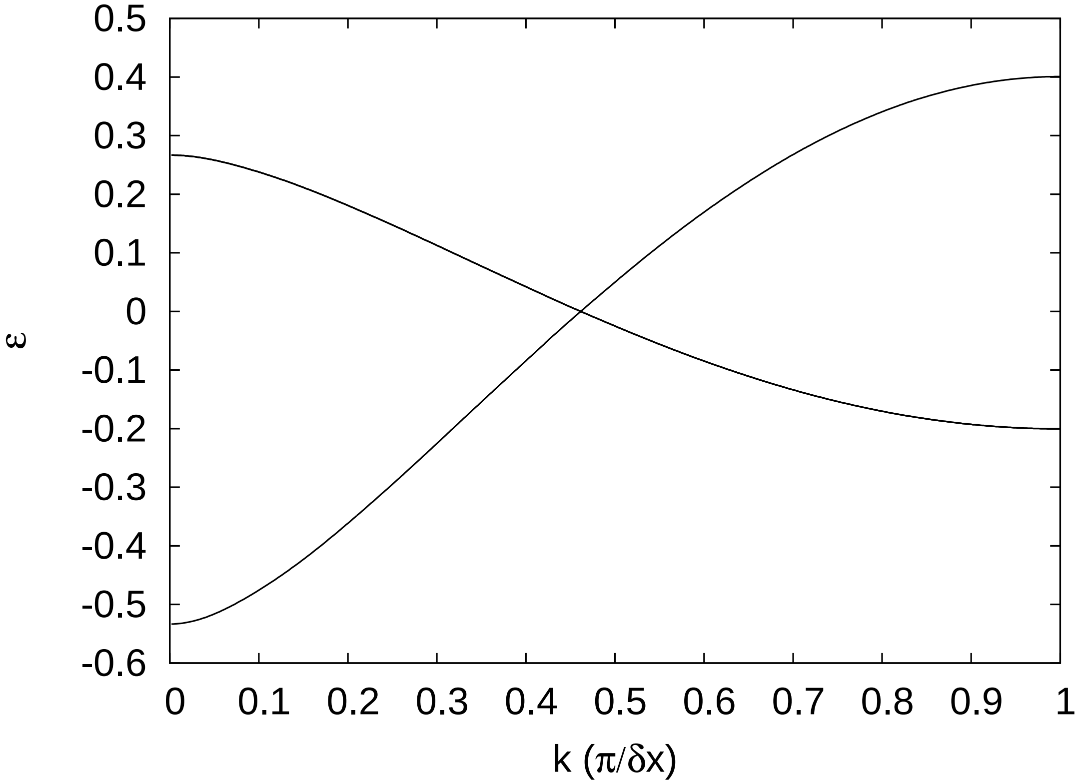

Figure 3.1: The scaled band energy (band energy divided by $\sqrt{8\pi/3}(d_{n_a1,n_b0})^2/\delta x^3$) as function of the wavenumber k for a linear array of atoms with one p state and the rest s states.

3.3.2 Square lattice

The next logical extension was to look at the bands for a square lattice $\epsilon_\alpha(k_x, k_y)$. The Brillouin zone for a square lattice has three special points: the center (Γ) $(k_x, k_y) = (0, 0)$, the center of the side (X) $(\pi/\delta x, 0)$, and the corner (M) $(\pi/\delta x, \pi/\delta y)$. A common way of presenting the bands is to plot the energy along the three lines that connect the special points: Δ connects Γ and X, Σ connects Γ to M, and Z connects X to M. These are shown in Fig. 3.2. The band energies are shown in Fig. 3.3 for the special lines as a function of $k = |\vec{k}| = \sqrt{k_x^2 + k_y^2}$. The nature of the eigenvectors allow for the labeling of the different bands. At the center and corner of the Brillouin zone, Γ and X respectively, two of the bands are degenerate and one is nondegenerate. The nondegenerate band must correspond to the p state having $m = 0$ character since this is the state whose wavefunction has a nodal plane in the xy plane. This is analogous to a transverse wave, i.e., the lobes of the p state are perpendicular to k. This band exactly crosses the others since the $m = 0$ character does not couple to states with $m = \pm 1$ character. The two degenerate bands near the center of the Brillouin zone have the lobes of the p state in the xy plane. The band that rises linearly with k has a p state with lobes perpendicular to $\vec{k}$ (transverse-like) while the other band has lobes parallel to $\vec{k}$ (longitudinal-like).

The bands near $k = 0$ with a transverse nature have band energies that change linearly with respect to k. Using Eq. 3.15 it becomes evident that the group velocity will be constant near $k = 0$, and does not depend on the direction of propagation. Therefore these transverse bands behave like neither particles or holes, but rather

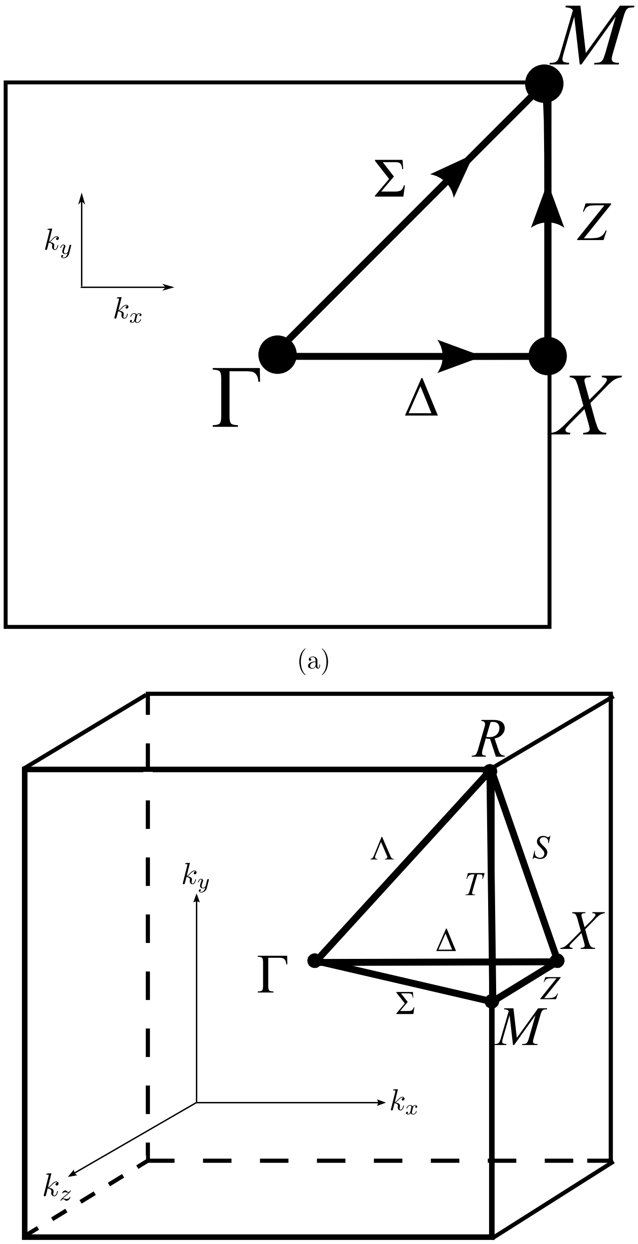

(a)

(b)

Figure 3.2: (a) is the Brillouin zone for a square lattice with special points and paths. (b) is the Brillouin zone for a simple cubic lattice with special points and paths.

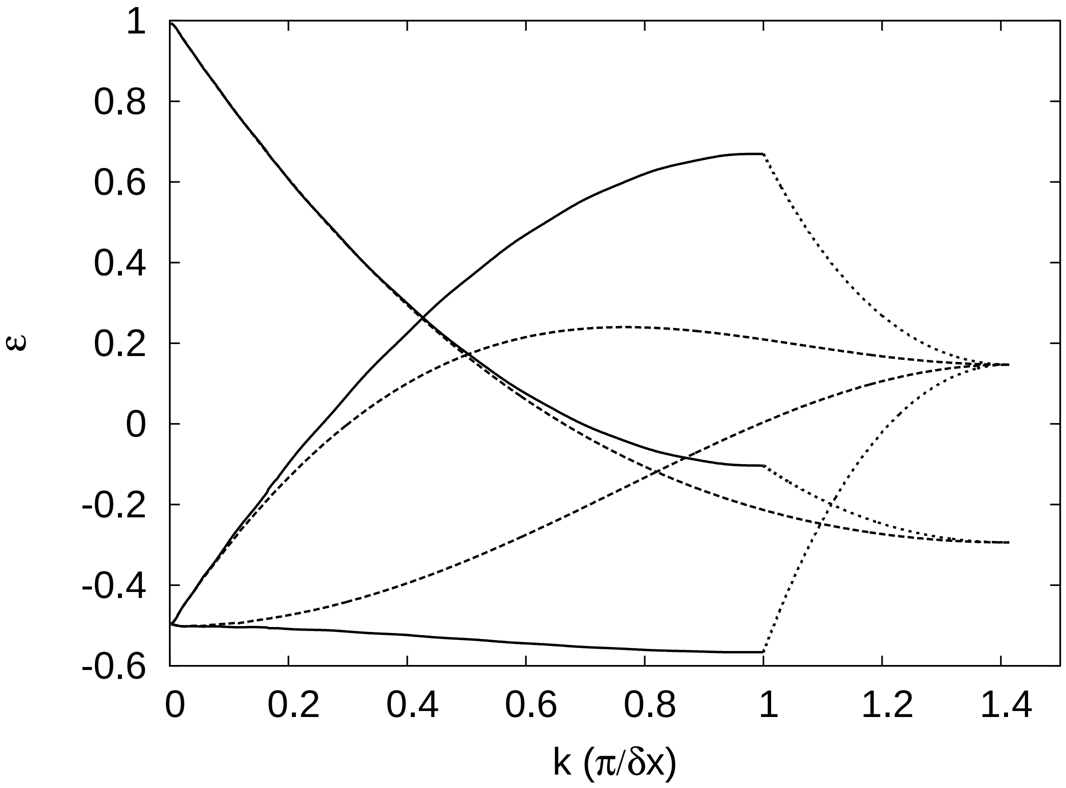

Figure 3.3: The scaled band energy (band energy divided by $\sqrt{8\pi/3}(d_{n_a1,n_b0})^2/\delta x^3$) as function of the wavenumber k for a square array of atoms with one p state and the rest s states.

like photons or phonons. It is interesting to note that the nondegenerate band has a negative group velocity, which means that the a wavepacket moves in the opposite direction to the wavenumber. The longitudinal wave acts like a hole or a particle depending on $\vec{k}$.

3.3.3 Cubic lattice

The Brillouin zone for a simple cubic lattice has four special points: the center of the cube (Γ) $(k_x, k_y, k_z) = (0, 0, 0)$, the center of a face ($X$) $(\pi/\delta x, 0, 0)$, the center of an edge (M) $(\pi/\delta x, \pi/\delta x, 0)$, and a corner ($R$) $(\pi/\delta x, \pi/\delta x, \pi/\delta x)$. We computed energies along six paths that connect these points: Δ which connects Γ to X, S which connects X to R, T which connects M to R, Σ which connects Γ to M, Z which connects X to M, and Λ which connects Γ to R.

In Fig. 3.4 we plotted the band energies $\epsilon_\alpha(k_x, k_y, k_z)$ as a function of $k = \sqrt{k_x^2 + k_y^2 + k_z^2}$. Again the character of the eigenvalues let us label the different bands. All four of the special points have degenerate states and the Δ, T, and Λ paths also have degenerate bands.

While the cubic lattice is very simple, the resultant band structure it not. As with the square lattice, the particle or hole nature of the bands is dependent on the direction of $\vec{k}$ near $k \sim 0$.

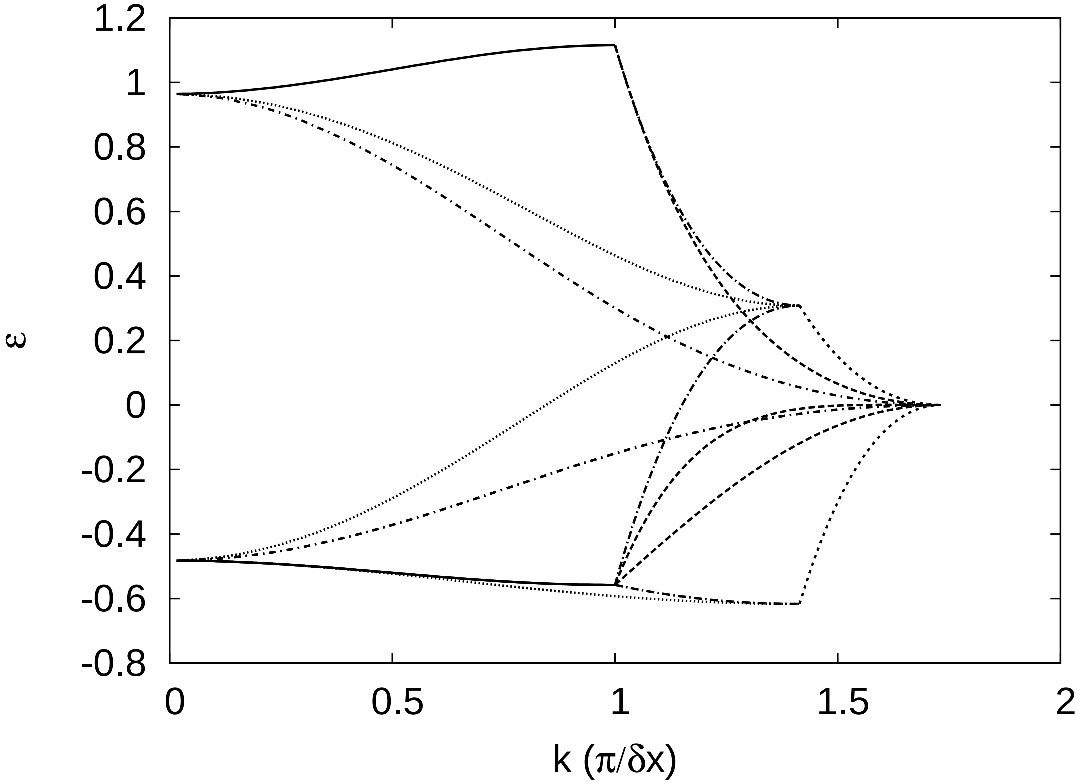

Figure 3.4: The scaled band energy (band energy divided by $\sqrt{8\pi/3}(d_{n_a1,n_b0})^2/\delta x^3$) as function of the wavenumber k for a cubic array of atoms with one p state and the rest s states.

3.4 Hopping in a small non-perfect lattice

The actual hopping of a Rydberg excitation can be seen experimentally by using a CCD camera and state-selective field ionization. Since the states can be distinguished by ramping on an electric field, we assumed the atoms are always in a strong electric field that places the Rydberg atoms into an extreme Stark state. In this section we will study the case where one atom is excited to the $n = 61$ state and the rest of the atoms are in the $n = 60$ state. Each atom is randomly placed in a 27 μm^3 cube and each cube is separated by a center-to-center distance of 20 μm. In every case we also had the electric field pointed perpendicular to the line or plane of atoms ($\hat{z} \cdot \hat{R} = 0$).

The first case we simulated was a line of atoms along the x-axis with the $n = 61$ atom starting in the leftmost region. In Fig. 3.6.a we plotted the result for the 2 atoms. The solid line is the probability of finding the $n = 61$ state in the left region, while the dashed line is the probability of finding it in the right region. If the spacing between atoms was fixed then the probability would oscillate between 0 and 1 at a fixed frequency ω that depended on the distance. Since the atoms are not evenly spaced, but randomly placed within regions, damping occurs. This damping is a direct result of averaging over the range of allowed frequencies.

In Fig. 3.6.b we plotted the results for 6 atoms, with the leftmost atom being in the $n = 61$ state. Again the solid line is the probability of finding the $n = 61$ in the leftmost region, the dashed is the probability of finding it in the adjacent region, and the dotted line is the probability of finding it in the rightmost region. The coherent

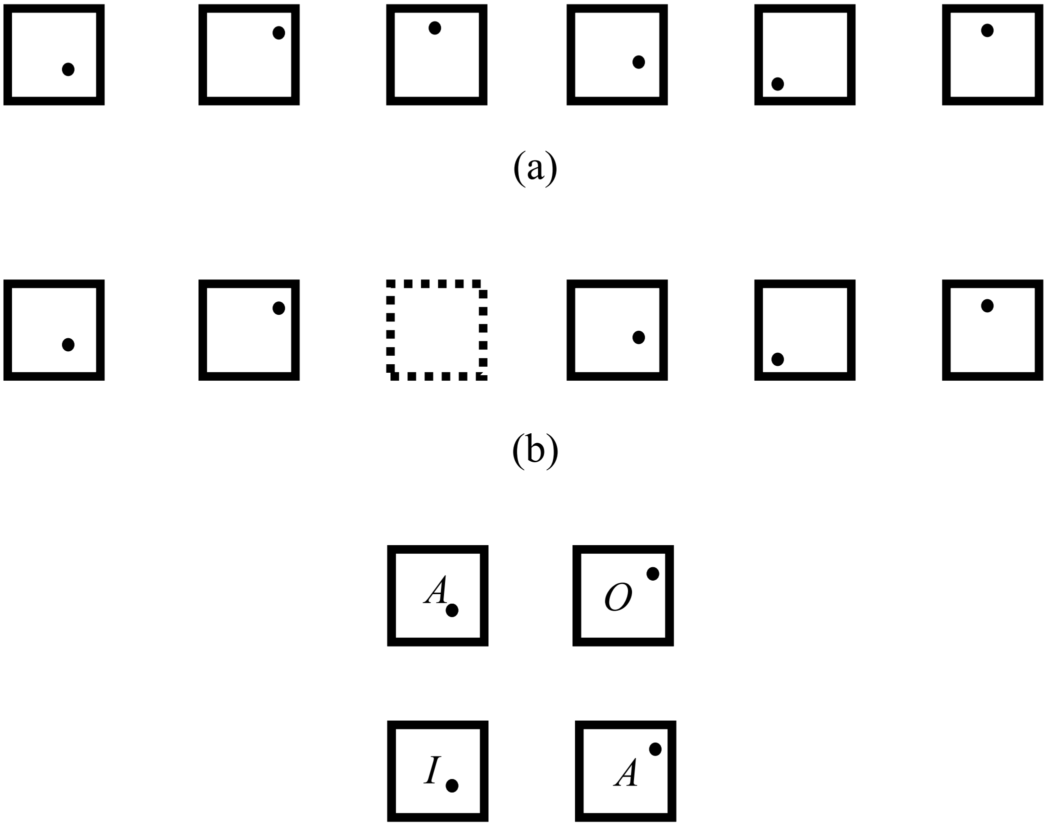

(a)

(b)

(c)

Figure 3.5: A schematic drawing of the setup for a system of (a) a slightly irregular linear lattice (b) a slightly irregular lattice with the third site empty, and (c) a slightly irregular 2×2 square lattice.

hopping of character from one region to next can clearly be seen as the probability of finding the $n = 61$ state in the region next to the leftmost region peaks just after the probability of finding it in the initial region drops off. The hopping is also seen as the $n = 61$ state returns and the dashed line peaks just before the solid line. The probability of finding the $n = 61$ character in the rightmost region peaks around 8 μs which is around the same time scale where the two atom case damps out to the average value. This indicates that the coherence survives the spatial for long time scales. In fact these probabilities continued to oscillate up to approximately 20 μs.

In an experiment it might not be possible to perfectly fill every lattice site. In Fig. 3.6.c we examined the effects of having an atom missing from a region. We simulated the case of 6 regions with only 5 atoms. The configuration was as follows: 61,60, no Rydberg, 60,60,60. See Fig. 3.5.

We looked at the hopping from region to region in the same manner as the previous figure. What immediately pops out is the similarity between Figs. 3.6.a and 3.6.c. This implies the leftmost two regions behave like the two atom case. The probability of jumping the gap in region 3 is very small. Since the dipole-dipole interaction falls off like $1/R^3$, the strength of the interaction between regions 1 and 2 is a factor of 8 times larger than the interaction between regions 2 and 4. The strongest coupling is between the nearest atoms, so much so that the pair of atoms do not interact strongly with the rest of the atoms.

We moved from a linear array of regions to a 2×2 square of regions with one $n = 61$ atom and the rest $n = 60$. It is important to once again mention that the

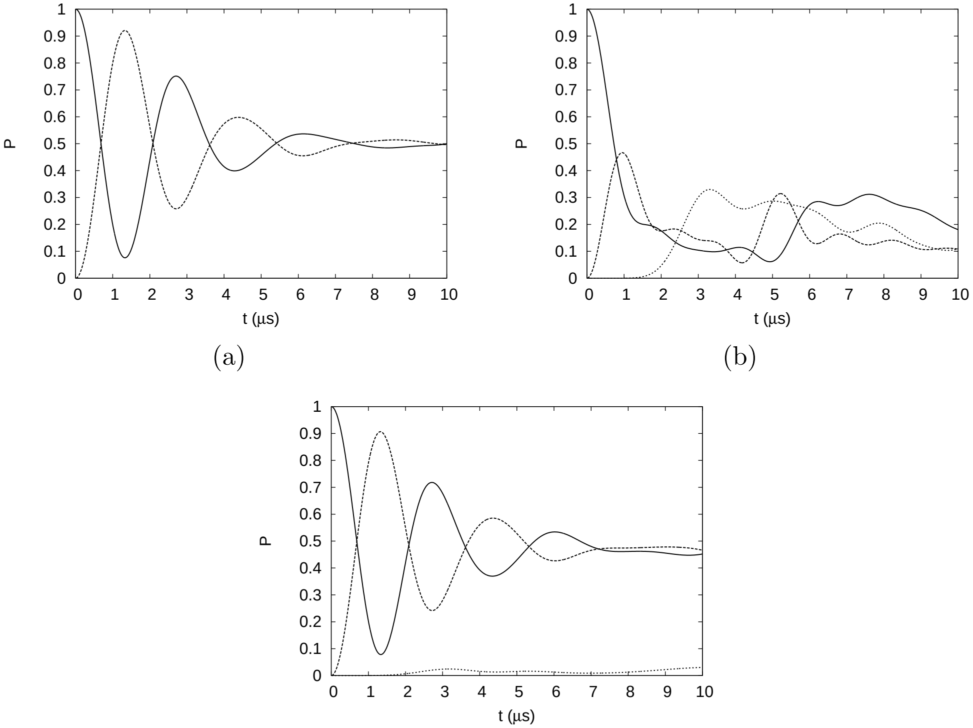

(a) (b)

(c)

Figure 3.6: The probability P for finding the $n = 61$ state on various atoms as a function of time. The atoms are placed in small regions with a width of 3 μm and separated by a center-to-center distance of 20 μm. In all cases the $n = 61$ state in initially in the leftmost region. (a) For two regions, where the solid line is probability of finding the $n = 61$ state in the leftmost region, and the dashed line is the probability of finding it in the rightmost region. (b) For six regions (see Fig. 3.5.a), the solid line is the probability of finding the $n = 61$ state in the leftmost region. The dashed line is the probability of finding it in the adjacent region, and the dotted line is the probability of finding it in the rightmost region. For six regions with an atom missing in third region (see Fig. 3.5.b), the solid line is the probability of finding the $n = 61$ state in the leftmost region. The dashed line is the probability of finding it in the adjacent region, and the dotted line is the probability of finding it in the rightmost region. Note the similarity between (a) and (c) which indicates that the excitations cannot hop over the skipped region.

electric field is perpendicular to the plane of the array $\hat{z} \cdot \hat{R} = 0$, which means that there is no angular dependence to the dipole-dipole interaction between Rydbergs. Only the distance between regions will effect the nature of the hopping. We labeled the regions of the square in the following manner: the initial region (I), an adjacent corner (A), and the opposite corner (O). The solid line in Fig. 3.7 is the probability of finding the $n = 61$ state in region I, while the dashed line is the probability of finding it in region A, and the dotted line is the probability of finding the $n = 61$ state in region O. The peaks in the figure suggest the $n = 61$ state seems to hop from region I to A before hopping to region O.

3.5 Conclusions

By implementing an essential states model it is possible to explore the coherent interactions between Rydberg atoms by solving the time-dependent Schrödinger equation. We examined two distinct situations where atoms are excited into Rydberg states between which a resonant exchange of energy is allowed to occur. In the first case there is no electric field, and the energy exchange is between an $|sp\rangle$ state and a $|ps\rangle$ state. The situation where there is one p state in a sea of s states was used to calculate simple band structures. The band structure for a perfect linear array of atoms was remarkably similar to what is seen in the bands for a line of driven nanoparticles. The nature of the excitations near $k \sim 0$ was also labeled as either particle-like or hole-like depending on the curvature. The coherent hopping of excitation was also investigated for a perfect square lattice and a cubic lattice. As the dimensionality

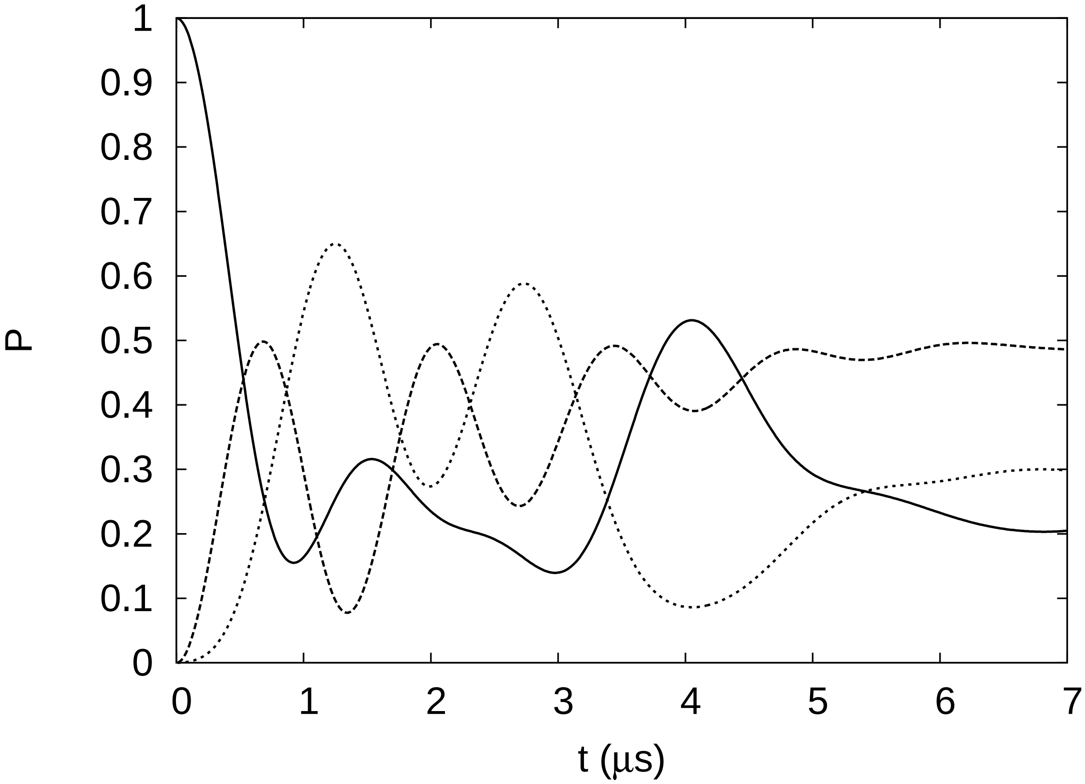

Figure 3.7: The probability of the $n = 61$ state being in a region as a function of time for a slightly irregular 2×2 square lattice (See Fig. 3.5.c). The solid line is the probability of finding the $n = 61$ state in the initial region I, the dashed line is the probability of finding it in an adjacent region A, and the dotted line is the probability of finding it in the opposite corner region O.

of the system increased the richness of the band structure also increased. Now in addition to holes and particles, phonon-like hopping was found.

The second case consisted of Rydberg atoms excited to high Stark states in a static electric-field. The coherent energy transfer of interest then became from $|n_1 n_2\rangle$ to $|n_2 n_1\rangle$ and visa versa. In order to simulate a realistic experimental setup, the atoms were not perfectly placed in a regular arrangement, but rather a nearly perfect one. Even in this non-perfect case, the coherent hopping should last for substantial time scales. If the nonregularity is so severe that there appears to be a hole in the chain of atoms, the hole in the chain will block the excitation from hopping across.

3.6 Validity of the essential state model

The results in this section are based in the work done by F. Robicheaux and T. Topçu in Ref. [26]. In order to investigate the validity of the essential states model the interaction between atoms must be carefully examined, in particular the transitions to states outside of the ones used the essential states model. Since a Rydberg atom can be reasonably modeled as hydrogen-like, the essential states model can be tested by numerically solving the time-dependent Schrödinger equation for two hydrogen atoms.

3.6.1 Field-free case

The potential between two hydrogen atoms can be modeled by

$$V(\vec{r}_1, \vec{r}_2, R) = -\frac{1}{r_1} - \frac{1}{r_2} + \frac{r_1 r_2}{R^3}. \tag{3.16}$$

As the distance, R, between the two atoms is increased to infinity, V effectively becomes the potential for two isolated hydrogen atoms. The size of the isolated atoms can be estimated from the classical turning radius (where $V(r) = E$), $r = 2n^2$. At minimum the distance between atoms should be large enough for no overlap between the electron orbits. Naturally there are two cases, when both atoms start in the same state $n_1 = n_2 = n$ and when they start in different states $n_1 \neq n_2$. The second case can be limited to looking only at the situation where $|n_1 - n_2| = 1$ because of the rapid fall of the dipole matrix elements with respect to $|n_1 - n_2|$. The first case is nondegenerate, while in the second case $n_1 = n$, $n_2 = n + 1$ is degenerate with $n_1 = n + 1$, $n_2 = n$. In either case, the nearest available states differ from the initial state by energies of the order $1/n^4$. Since the relationship between nearby states is the same for either initial state, the simpler nondegenerate case should be sufficient to describe the limitations of the essential states model in the field-free case.

If the essential states model is to be used then the two atoms starting at $n_1 = n_2 = n$ should remain in the states n, n at the end of the simulation time. In other words the probability of finding the atoms in a nearby n', n'' state should be very small. The simulation was performed by including an expansion of basis states $\psi_{n_1}(r_1)\psi_{n_2}(r_2)$

until convergence occurred. The expansion was accomplished by scanning n_1 and n_2 through the states $n - \Delta n$ to $n + \Delta n$, and Δn was increased until the wavefunction converged. The amount of mixing between states is an effect of the last term in the potential V, $r_1 r_2/R^3$, so as R is decreased the transition between states should get stronger.

In their paper the conclusion was that for less than 10% mixing between n-manifolds, the distance between atoms should be greater than $10n^2$ as long as $n < 80$. There also needs to be no accidental degeneracies. Using these findings the essential states model should be accurate for $n = 60$ as long as $R \gtrsim 2\mu$m.

3.6.2 Static electric field

In the presence of a static electric field F pointed in the z direction, the interaction potential can be written

$$V(\vec{r}_1, \vec{r}_2, R) = (z_1 + z_2)F + \frac{\vec{r}_1 \cdot \vec{r}_2 - 3(\vec{r}_1 \cdot \hat{R})(\vec{r}_1 \cdot \hat{R})}{R^3}. \tag{3.17}$$

This potential gives rise to Stark splitting and the transitions within the n-manifold. The Stark splitting can also lead to mixing of states between n-manifolds. This mixing occurs when the field strength is $F \simeq 1/(3n^5)$, so the essential states model will require $F < 1/(3n^5)$.

Since this model is based upon using two H atoms, the problem can be greatly simplified by taking advantage of the scaled Runge-Lenz vectors and rewriting the position operators $\vec{r}_1$ and $\vec{r}_2$ [61],

$$\vec{r}_1 = \frac{3}{2} n_1 \vec{A}_1, \quad \vec{r}_2 = \frac{3}{2} n_2 \vec{A}_2. \tag{3.18}$$

The scaled Runge-Lenz vectors and the orbital momentum operators can now be replaced by a new set of commuting angular momentum operators, $\{\vec{J}_1, \vec{J}_2, \vec{J}_3, \vec{J}_4\}$

$$\begin{aligned} \vec{L}_1 &= \vec{J}_1 + \vec{J}_2, \qquad & \vec{A}_1 &= \vec{J}_1 - \vec{J}_2 \\ \vec{L}_2 &= \vec{J}_3 + \vec{J}_4, \qquad & \vec{A}_2 &= \vec{J}_3 - \vec{J}_4. \end{aligned} \tag{3.19}$$

Equation 3.17 can now be rewritten

$$\begin{aligned} V \;=\; & \frac{3}{2} \left[n_1 (J_{1z} - J_{2z}) + n_2 (J_{3z} - J_{4z}) \right] F + \frac{9 n_1 n_2}{4 R^3} \\ & \times \left\{ (\vec{J}_1 - \vec{J}_2) \cdot (\vec{J}_3 - \vec{J}_4) - 3 \left[(\vec{J}_1 - \vec{J}_2) \cdot \hat{R} \right] \left[(\vec{J}_3 - \vec{J}_3) \cdot \hat{R} \right] \right\}. \end{aligned} \tag{3.20}$$

The magnitude of $\vec{J}_1$ and $\vec{J}_2$ are both $j_1 = j_2 = (n_1 - 1)/2$ while the magnitude of $\vec{J}_3$ and $\vec{J}_4$ are both $j_3 = j_4 = (n_2 - 1)/2$, and the azimuthal component of $\vec{J}$, m, ranges from $-j$ to j.

The mixing between Stark states within an n-manifold is suppressed as the spacing between states is made large compared to the coupling matrix elements. The coupling between states is determined by the separation while the spacing between Stark states is proportional to the strength of the electric-field. When the simulations are run and R is varied, the distance where the state-mixing rapidly changes from strong to weak is the distance where the strength of the dipole electric-field from one atom is comparable to the strength of the external field: $n^2/R^3 \sim F \rightarrow R_{min} \gtrsim n^{2/3}F^{-1/3}$. The size of the minimum separation between atoms can be made smaller by increasing the electric-field, but as mentioned above F cannot be too strong or mixing between manifolds will begin to occur. When just under the largest allowed value for $F \lesssim 1/(3n^5)$ is used $R_{min} \gtrsim n^{7/3}$. For the $n = 60$ case looked at in this chapter, $R_{min} \sim 2\mu$m which is much smaller than the 20 μm distances used.

For either the field-free or the static electric field case, the essential states model is reasonable and quite accurate for the parameters used in this chapter.

Chapter 4

The effects of rotary and spin echo sequences on a Rydberg gas

4.1 Introduction

Advancements in cooling and trapping have opened up new opportunities for investigating the properties of interacting many-body systems. In particular, the creation of frozen Rydberg gases have made it possible to study correlated groups of atoms [8, 9]. At these low temperatures the motion of the atoms can be neglected during the time scales of excitation, and the long range interactions between atoms can be carefully studied.

One interesting consequence of the strong interaction between Rydberg atoms is the suppression of excitation known as the dipole blockade effect [4, 14]. While the reduction in excitation has experimentally been seen by several groups [14–19, 50], it is of recent interest to measure the coherent collective behavior of the groups of atoms that have been blocked from becoming excited [36, 50].

The dipole-dipole interaction between Rydberg atoms can also lead to a situation where two pairs of states ($|AB\rangle, |B'A'\rangle$) are moved into resonance with each other ($E_A + E_B \simeq E'_B + E'_A$) [8, 9, 31, 52]. In this case, the system will oscillate between the two states at a rate governed by the dipole-dipole interaction between them. With more than two atoms involved in the system, the states appear to coherently hop from atom to atom [26, 30]. If the atoms are placed into regular lattice sites then a direct observation of the coherent hopping can be detected [30], but in a random gas the coherent nature of the hopping is hidden.

In this chapter we simulated the effect of echo sequences on coherent Rydberg systems by using the many-body pseudoparticle wavefunction approach outlined in chapter 2 and the essential states model used in chapter 3 to numerically solve the Schrödinger equation. In particular we investigated the rotary echo of a strongly blocked Rydberg gas and the spin echo of a system of hopping excitations. The approach taken in section 2.7 is particularly appropriate to use in the strong dipole blockade regime because we explicitly correlate groups of nearby atoms and take into account the spatial correlations between pseudoparticles that a simple mean field model can not. The hopping dynamics are well described by the essential states model.

4.2 Rotary echo of a dense Rydberg gas

When the system is especially dense, the correlations within a gas can become the dominant factor in the dynamics of the system. An example of this is the coherent Rydberg excitation of dense ultracold atoms [50]. In this case, the van der Walls interaction ($V(R) \propto 1/R^6$) between excited states actively suppressed the number of atoms able to be excited to Rydberg states, exhibiting a dipole blockade [4]. In section 2.4.1 we simulated a dipole blockade, and generated 2D correlation functions which indicated that there was a minimum allowed distance between excitations called the blockade radius R_b. Only one excited atom within the blockade region was allowed, and the single excitation was de-localized across all N_b atoms contained within this volume. The collective Rabi oscillation rate Ω of this collection, or “superatom” [35], of N_b atoms was given by $\Omega = \sqrt{N_b}\Omega_0$ where Ω_0 was the Rabi frequency of an isolated atom. The results of section 2.7.1 showed that the size of the blockade region was related to the density of the atoms within the region: $R_b \propto \rho^{-1/15}$, and ultimately the collective oscillation rate of a superatom was dependent on the local density by $\Omega \propto \rho^{2/5}$. In a typical MOT, the density of the gas spans over several orders of magnitude; therefore superatoms within the gas will oscillate over a wide range of frequencies. In fact, by using the MOT parameters in Ref. [50], we discovered in section 2.7.1 that most of the superatoms in the gas oscillate about ten times slower than those located near the peak density. This inhomogeneity in density (and therefore collective oscillation frequency) makes it very difficult for experimental studies to directly measure the coherent nature of the system because the observable is an integration over the entire sample [36].

Early studies in the field of nuclear magnetic resonance physics had to overcome similar problems with inhomogeneities in magnetic fields which led to a wide range of Larmor precession frequencies and obscured the resonant absorption of the driving RF field [37,38]. In 1950, Hahn demonstrated the effectiveness of a “spin echo” sequence of pulses that was extremely effective in eliminating noise from the signal. In 1959 Solomon also demonstrated the successful use of a “rotary echo” in doped water to overcome the effects of inhomogeneities in magnetic fields.

More recently, there was an experiment which used a rotary echo technique to prove the coherence of the excitation in a strongly blockaded ultracold gas [36]. The experimental setup in Ref. [36] trapped and cooled atoms down to 3.8 μK and excited them to $43S_{3/2}$ for up to 500 ns while keeping track of the total number of excitations in the gas. At such a low temperature and short excitation time the atoms are effectively motionless, so thermal motion can be disregarded as an outside source of decoherence. In a system of ultracold Rydberg atoms, a substantial source of inhomogeneity in the Hamiltonian is the variation in local density across the sample; the Gaussian shape of the density distribution in Ref. [36] certainly led to an inhomogeneity in Ω.

4.2.1 Rotary echo

In simplest terms a rotary echo sequence flips the sign of the excitation amplitude in the Hamiltonian after a certain time τ_p. The Hamiltonian describing the excitation of a dense ultracold gas using the pseudoparticle approach was given in section 2.3:

$$\begin{aligned} \hat{H}(t) &= \sum_j \hat{H}_j^{(1)}(t) + \sum_{j<k} V_{jk} |n_j n_k\rangle\langle n_j n_k| \\ \hat{H}_j^{(1)}(t) &= -\left(\Delta\omega(t) + \varepsilon(t)\right)|n_j\rangle\langle n_j| + \mathcal{F}(t)\frac{\Omega_0}{2}\sqrt{W_j}(|g_j\rangle\langle n_j| + |n_j\rangle\langle g_j|), \end{aligned} \tag{4.1}$$

where V_{jk} is the interaction between two pseudoparticles j and k. The number of atoms associated with each pseudoparticle is given by W. The detuning of the laser is $\Delta\omega(t)$, and $\varepsilon(t)$ is a mean field energy shift due to excited atoms outside of the simulated volume. The kets $|g_j\rangle$ and $|n_j\rangle$ correspond to atom j being in the ground state and excited to the n manifold respectively, and $|n_j n_k\rangle$ is the state where atoms j and k are both excited. In Ref. [36], the rotary echo sequence was accomplished by using an RF field to flip the sign of Ω_0 after the time $\tau_p \leq \tau$, where τ is the total excitation time. In our simulations we used the following to model the excitation profile:

$$\mathcal{F}(t) = \begin{cases} e^{-5(t-t_r)^2/t_r^2} & \text{for } t \leq t_r \\ 1 & \text{for } t_r < t \leq \tau_p - t_r \\ e^{-2(t-(\tau_p-t_r))^2/t_r^2} - e^{-2(t-(\tau_p+t_r))^2/t_r^2} & \text{for } \tau_p - t_r < t \leq \tau_p + t_r \\ -1 & \text{for } \tau_p + t_r < t \leq \tau - t_r \\ -e^{-5(t-(\tau-t_r))^2/t_r^2} & \text{for } \tau - t_r < t \leq \tau. \end{cases} \tag{4.2}$$

In Eq. 4.2, t_r is the ramping time for the laser. A Gaussian is used during ramp on time, between sign changes, and ramp down time as a smooth transition to avoid an instantaneous switch which could lead to unphysical, and therefore undesired high frequency effects. Figure 4.1 illustrates an example of this type sequence.

When the system is sufficiently sparse, the energy shift due to the van der Waals interaction (V_{jk}) between atoms becomes negligibly small compared to the width of the excitation amplitude, and the ground state atoms are excited for a time τ_p and de-excited for a time $\tau - \tau_p$. This system of isolated atoms will be returned to zero excitations if $\tau_p = \tau/2$. A measurement of zero excitations is the perfect rotary echo

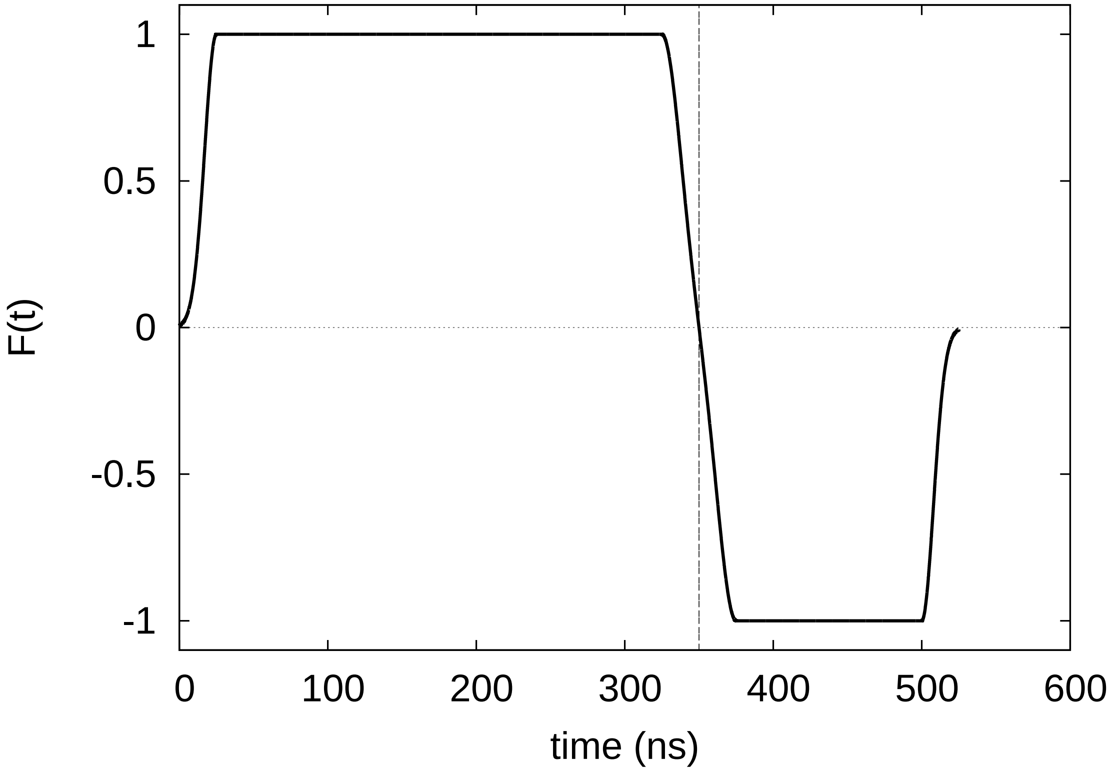

Figure 4.1: An illustration of a rotary echo sequence. The sign of the excitation amplitude $\mathcal{F}$ is smoothly flipped after time τ_p. In this case $\tau_p = 350$ ns, and is indicated by the dashed line.

case. Figure 4.2 is the result of simulating the excitation of a diffuse system of 5 atoms using a rotary echo sequence. The excitation amplitude Ω_0 was chosen so the maximum number would be excited at 500 ns. These echo simulations compare the number of excited atoms to the timing of the sign flip τ_p. As expected, when $\tau_p = \tau/2$ a perfect echo was recorded.

If the system is so dense that the vdW interactions are much greater than the excitation amplitude then the system is in the strong blockade limit. In the extreme case where all of the atoms are within a blockade radius the system has been reduced down to a single superatom. This single isolated superatom will also be excited and de-excited for the same amount of time, thus returning the system to a state of zero excitations. In Figure 4.3, we plot the number excited versus τ_p for a perfectly blocked system of 10 atoms. A perfect echo can be seen when $\tau_p = \tau/2$ and the maximum number excited is exactly 1.

A more interesting situation arises when the system is dense enough to create blockades, yet large numbers of excitations are allowed to occur. Now the energy shift due to the van der Waals interaction is comparable to the width of the excitation amplitude. In this case the pseudoparticle approach used in section 2.7 is especially useful in describing the spatial correlations between pseudoparticles which represent groups of blockaded atoms. In this model, the van der Waals interaction is between pseudoparticles and not between individual atoms themselves, so the inhomogeneity in collective oscillations is explicitly included in the simulation. We simulated a rotary echo sequence of excitation for two different peak densities. In each case we simulated

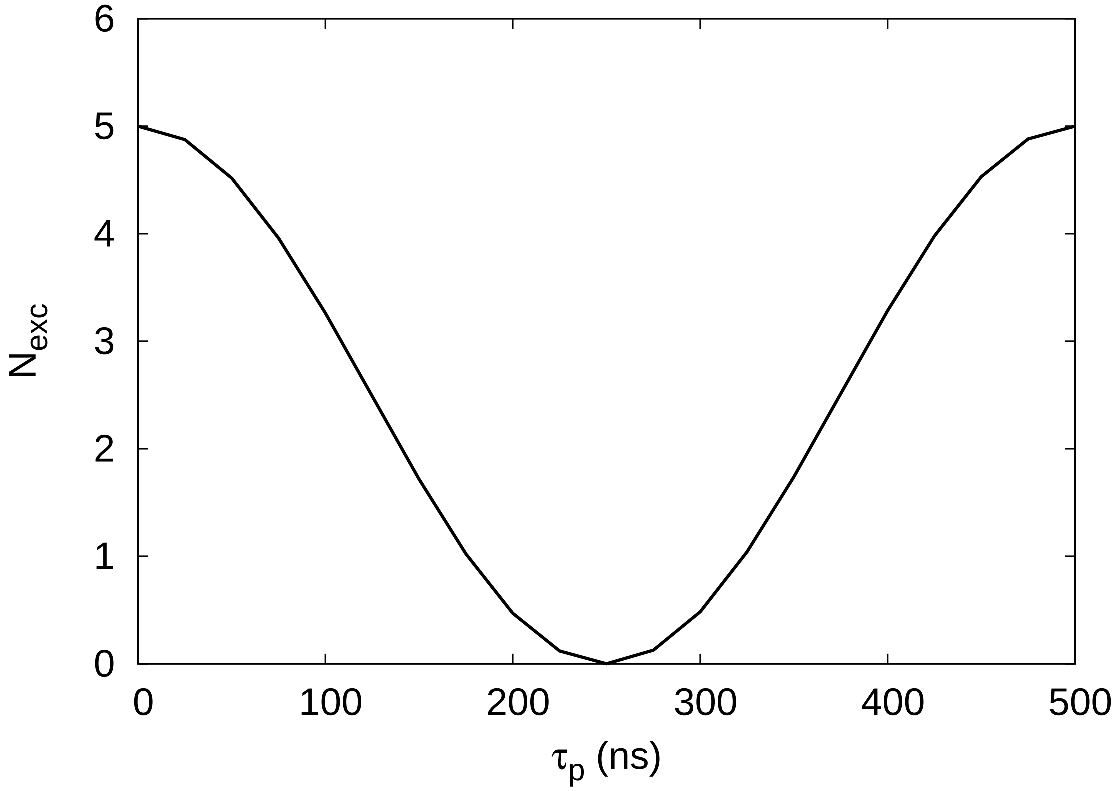

Figure 4.2: Number excited versus the timing of the sign change of the excitation amplitude. This echo signal is for 5 isolated atoms. Note that there are zero excitations when $\tau_p = 250$ ns, exactly half of the total excitation time.

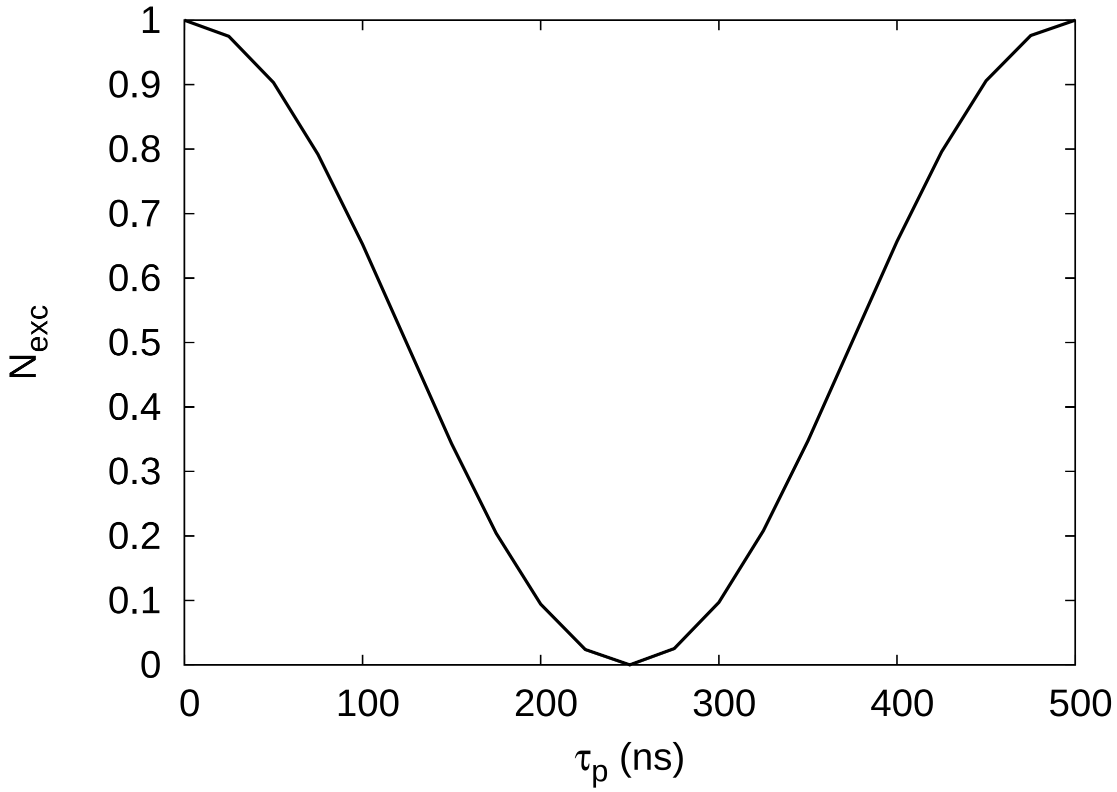

Figure 4.3: Number excited versus the timing of the sign change of the excitation amplitude. This echo signal is for 10 atoms in the perfect blockade regime. Note the perfect echo signal at 250 ns.

the fraction excited at specific density points as we did in section 2.7.2 and convolved the results over the density distribution given in [50]. The other parameters used in the following three simulations were chosen to match those used in Ref. [36]. Plotted in Figure 4.4.a is the echo signal as a function of τ_p for a peak density of 5×10^{12} cm^{-3}. While the echo signal is not perfect at $\tau_p = \tau/2$, it is still prevalent because the interaction between pseudoparticles is not as strong. When simulating at a higher peak density of 1.5×10^{12} cm^{-3}, the echo signal is weakened as in Figure 4.4.b by the dephasing caused by pseudoparticle interactions.

Interactions between pseudoparticles are a significant source of dephasing which prevents a perfect echo from occurring. This can be understood in the context of the Hamiltonian for the system. While the off-diagonal elements (given by the excitation amplitude) are reversed after τ_p, the sign of the diagonal van der Waals interaction elements remain unchanged, and the system does not perfectly evolve backwards in time. If it were possible to switch the sign of the van der Waals interaction between particles at the same time as the excitation amplitude then the sign of the entire Hamiltonian would be flipped and all sources of dephasing would have to be external such as thermal motion or ionization. Flipping the sign of the whole Hamiltonian is effectively the same as reversing the sign of t and perfectly running the system backwards in time. The lack of a perfect rotary echo signal would indicate outside sources of decoherence on the gas and coupling to external degrees of freedom. In Fig. 4.5 we simulated a system where the whole Hamiltonian gets switched in sign at τ_p in the same manner as Eq. 4.2. The perfect echo indicated in our simulations is

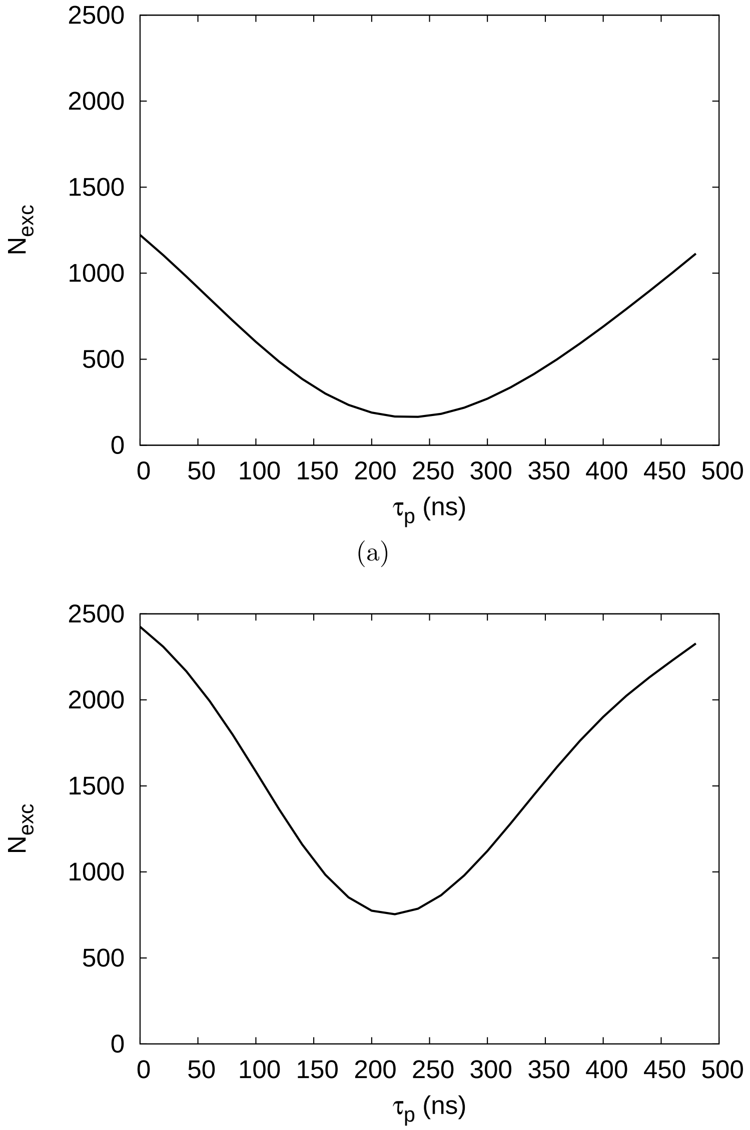

(a)

(b)

Figure 4.4: Number excited versus the timing of the sign change of the excitation amplitude. The echo signal for (a) peak density of $\rho = 5.0 \times 10^{12}$ cm^{-}3 and (b) peak density $\rho = 1.5 \times 10^{13}$ cm^{-}3.

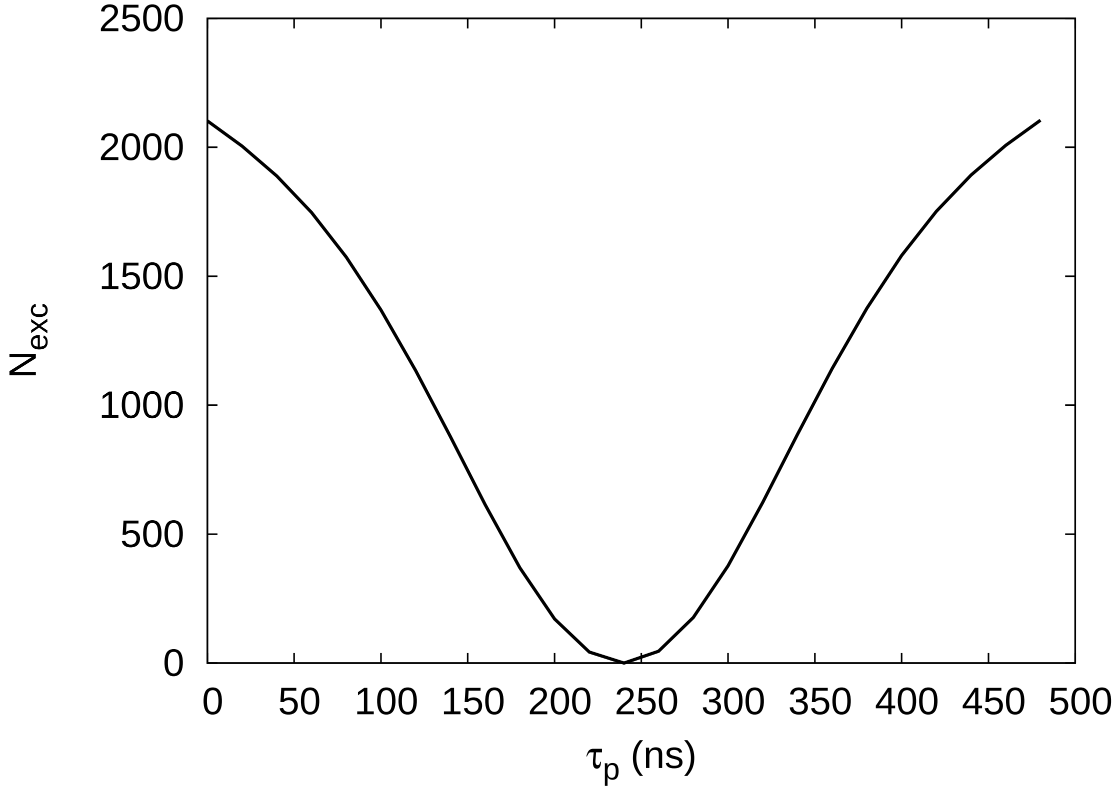

Figure 4.5: Number excited versus the timing of the sign change of the entire interaction Hamiltonian. This echo signal is for a high peak density of $\rho = 1.5 \times 10^{13}$ cm^{-}3.

consistent with the notion of running the system backwards in time. We believe that it might be possible to realize a time-reversable system of Rydberg atoms by using a small electric field to diabatically push the system to states that experience a dipole interaction of the same magnitude but opposite in sign compared to the field-free states. A promising interaction would involve taking advantage of the resonance near $n = 43$ for $d - d$ Rb atoms.

4.3 Spin echo for Rydberg hoppers

In section 3.4, a possible experiment to measure the coherent hopping of excitation between slightly irregular lattice sites was proposed. A key feature of this proposed experiment was the clear separation of regions which would allow for the spatial location of the hopper to be measured, but it would be impossible to measure the coherent nature of the hopping in an inhomogeneous gas in this manner. The amount of time it takes for an excitation to hop between atoms is inversely proportional to the dipole-dipole interaction energy between them, $t_{hop} \propto R^3$ [26], so in an irregular gas of Rydberg atoms the excitations would be hopping at different rates and directions. Any measurement of hopping rates or locations would be hidden due to the random placement of Rydberg atoms.

4.3.1 Spin echo

Like the rotary echo, the spin echo sequence was first used to overcome inhomogeneities in the magnetic field in NMR. Unlike the rotary echo, the spin echo isn't simply a consequence of running the system forwards and backwards in time for the same duration. The spin echo works by making series of unitary transformations on the generalized Bloch sphere describing the quantum system [37]. In particular we used the following sequence of pulses to simulate a spin echo: first the system is excited by a $\pi/2$ pulse (which takes the ground state $|g\rangle$ to a mix of the ground and excited state $(|g\rangle - i|n\rangle)/\sqrt{2}$, and an excited state $|n\rangle$ to a mix of $|n\rangle \rightarrow (-i|g\rangle + |n\rangle)/\sqrt{2}$), then the system is allowed to relax for a time τ_1. Next, the system is excited by a π pulse (which takes the state $|g\rangle \rightarrow -i|n\rangle$ and $|n\rangle \rightarrow -i|g\rangle$); again the system is allowed to relax for τ_2, and finally the system is excited via a $\pi/2$ pulse. In summary the sequence looks as follows:

$$\pi/2 \rightarrow \tau_1 \rightarrow \pi \rightarrow \tau_2 \rightarrow \pi/2. \tag{4.3}$$

If sources of dephasing and outside decoherence are negligible then the system will exhibit a strong spin echo when the two relaxation times are equal $\tau_1 = \tau_2$.

We simulated the effect of the spin echo sequence of Eq. 4.3 on the following system: a single ground state $|g\rangle$ atom in a sea of atoms excited to the Stark state $|n'\rangle$ or $|\psi_0\rangle = |gn'n' \cdots n'\rangle$. This is, of course, a severe approximation to a real experiment where the number of $|g\rangle$ state atoms will most certainly be greater than one, but the effect of a spin echo sequence on this simplified system should be of interest. The density of the gas was chosen so the average distance between particles would be 13.5 μm. The excitation laser coupled $|g\rangle$ to an excited Stark state $|n\rangle$, but not $|g\rangle$ to $|n'\rangle$. The two Rydberg states $|n\rangle$ and $|n'\rangle$ were chosen in a manner that allowed for the resonant exchange of energy through the dipole-dipole interaction [26]. This means that the $|n\rangle$ state on atom j can coherently hop to any atom k with $|n'\rangle$ character. If the direction of the static electric field is in the $\hat{z}$ direction then the likelihood of hopping will be determined by $(nn'/3)^2/R_{jk}^3$, where $|n - n'| = 1$ are the principal quantum numbers of the two Stark states, and R_{jk} is the distance between the two atoms. If the atoms are not allowed to move during the simulation time (i.e. the temperature is set to 0 K), then the final state of the system after a spin echo sequence can be analytically derived for the single hopper case in a sea of N $|n'\rangle$ atoms. For clarity, we first solved the two particle case for the final state of the system:

$$\begin{aligned}
|\psi_f\rangle = \frac{1}{2}\Big\{ &- \ \left[\cos(V\tau_2)e^{-i(\varepsilon_g\tau_1+\varepsilon_n\tau_2)} + \cos(V\tau_1)e^{-i(\varepsilon_g\tau_2+\varepsilon_n\tau_1)}\right]|gn'\rangle + \\
&+ i\left[\sin(V\tau_2)e^{-i(\varepsilon_g\tau_1+\varepsilon_n\tau_2)} + \sin(V\tau_1)e^{-i(\varepsilon_g\tau_2+\varepsilon_n\tau_1)}\right]|n'g\rangle + \\
&- i\left[\cos(V\tau_2)e^{-i(\varepsilon_g\tau_1+\varepsilon_n\tau_2)} - \cos(V\tau_1)e^{-i(\varepsilon_g\tau_2+\varepsilon_n\tau_1)}\right]|nn'\rangle + \\
&+ \ \left[\sin(V\tau_2)e^{-i(\varepsilon_g\tau_1+\varepsilon_n\tau_2)} - \sin(V\tau_1)e^{-i(\varepsilon_g\tau_2+\varepsilon_n\tau_1)}\right]|n'n\rangle \\
\Big\} &\times e^{-i\varepsilon_{n'}(\tau_1+\tau_2)},
\end{aligned} \tag{4.4}$$

where $V = (nn'/3)^2/R_{jk}^3$ was the off-diagonal matrix element for the dipole-dipole interaction, ε_g was the energy of the ground state, ε_n, and $\varepsilon_{n'}$ were the energies of the excited Stark states. When $\tau_1 = \tau_2 = \tau$, the final wavefunction is simply

$$|\psi_f\rangle = [-\cos(V\tau)|gn'\rangle + i\sin(V\tau)|n'g\rangle]\, e^{-i(\varepsilon_g+\varepsilon_n+2\varepsilon_{n'})\tau}. \tag{4.5}$$

Note that only $|gn'\rangle$ and $|n'g\rangle$ states remained, and the probability of finding an atom in the Stark state $|n\rangle$ is zero. This was a perfect spin echo. For the case of a small difference in relaxation times, $\tau_2 = \tau_1 + \Delta$ and Δ is small, this case can be simplified as well to

$$\begin{aligned} |\psi_f\rangle = -\Big\{ & \cos([\varepsilon_n - \varepsilon_g]\,\frac{\Delta}{2})\,[\cos(V\tau_1)|gn'\rangle - i\sin(V\tau_1)|n'g\rangle] \\ & - \sin([\varepsilon_n - \varepsilon_g]\,\frac{\Delta}{2})\,[\cos(V\tau_1)|nn'\rangle - i\sin(V\tau_1)|n'n\rangle] \Big\} \\ & \times e^{-i(\varepsilon_g+\varepsilon_n+2\varepsilon_{n'})(\tau_1+\frac{\Delta}{2})}. \end{aligned} \tag{4.6}$$

Now the probability of finding a $|n\rangle$ state atom is very small and proportional to $\left[(\varepsilon_n - \varepsilon_g)\frac{\Delta}{2}\right]^2$. For the general case of one $|n\rangle$ hopper in a sea of N $|n'\rangle$, the final wavefunction is

$$\begin{aligned} |\psi_f\rangle = -\frac{1}{2}\Big\{ & i\sum_{k=1}^{N+1}\left[\alpha_{ik}(\tau_2)e^{-i(\varepsilon_g\tau_1+\varepsilon_n\tau_2)} - \alpha_{ik}(\tau_2)e^{-i(\varepsilon_g\tau_2+\varepsilon_n\tau_1)}\right]|n_k\rangle \\ & \sum_{k=1}^{N+1}\left[\alpha_{ik}(\tau_2)e^{-i(\varepsilon_g\tau_1+\varepsilon_n\tau_2)} + \alpha_{ik}(\tau_2)e^{-i(\varepsilon_g\tau_2+\varepsilon_n\tau_1)}\right]|g_k\rangle \Big\} \\ & \times e^{-iN\varepsilon_{n'}(\tau_1+\tau_2)}, \end{aligned} \tag{4.7}$$

where α_{ik} is the probability amplitude of finding the $|n\rangle$ state initially on atom i on atom k, $|g_k\rangle$ represents the state with $|g\rangle$ atom k, and $|n_k\rangle$ represents the state with $|n\rangle$ on atom k. By solving for the eigenvalues and eigenvectors of the Hamiltonian given in Equations 3.9 and 3.10, we found the values for the hopping amplitudes α. When $\tau_1 = \tau_2 = \tau$, the probability of finding a $|n\rangle$ state atom is zero, and the system again displays a perfect echo:

$$|\psi_f\rangle = -\sum_{k=1}^{N+1} \alpha_{ik}(\tau) e^{-i[\varepsilon_g + \varepsilon_n + 2N\varepsilon_{n'}]\tau} |g_k\rangle. \tag{4.8}$$

In Figure 4.6 we plot the probability of finding no $|n\rangle$ atoms as function of the difference in scaled relaxation time. The difference in scaled relaxation time is $\Delta\tau/t_{hop}$, where $\Delta\tau = \tau_1 - \tau_2$ and $t_{hop} = 0.83\ \mu$s is the time it takes for the excitation to hop the average distance between atoms: 13.5 μm. As expected, in a zero temperature gas with one hopper the system exhibits a perfect echo at $\Delta\tau/t_{hop} = 0$. When the difference in relaxation times becomes large, the system becomes more and more evenly mixed.

While the previous discussion neglected the effects of temperature, by allowing the particles to exhibit thermal motion and by solving for the hopping amplitudes during every time step, we simulated a one hopper gas with an outside source of decoherence. In order to account for the time dependence of the Hamiltonian we used an exponential propagator and adjusted the position of each atom during each time step. If the time steps are kept small and the change in position is also small then

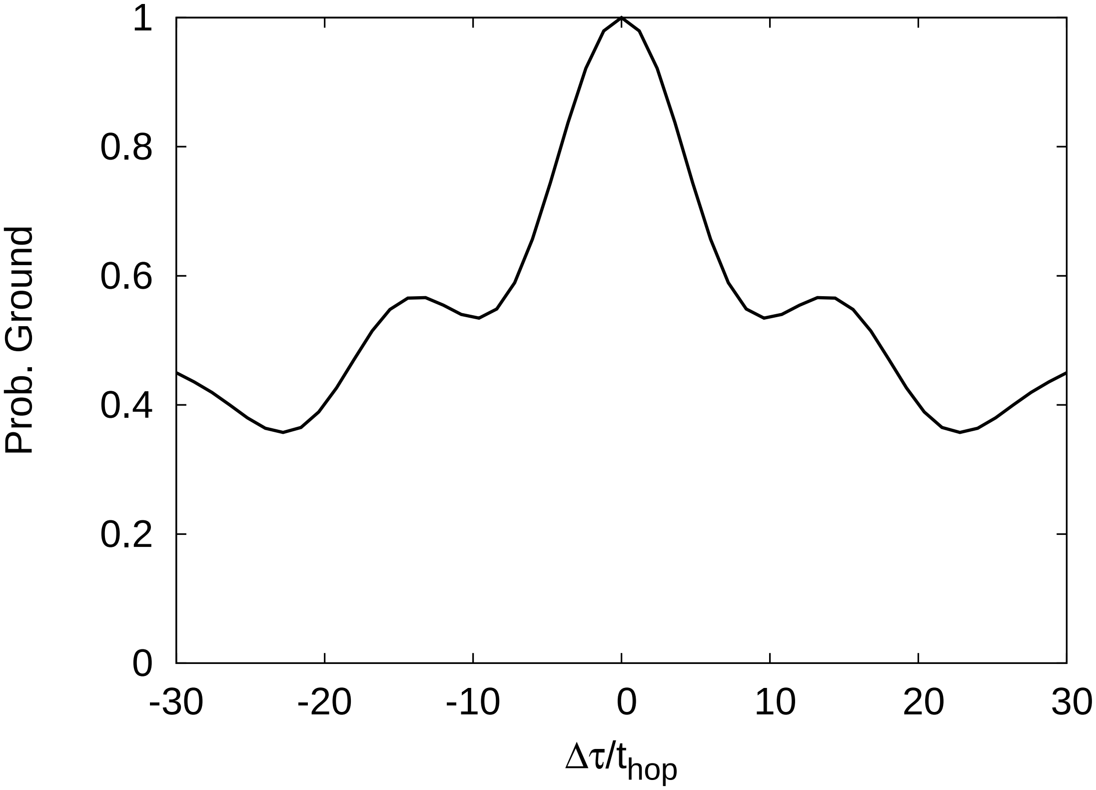

Figure 4.6: Spin Echo signal in a 0K gas with exactly one hopper versus difference in scaled relaxation times. When $\Delta\tau/t_{hop} = 0$ a prefect signal is seen.

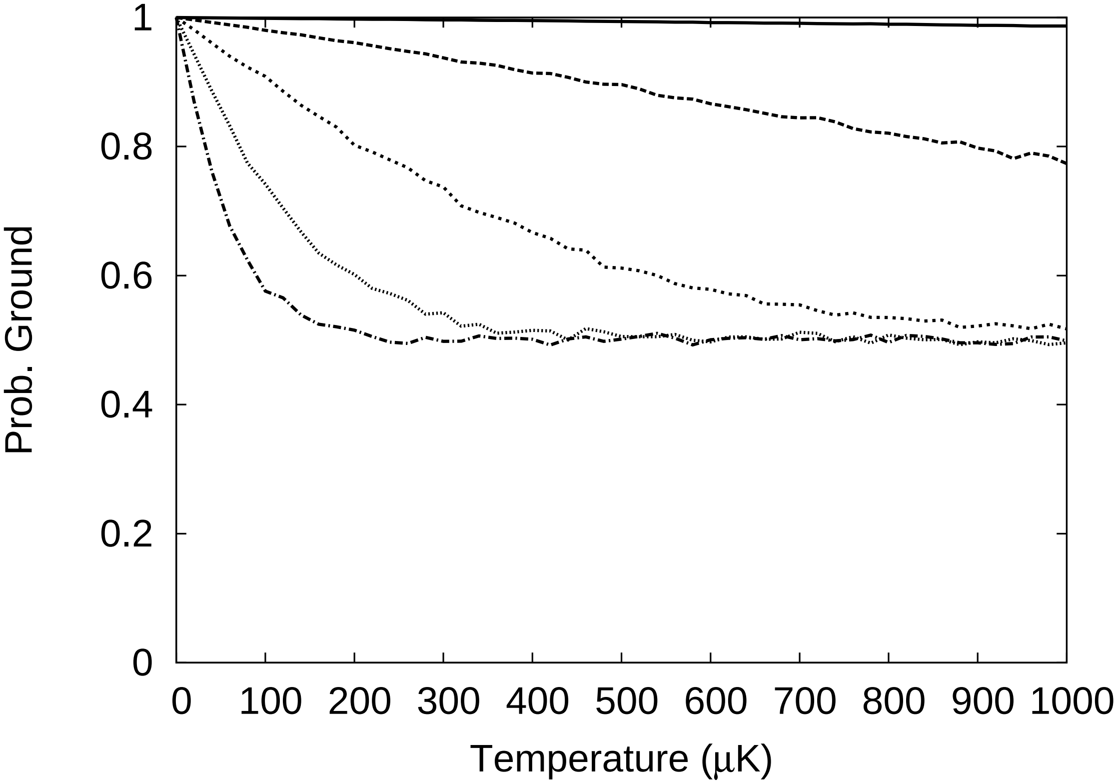

Figure 4.7: Spin Echo signal in a gas with exactly one hopper as a function of temperature for various τ relaxation times. In each case $\tau_1 = \tau_2 = \tau$. The solid line is for a $\tau = t_{hop}$, the dashed line is for $\tau = 2t_{hop}$, the dotted line is for $\tau = 3t_{hop}$, the perforated line is for $\tau = 4t_{hop}$, and the chain line is for $\tau = 5t_{hop}$.

the accumulated errors can be kept to a minimum. The results of our simulations are shown in Fig. 4.7 as a plot of of finding zero $|n\rangle$ atoms as a function of temperature. At every temperature point the two relaxation times were exactly equal, so if thermal motion caused no decoherence then a perfect echo should be seen. If the two relaxation times between excitation pulses are just long enough to allow one hop to occur than the effect of temperature is minimal, the $|n\rangle$ state has not diffused very much. In this situation, the hopping of the $|n\rangle$ state can be limited to only the nearest neighbors;

the sequence of hops to get to the final state is very simple, directly from i to k. When the relaxation time is increased to allow two hops, the effect of temperature is again pretty minimal well into the 100s of microkelvins. Now the $|n\rangle$ state is limited to nearest and next-nearest neighbors and the number of possible particles it can hop to has increased by a factor of about 8, and for each one of these atoms their motion contributes to the dephasing. By increasing the relaxation time, the number of atoms involved in the hopping dynamics increases drastically for each interval of t_{hop}. The effect of temperature is quite apparent when the number of allowed hops is 4 or above, the echo signal has effectively vanished for temperatures greater than 300 μK. As expected when the temperature gets closer to 0 K, a strong echo signal is observed, no matter how many times the excitation is allowed to hop. It should be noted that the even when the thermal motion is neglected, the dipolar force between Rydberg atoms will cause acceleration. The large mass of Rb and the shortness of t_{hop}, however, prevent this motion from being significant. For example, after 10 hops ($\sim$ 8.3 μs) the attractive force between two atoms initially separated by 13.5 μm will have moved them only 0.01 μm closer.

4.4 Conclusions

In summary, we have been able to investigate the effects of echo sequences on systems of interacting Rydberg atoms. We simulated a rotary echo signal in a dense ultracold Rydberg gas by using the pseudoparticle many-body wavefunction approach used in chapter 2 to describe the blockade effect. Unlike simpler mean field models, the pseudoparticle approach directly takes into account high correlation between nearby atoms, and the spatial correlations between pseudoparticles. While a mean field model predicts the strong echo signal to be suppressed due to the strong interactions between nearby pairs of individual atoms, the pseudoparticle method prevents such short distances between Rydberg atoms. Our simulations showed a clear rotary echo signal when the sign of excitation amplitude is switched half-way through the total excitation pulse. When all of the atoms or pseudoparticles are perfectly correlated, a perfect echo is seen. As the density between Rydberg atoms is increased the interactions between pseudoparticles is increased and the echo signal is reduced.

We also simulated a system where the sign of the entire interaction Hamiltonian is flipped, both the laser-atom interaction and the atom-atom interaction. Because the coupling between Rydberg atoms is no longer a source of dephasing, any reduction of the rotary echo signal would indicate an external source of decoherence. It might be possible to experimentally realize such a system using a weak electric field to switch the sign of van der Waals potential between two $44d_{5/2}$ Rb atoms at the same time an RF field is used to switch the phase of the excitation amplitude.

We finally examined the spin echo signal of a single coherently hopping Rydberg excitation in a gas. If thermal motion is neglected, we analytically showed that the system will display a perfect echo when the relaxation time between excitation pulses is exactly equal. Our simulations of temperature dependence on signal strength indicated that as the number of allowed hops in increased, the effect of thermal motion becomes drastically more significant. If more than 4 hops are allowed during each relaxation time then the the temperature of the gas must be less than 300 μK for any discernable echo signal to be detected. Of interest of would be further studies into the effects of multiple hoppers on the spin echo signal, and the how the coherence of these systems respond to increasing temperatures.

Chapter 5

Interactions between classical dipole moments: nanospheres

5.1 Introduction

The interactions between many Rydberg atoms have many similarities with the interactions between nanoparticles [62]. Using our knowledge of the dipole-dipole interactions between Rydberg atoms gained in the previous chapters, we describe the dipole-dipole interactions between driven metallic nanospheres. There have been many theoretical and experimental studies probing the nature of a collection of optically driven metal nanospheres (MNS's), their interactions, and various possible uses as sub-wavelength optical devices [44, 46–49, 62–69]. Arrangements of MNS's with features smaller than the wavelength of light, λ, can be constructed and will interact strongly with light tuned to the surface plasmon (SP) frequency (ω_{SP}) [40]. The coupling of the MNS's through the electromagnetic field produces a coherent wave of oscillating dipole moments. This coupling allows information to pass through geometries smaller than λ and causes the direction of the scattered light to strongly depend on λ.

A simple and important geometry to study is a straight line or chain of equally spaced MNS's placed in a dielectric medium. This configuration is shown in Fig. 5.1 with a realistic particle size and spacing. In this chapter we will use an array of ten nanospheres; it has been shown when using common parameters the infinite chain

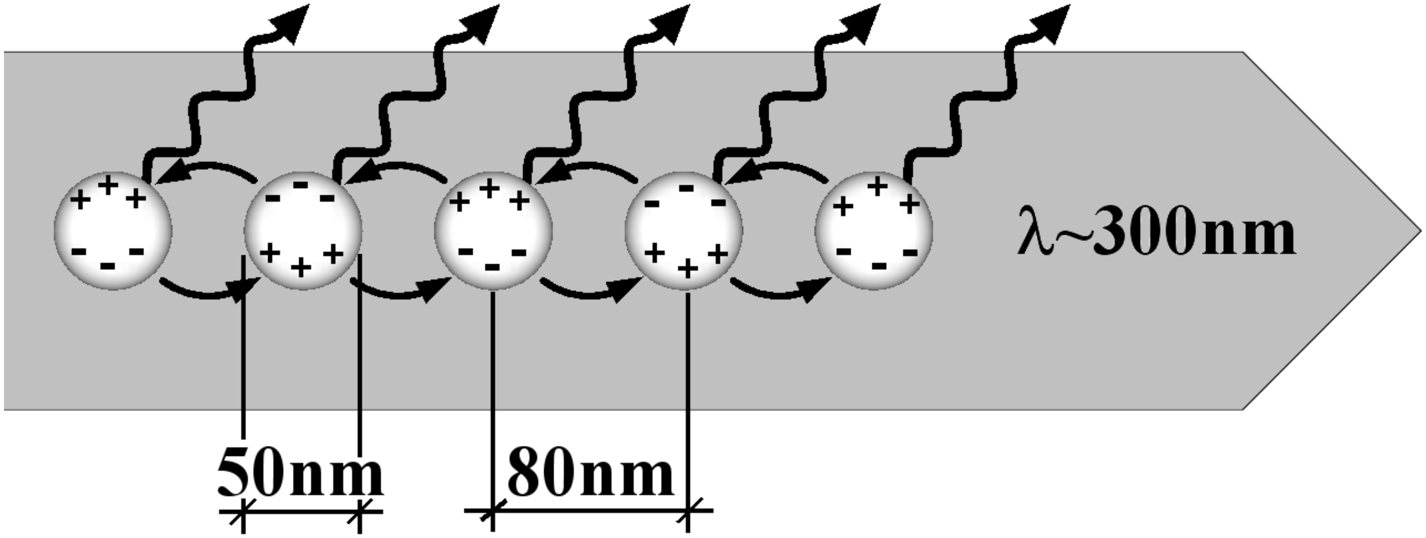

Figure 5.1: A schematic drawing of a possible set up for a regularly spaced linear array of silver nanospheres. A wide (compared to the size of a nanosphere of radius a) beam of light of frequency ω is propagated along the array's axis in the particular medium where the array is assembled. The light absorbed and scattered by each MNS will in turn excite neighboring MNS's and a coherent wave of oscillating electric dipoles will be produced.

limit is met at around ten particles. [67]. A technique for the fabrication of such assemblies is electron-beam lithography, which allows for good control over particle size and regular placement [62]. Since this is one of the simplest configurations to set up experimentally and theoretically, it has been studied extensively. All of the MNS's in the linear array can be excited using a broad light beam at a specific frequency ω.

Theoretical analysis of a linear array of MNS's has been done by several different groups. The numerical methods developed to describe these arrays and their interactions with an external electric field include the discrete dipole approximation [47], the multiple multi-pole method [48], the finite difference time domain method [62], and the T-matrix method [49]. The method used in this chapter can perhaps best be described as the coupled dipole approximation. Each nanosphere will be described by a single point dipole that linearly responds to electric fields. When the system is driven at a specific frequency, ω, then every time dependent quantity can be written as $A(t) = A(0)\ \exp(-i\omega t)$. We will solve a set of self-consistent linear equations describing the response of each electric dipole to the incident field and to the scattered electric fields from the other particles. In doing so we will use the full electric field from the oscillating dipoles and contrast these results with using only the near field approximation.

We report several interesting effects apparent in this simple system that emerge from treating the full field rather than the near field. We show that the ohmic power deposited in a particular MNS can strongly depend on the position in the line of particles even when all of the MNS are equally illuminated by a light beam.

Furthermore, we can reverse the ratio of power in the first sphere compared to the last sphere with an extremely small variation in light frequency suggesting a device for wavelength discrimination over this range of frequencies. Also, we will show that the direction of the light emitted from the MNS array strongly depends on frequency when only one of the spheres is driven. Thus, it should be possible to detect collective properties of the MNS array, like inhomogeneous power distribution along the array, using simple measurements of the far field radiation which could simplify experiments.

There are three uncoupled modes of propagation down this chain: two degenerate transverse (T) waves which have the direction of the dipole moments, $\vec{p}$, perpendicular to the line of MNS's, and a longitudinal (L) mode in which $\vec{p}$ are parallel to the chain axis. All other forms of propagation can be described as a linear combination of T and L modes. For the T modes, widely separated MNS's can interact via the far field of the scattered light; this is not possible for the L modes since there is no scattered light parallel to the dipole moment. A very thorough study on the effect of including the far field of scattered light on the dispersion relation of T modes was done by Citrin [68]. For the geometry discussed in this chapter, the light beam will be directed from left to right so only T modes are excited unless noted otherwise.

5.2 Coupled dipole method

In our calculations, we assume that the plasmon excitations caused by incident light produce an oscillating dipole electric field. This assumption holds if the wavelength of the incident light is much larger than the diameter, $2a$, of the MNS and the inter-particle distance $d \gtrsim 3a$ [48,70]. A more complete investigation of higher order multi-pole effects in the near field has been done by Park and Stroud [48]; higher order multi-pole effects become increasingly important as the inter-particle spacing decreases but should give only minor, quantitative differences for the cases we present here. The electric field produced by a single, periodically oscillating dipole with an electric dipole moment $\vec{p}$ is given by:

$$\begin{aligned} \vec{E}(\vec{p},\vec{R},k) &= \frac{1}{4\pi\varepsilon}\Big\{k^2(\hat{R}\times\vec{p})\times\hat{R}\,\frac{e^{ikR}}{R} \\ &\quad + [3\hat{R}(\hat{R}\cdot\vec{p})-\vec{p}\,]\left(\frac{1}{R^3}-\frac{ik}{R^2}\right)e^{ikR}\Big\}, \end{aligned} \tag{5.1}$$

where $k = \omega/v$ is the wavenumber in the dielectric, v is the speed of light in the dielectric medium [71], and $\hat{R}$ is the unit vector in the direction of $\vec{R}$ ($\vec{R}$ is the displacement from the dipole $\vec{p}$) [70]. If we use the near-field approximation $R \ll \lambda$, then we set $k = 0$ and the electric field is:

$$\vec{E}_{near}(\vec{p},\vec{R}) = -\frac{1}{4\pi\varepsilon}\frac{\vec{p}-3\hat{R}(\vec{p}\cdot\hat{R})}{R^3}. \tag{5.2}$$

In the near-field the electric field is dominant, but when using the full field this is not immediately obvious. We can neglect the effects of the magnetic field however, if the charge separation is small, i.e. the magnitude of the dipole is not very large compared to the total charge times the radius a on the MNS.

Using the full electric dipole fields, we can construct self-consistent equations of motion for a driven system of MNS's. The equation of motion for a dipole driven by an electric field can be parameterized as $\ddot{\vec{p}} + \gamma\dot{\vec{p}} + \omega_{SP}^2\vec{p} - \beta\dddot{\vec{p}} = \eta\vec{E}(t)$ where γ, ω_{SP}, β, and η are constants; the physical values of these parameters are substituted in the equation below. The terms of this equation have a familiar origin: the first term is the acceleration, the second term is the damping from ohmic heating, the third term is from the harmonic force, the fourth term is from radiation damping and the right hand side is the driving term from the electric field. Substituting the oscillating form, $\vec{p}_n(t) = \vec{p}_n \exp(-i\omega t)$, and substituting the physical values for the constants gives the coupled dipole-dipole equations of motion:

$$\left[-\omega^2 - i\gamma\omega + \omega_{SP}^2 - i\frac{2}{9}\left(\frac{a}{v}\right)^3 \omega_p^2\omega^3\right]\vec{p}_n = \frac{1}{3}a^3\omega_p^2 4\pi\varepsilon\left\{\vec{E}_n^{(ext)} + \sum_{n'\neq n}\vec{E}(\vec{p}_{n'}, \vec{R}_{nn'}, k)\right\} \tag{5.3}$$

where a is the radius of the MNS, $\vec{R}_{nn'} \equiv \vec{R}_{n'} - \vec{R}_n$ is the center-to-center distance between two particles, $\vec{E}_n^{(ext)}$ is external electric field at the nth nanosphere, and $\vec{E}(\vec{p}_{n'}, \vec{R}_{nn'}, k)$ has been defined as Eq.(5.2). In a previous study, the radiation damping was erroneously taken to be negligibly small [66]. For the parameters of this chapter, the radiation damping is the largest loss mechanism, but the radiation damping does become less important as the radius of the MNS's decreases. In the ohmic damping term, γ is the inverse of the electronic relaxation time. In order to match the bulk dielectric properties of silver, we use a value of $\gamma = 7.87\times10^{13}$ s^{-1} [66].

The coupling strength is determined in large part by the bulk plasmon frequency ω_p. The value of w_p has been defined such that: $\omega_p^2 = (Ne^2)/(\varepsilon m^*)$, where N is the total number of conducting electrons per unit volume, e is the charge of an electron, and m^* is the optical effective electron mass [72]. For silver we used $N = 5.85 \times 10^{28}$ electrons/m^3 and $m^* = 8.7 \times 10^{-31}$kg. We have calculated a value of $\omega_p \sim 9.3 \times 10^{15}$ rad/s, and we will use $\omega_{SP} \sim 5 \times 10^{15}$ rad/s [66]. The solutions to these coupled inhomogeneous linear algebra equations are the induced dipole moments, $\vec{p}$, on each sphere. Because $\vec{p}$ appears linearly, these coupled equations can be solved directly by using standard linear algebra packages.

5.3 Results

The MNS's act as both scatterers and detectors of the total electromagnetic field. The induced dipole moment of an MNS is proportional to the local electric field, while the ohmic power dumped into the MNS is proportional to the magnitude of the dipole moment squared. In Fig. 5.2 the ohmic power of each of the ten individual MNS is plotted for two specific frequencies: one placing most of the power on the first MNS and the other directing most of the power down the chain. In both cases the magnitude of the incident electric field is chosen to be 1 V/m to facilitate (through linear scaling) the calculation of the power at other field strengths. The dramatic difference in the distribution of power with relatively small changes in frequency is evident. The near field approximation has been used in many studies of interacting MNS's, but does not correctly reproduce most effects in Fig. 5.2. The near-field

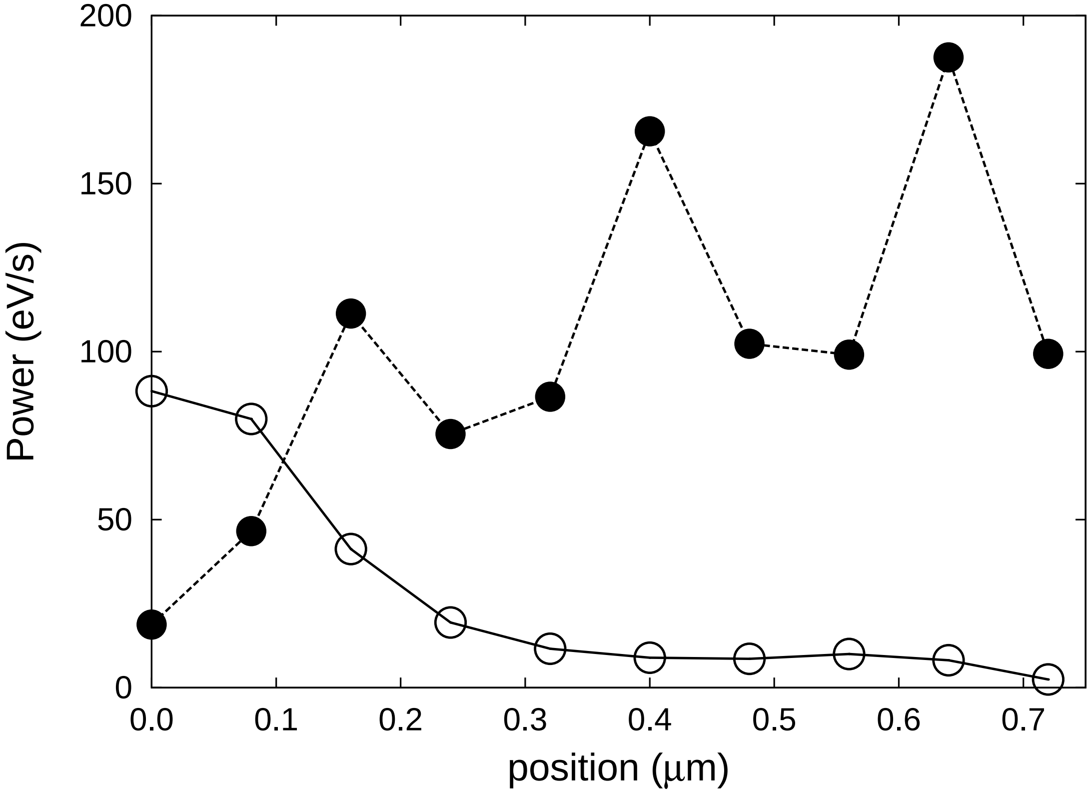

Figure 5.2: The ohmic power as a function of the position of 10 MNS's in a regularly spaced linear array. The center-to-center inter-particle distance is $d = 80$ nm and the diameter, $2a$, of each MNS is 50 nm. A plane transversely polarized electromagnetic wave is propagated from left to right along the axis of the array. All of the MNS's absorb and scatter the incident electromagnetic wave of magnitude 1 V/m. The solid line is for a chosen frequency $\omega = 4.85 \times 10^{15}$ rad/s ($\lambda_{\text{diel}} = 259$ nm) when most of the power is in the first sphere. The dashed line is for a frequency of $\omega = 4.62 \times 10^{15}$ rad/s ($\lambda_{\text{diel}} = 272$ nm) when most of the power is in the last sphere. This asymmetry between first and last MNS's vanishes in the near field approximation at all wavelengths.

approximation is most accurate when $kd \ll 1$, d being the regular center-to-center inter-particle distance. In the case of silver nanospheres, $\omega_{SP} \sim 5 \times 10^{15}$ rad/s which gives a value of $k \sim 3.0 \times 10^{7}$ m^{-1} in the dielectric. Typical inter-particle spacings are in the range of 80 nm, so in these cases $kd \sim 2\pi/3$. In the near-field approximation, coupling terms that fall off as R^{-1} and R^{-2} are neglected. When using the full electric field, certain phase dependent phenomena are now taken into account that have been overlooked in earlier work [66]. It is important to recognize that the dipole fields created by the now oscillating electric dipoles have individual phases that vary with the distance from an MNS. The retarded electric field can either add constructively or destructively down the chain to create localized regions of high total electric field. Using the near field approximation, all of the MNS's interact with each other instantaneously and any phase is solely due to the phase of oscillation of a single dipole. Using this approximation, the ohmic power is symmetric through the midpoint of the array at all wavelengths. In contrast when using the full dipole field there is a lag in inter-particle communication due to the finite speed of light. It is this lag that allows the MNS's to have differing phases that can coherently add or subtract at specific locations in space.

It is also interesting to compare the ohmic power of the first MNS to the last one while scanning over a range of frequencies. Remember that in our geometry the light is directed down the line of MNS's. Therefore, without the interaction between MNS's, each of the nanospheres would dissipate the same amount of ohmic power.

It can immediately be seen in Fig. 5.3 that within a certain band of frequencies the ohmic power from sphere one is much greater than that of the last one.

Within another band of frequencies the opposite is true. A similar though lesser effect is present even for the limit of two MNS's. In order to clearly illustrate the sensitivity of the array we also plotted the single particle response to an identical beam of light in Fig. 5.3 as dotted lines. Note that the response of the first MNS follows the response of a single sphere when the driving frequency is far off resonance, but the response of the last sphere is strongly suppressed for all of the plotted frequencies greater than resonance. This forward-backward asymmetry is not present when the near-field approximation is used (inset of Fig. 5.3), and thus the asymmetry is due solely to the retardation of the electric field. It is also interesting that the power in the first sphere is greater than for a single sphere for almost all frequencies and is roughly a factor of 3 times larger at the peak.

Naturally the next step is to investigate what is the cause of the forward-backward frequency dependent asymmetry as seen in Fig. 5.3. Using the calculated dipole moments and looking in the far field ($r \to \infty$) limit we can determine the differential radiated power per solid angle [70]:

$$\frac{d\mathcal{P}_{rad}}{d\Omega} = \frac{1}{2}\frac{vk^4}{(4\pi)^2\varepsilon}[\,|\vec{P}|^2 - |\hat{r}\cdot\vec{P}|^2], \tag{5.4}$$

where

$$\vec{P} \equiv \sum_n \vec{p}_n \, e^{-ik\hat{r}\cdot\vec{\Delta}_n} \tag{5.5}$$

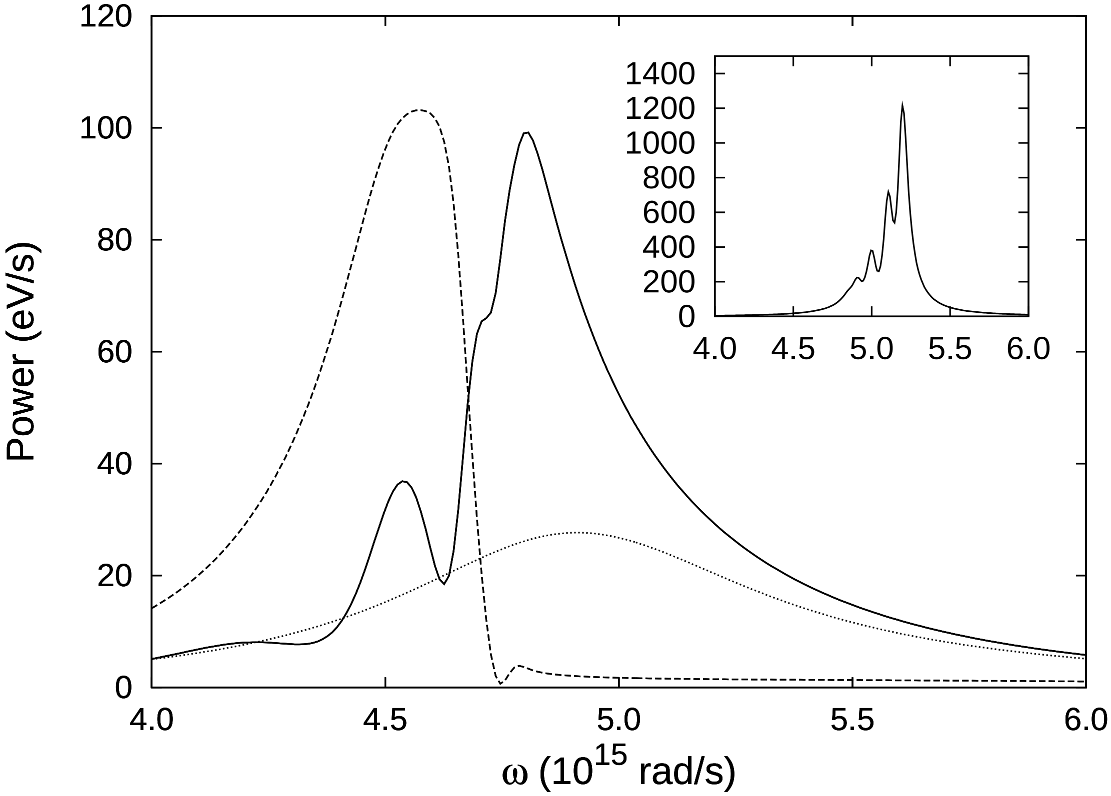

Figure 5.3: The ohmic power as a function of the frequency, ω, of a plane electromagnetic wave propagating along the axis of a regular linear array of MNS's. The dimension of the array and MNS's is the same as in Figs. 5.1 and 5.2. All of the MNS's absorb and scatter the incident beam of light as it comes in from left to right. The solid line is the ohmic power of the first (leftmost) MNS and the dashed line is for the last (tenth) one. The dotted line is the power response for the single MNS case. The inset is the same as the main figure, but using only the near field approximation. Note that it is now impossible to preferentially excite the first or last MNS by modifying the driving frequency.

and $k = \omega/v = 2\pi/\lambda$ is the wavenumber in the dielectric medium. In Eqs. (5.4) and (5.5), $\hat{r}$ is the usual radial unit vector, $\vec{\Delta}_n$ is the displacement from the the first nanosphere to the n^{th} one, and $|\vec{\Delta}_n| = (n-1)d$ for a regularly spaced linear array.

We set up a regular linear array as in Fig. 5.1, but we changed the simulation so that only the first (leftmost) MNS is excited to a frequency ω. Exciting a single MNS can probably be realized by using an electron beam instead of optical radiation. Optical spot sizes are of at least the order of λ in dielectric, while e-beams can have spot sizes much smaller than the inter-particle separation d. We can see in Fig. 5.4 that there are indeed certain bands of frequency that cause the whole system to scatter light in the backward direction and that these frequencies are the same frequencies where the forward-backward asymmetry is realized. In fact the similarity between Figs. 5.3 and 5.4 is quite pronounced showing that the asymmetric behavior is caused by the coherent constructive or destructive interference of the radiated light from the individual MNS. When driving the first MNS at certain frequencies, the total electric field emitted by the MNS's add constructively along the line which correlates with a large amplitude at the last sphere. At other frequencies, the total electric field gives destructive interference along the line which correlates with the small amplitudes at the final sphere.

Another way to look at Fig. 5.4 is to perform a discrete Fourier transform of the induced dipole moments: $\vec{p}(k) = \sum_n \vec{p}(\hat{r}\cdot\vec{\Delta}_n)\exp(-ik\hat{r}\cdot\vec{\Delta}_n)$. We examined $p(k)$ at various ω's by starting from about 4.0×10^{15} rad/s and increasing the frequency. At first a clear peak could be seen in $p(k)$ and this peak increased as we increased ω.

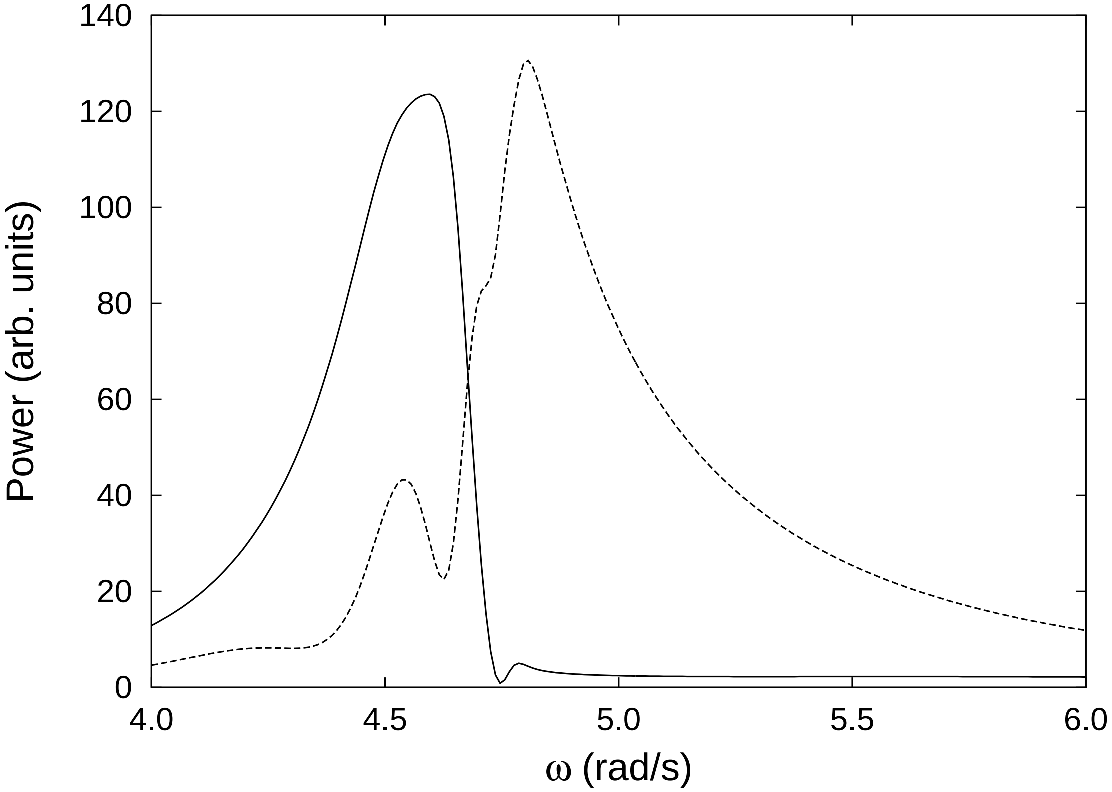

Figure 5.4: The same physical set up as Fig. 5.2, but this time only the first sphere is externally excited. Plotted is the differential radiated power per solid angle versus the frequency of the incident light. The solid line is the power scattered in the forward direction and the dashed line is the power scattered in the backward direction.

At around $\omega \sim 4.8 \times 10^{15}$ rad/s a clear peak could no longer be discerned, and $p(k)$ becomes very noisy. This implies that above about $\omega \sim 4.8 \times 10^{15}$ rad/s we are trying to drive the system outside the allowed photonic bands. This behavior matches closely with Fig. 5.4, suggesting that scattering light in the forward direction is suppressed due to driving within the photonic bandgap for this system. It also suggests that a correct band structure calculation must take into account the full electric dipole field and radiative damping.

When exciting the system into L modes, widely separated MNS's do not interact via the far field of the scattered light ($\hat{R} \times \vec{p} = 0$). They do still communicate through the near and intermediate fields. Unlike using the near field approximation, however, the scattered field is still retarded. This retardation will once again cause MNS's to oscillate at various phases allowing for interference effects. In Fig. 5.5 we again use the same physical set up as Fig. 5.1, and we only excite the leftmost MNS at a various frequencies ω. This time we excite into an L mode (parallel to the chain). Plotted in Fig. 5.5 is the differential power scattered per solid angle ($d\mathcal{P}/d\Omega$) versus the scattering angle θ at two different frequencies. The inset is also $d\mathcal{P}/d\Omega$, but forcing all of the MNS's to oscillate in phase. This plot is reminiscent of the symmetric diffraction pattern of light passing through slits spaced closely relative to the incident wavelength. A clear asymmetry however, can be seen in the main plot. As seen with the T mode case, the bulk of the scattered light can be preferentially aimed in different directions by adjusting the frequency of the driving force.

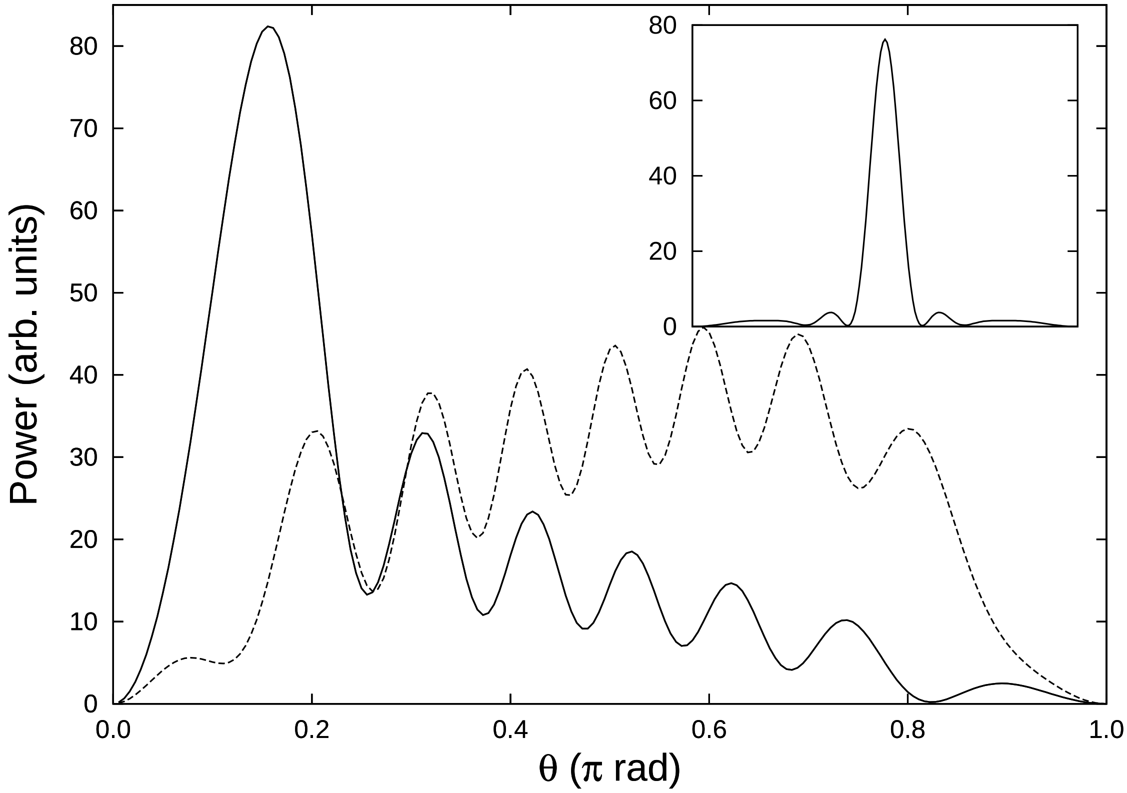

Figure 5.5: Again the same physical set up as Fig. 5.4, but this time the first sphere is externally excited into an L mode. Plotted is the differential radiated power per solid angle versus the scattering angle θ for two frequencies, where θ is the angle relative to the line of MNS's. The solid line is the power scattered at $\omega = \omega_{SP} = 5.0 \times 10^{15}$ rad/s and the dashed line is the power scattered when $\omega = 5.5 \times 10^{15}$ rad/s. In order to more cleary show the asymmetry the dashed line is scaled by 2.0 i.e the amplitude of the driving force is increased by about 40%. The intermediate electric field of the oscillating dipoles gives the asymmetry. The inset also plots differential radiated power per solid angle versus the scattering angle for $\omega = \omega_{SP}$, but here the MNS's are forced to oscillate in phase.

5.4 Conclusion

In summary, we have shown that when looking at a system of MNS's, interesting effects can be lost when using only a near-field approximation. Within certain closely spaced bands of frequencies it is possible, using a spatially broad beam of light, to excite specific MNS's. In Fig. 5.3, the ratio of the power in the first sphere to that in the last sphere is 1 near the crossing frequency $\sim 4.7 \times 10^{15}$ rad/s; near this frequency, the ratio varies by more than an order of magnitude in a small range of frequencies. Various experimental techniques can detect when the surface plasmon of an MNS is excited; thus, it seems possible to distinguish between two nearby wavelengths in a small frequency range near $\sim 4.7 \times 10^{15}$ rad/s using a device less than 1 μm in size.

Exciting the surface plasmon in a particular MNS is closely related to the frequencies where the whole system exhibits a large amount of forward or backward scattering of light. This pronounced forward and backward scattering is caused within specific ranges of frequency that allow the collection of MNS's to constructively or destructively add their radiated light. This behavior has exciting experimental consequences such as being able to infer the ohmic power dissipated in an MNS by looking at the scattered light field. Rather than having to coat the MNS's with specific dyes to measure their output power, it should be possible to simply detect the amount of forward and back scattered light.

The retardation of the incident and scattered light field removes the symmetry through the middle of the line of nanospheres allowing a range of complex phenomena.

Only a few of these effects have been discussed in this chapter; many variations have not yet been explored and will probably disclose more fascinating results.

Chapter 6

Summary

In this dissertation, we explored the effects of many body dipole interactions. Primarily we studied the long range interactions between groups of Rydberg atoms since the large size of the Rydberg atoms allowed for the creation of large dipole moments. The dipole moments were either created via a second order interaction between excited atoms in a field free environment or induced via a first order interaction such as being placed in a static electric field. When using the second order case, or van Der Waals, the interaction between Rydberg atoms fell off as $1/R^6$, and when using the the first order case the interaction fell off as $1/R^3$. In both cases, the excitations in the system were tracked by solving the time dependent Schrödinger equation numerically. We also looked at a classical system of interacting dipole moments and calculated the power absorbed and emitted by each classical dipole.

6.1 Dipole blockade

The first effect studied in this dissertation was the dipole blockade. A dipole blockade is seen when the interactions between nearby Rydberg atoms push the system out of resonance with a tightly tuned excitation laser, and the total number of excitations is suppressed. We developed a many body wavefunction approach that allowed us to study two particle correlations, number correlations via the Mandel Q-parameter, how the excitations fill space, and the possible use of Rydberg atoms in a phase gate. This many body wavefunction was used with the time-dependent Schrödinger equation and solved numerically by using the split operator method.

The 2D two particle correlation function clearly illustrated the existence of a minimum distance between atoms at which multiple excitations were possible. In the first order dipole-dipole case, the region defined by this minimum distance, R_b, is dependent on the angle of orientation between atoms. There is a critical angle, $\theta \approx 55^\circ$, where the dipole interaction between pairs of atoms vanishes, and it is possible for two nearby atoms along this angle to both become excited. If a well defined blockade region is desired then special care must be taken to exclude any pairs of atoms from the excitation region that might be situated close to the critical angle.

The Mandel Q-parameter was a useful quantity for measuring the degree to which a group of Rydberg atoms were blockaded and how well correlated the system is. Our calculations of the Q-parameter showed the level of correlation increased as the density of the system was increased. Even with very few excitations, if the gas of atoms was dense enough, the system was still well correlated. This was a result of the non-excited atoms within a blockade region still affecting atoms outside of R_b.

We learned that if the atoms are placed on a regular linear lattice, the maximum number of allowed excitations grows smoothly as the length of the lattice is increased. We did not see a sudden jump from one excited atom to two excited atoms which indicated that a bubble picture for excitations is not correct. The size of R_b was seen when the probability of being in a state with a specific number excited was plotted as a function of chain length. This plot also explained the smoothness seen in the maximum number of possible excitations versus chain length. Our results also clearly demonstrated the sub-Poissonian nature of the correlated system.

One of the bigger advantages to solving the many body wavefunction as opposed to a mean field or Monte Carlo approach was that it allowed us to keep track of phase changes. We examined the use of blockaded atoms as qubits in a phase gate. We simulated a well defined collection of Rydberg atoms as qubits, and calculated the phase accumulated after a series of pulses. We compared a perfectly functioning phase gate to the non-perfect case and discovered that in order for the generated errors to be small the interaction energy between the two qubits must be rather large.

We also performed three very different model calculations of a gas or Rydberg atoms in the strongly blockaded regime: the many body wavefunction model using pseudoparticles, a simple sinusoidal model, and a Monte Carlo model. In this regime the density of atoms is much higher than in previous simulations. In this case we were simulating around of 1.5×10^7 atoms. The three models were all in good qualitative agreement with each other and within a factor of 2 in both N_{exc} and saturation time. For such a large number of atoms this was encouraging, but the calculations were not in agreement enough with experimental data to suggest that the physics of the system was completely understood. We were unable to take into account the variations in density over R_b present in the experimental parameters of the MOT, and we believe that in order for a theoretical model to accurately simulate this experiment this density variation must be taken into account. This would present an imposing challenge to any mean field model since the value of the mean field energy shift of an atom would also have to vary with the location of the atom in the MOT. Nonetheless our studies still provided a useful tool in studying some of the many body effects present in a strongly blockaded regime.

6.2 Coherent hopping of excitation

In Chapter 3, we studied the coherent energy exchange between Rydberg atoms. This exchange of character between two atoms is possible when the energy cost for such a transition is very small. The coupling that regulates this hopping of states is a dipole interaction that falls off as $1/R^3$. We examined two distinct cases where atoms are excited into Rydberg states that allow a resonant exchange of energy to occur via a dipole transition: the hopping from an $|sp\rangle$ state to a $|ps\rangle$ state in a field-free environment and the hopping among the highest Stark states ($|n_1 n_2\rangle \rightarrow |n_2 n_1\rangle$) in a static electric field. In the second case we proposed a realistic experimental setup that has been attempted. We simulated the coherent hopping of excitation by using an essential states model that included only states that are degenerate or nearly degenerate in our calculations.

In the field free situation we placed a single s Rydberg atom in a sea of regularly placed p Rydberg atoms. We then solved the time-independent Schrödinger equation to generate band structures for various geometries. The band structure for a linear array of of Rydberg atoms was remarkably similar to what is seen in the bands for a line of driven metallic nanospheres. There were three modes of propagation: two degenerate bands (the lobes of the hopping p state perpendicular to the array axis) and one nondegenerate band (the lobes of the p state parallel to the array axis). The band structures also allow us to label the nature of the p state hopping as either particle-like or hole-like. When the geometry was expanded to two dimensions, phonon-like hopping was also seen in the bands. In three dimensions the band structure becomes feature-rich for such a simple system, with holes, particles, and many degenerate modes of hopping.

We proposed an experimental setup consisting of Rydberg atoms placed into high Stark states by a static electric field. In this case one atom is excited to an $n = 61$ Stark state in an array of $n = 60$ Stark states. We simulated this system as it evolved in time by numerically solving the time-dependent Schrödinger equation via an exponential propagator. Since the perfect placement of atoms is not experimentally viable, we randomly placed each atom in a number of separated regions and averaged our results over a large number of geometries. Our simulations indicated that the coherent hopping of the $n = 61$ state should still last for substantial time scales. We also simulated a case where the non-uniformity of the atoms was severe enough for a region to be empty, and our results showed that while coherence of the system is not destroyed, the $n = 61$ state is unable to hop across the hole in the chain of atoms.

6.3 The effects of rotary and spin echo sequences on a Rydberg gas

We next studied the effects of using echo sequences on a Rydberg gases. In the first part of chapter 4 we simulated the rotary echo signal of an ultracold Rydberg gas in the strongly blockaded regime. While in the second part we examined the spin echo signal of a Rydberg gas that allowed for a coherent hopping of state to occur. A rotary echo is accomplished in a frozen Rydberg gas by reversing the sign of the excitation mechanism after a length of time τ_p. When τ_p is exactly half of the total excitation time τ and there is no significant source of outside decoherence, a strong signal should appear reflecting that the system has been returned to its initial configuration. A spin echo is performed by exciting a gas using a $\pi/2$ pulse, letting it relax for set time, exciting it again with a π pulse, letting it relax again for second amount of time, and finally deexciting it with a final $\pi/2$ pulse. When the two relaxation times are equal and outside sources of decoherence are again small, the gas should be returned to its initial state. We simulated the first case by using the many-body pseudoparticle wavefunction approach and the split operator method to numerically solve the time-dependent Schrödingder equation. The second case was solved by diagonalizing the interaction Hamiltonian and using an exponential propagator to numerically simulate the evolution of the many-body wavefunction.

For the rotary echo case, a strong echo signal means the gas of Rydberg atoms has been returned to a state with very few excitations. In fact if the system is perfectly blockaded, our results show that the system should exhibit a perfect echo where no excitations are present when $\tau_p = \tau$. This is a result of the entire collection of atoms oscillating in a coherent manner, and analagous to an isolated superatom. A more interesting situation arose when the system was not completely blockaded, and the interactions between pseudoparticles lead to dephasing and a supression of the echo signal. As the density was increased the echo signal was weakened. If the van der Waals interaction between pseudoparticles was also reversed in sign at the same time the excitation amplitude reverses sign, a perfect echo is again seen. We offered a system that might possibly allow for the force between Rydberg atoms to be switched from attractive to repulsive.

Our simulations of the spin echos showed that if only one hopper is present, and the thermal motion of the gas is ignored then a perfect spin echo signal will always be seen when the relaxtion times are equal. The effect of thermal motion is very small when the relaxation times are short enough to only allow a couple of hops to occur. When four or more hops are allowed, however, the spin echo signal is destroyed for temperatures greater than 300 μK. The increase in the number of allowed hops leads to the increase in the number of atoms that contribute to the dephasing.

6.4 Interactions between classical dipole moments: nanospheres

In chapter 5 we investigated the response of a system of metallic nanospheres (MNSs) to a driving electric field. When excited by a tuned beam of light, the surface plasmon on a MNS behaves as an oscillating dipole moment. In turn, these oscillating dipoles generate their own time-dependent electric fields which interact with other MNS. We reported several interesting effects that arise from this simple system when the full electric field from the oscillating dipoles was used rather than just using the near field approximation. In order to describe this system of driven oscillating dipoles we developed a coupled point dipole model where each MNS is treated as a point dipole that responds linearly to an electric field. For our results we used up to ten Ag MNSs.

When all of the MNSs are placed in a linear array and are equally illuminated by a beam of light, the power deposited in a particular MNS strongly depends on its position in the system and the frequency of the driving electric field. In fact, the ratio of the power dumped into the first MNS and the last MNS can be inverted by making small changes in the frequency of the excitation beam. This effect is not seen when the near field approximation is used because retardation of the scattered full field introduces interference. The retardation of the scattered light removes the symmetry through the middle of a line of MNS allowing a range of complex effects. Our simulations showed the possibility of taking advantage of effects through exciting experimental realizations such as finely tuned frequency discrimination and nanolithography.

Bibliography

[1] T. F. Gallagher, *Rydberg Atoms* (Cambridge University Press, New York 1994).

[2] "Resonant Rydberg-Atom-Rydberg-Atom Collisions", K. A. Safinya, J. F. Delpech, F. Gounand, W. Sander, and T. F. Gallagher, Phys. Rev. Lett. **47**, 405 (1981).

[3] "Spectral line broadening due to the interaction between very excited atoms: 'the dense Rydberg gas'", J. M. Raimond, G. Vitrant, and S. Haroche, J. Phys. B: At. Mol. Phys. **14**, L655 (1981).

[4] "Fast Quantum Gates for Neutral Atoms", D. Jaksch, J. I. Cirac, P. Zoller, S. L. Rolston, R. Côté, and M. D. Lukin, Phys. Rev. Lett. **85**, 2208 (2000).

[5] "Applicability of Rydberg atoms to quantum computers", I. I. Ryabtsev, D. B. Tretyakov, and I. I. Beterov, J. Phys. B: At. Mol. Phys. **38**, S421 (2005).

[6] "Analysis of a quantum logic device based on dipole-dipole interactions of optically trapped Rydberg atoms", M. Saffman and T. G. Walker, Phys. Rev. A **72**, 022347 (2005).

[7] "Operation of a quantum phase gate using neutral atons in microscopic dipole traps", I. E. Protsenko, G. Reymond, N. Schlosser, and P. G. Grangier, Phys. Rev. A **65**, 052301 (2002).

[8] "Resonant Dipole-Dipole Energy Transfer in a Nearly Frozen Rydberg Gas", W. R. Anderson, J. R. Veale, and T. F. Gallagher, Phys. Rev. Lett. **80**, 249 (1998).

[9] "Many-Body Effects in a Frozen Rydberg Gas", I. Mourachko, D. Comparat, F. de Tomasi, A. Fioretti, P. Nosbaum, V. M. Akulin, and P. Pillet, Phys. Rev. Lett. **80**, 253 (1998).

[10] "Colloquium: Trapping and manipulating photon states in atomic ensembles", M. D. Lukin, Rev. Mod. Phys. **75**, 457 (2003).

[11] C. Cohen-Tannoudji, *Quantum Mechanics: Volume II* (Hermann and John Wiley & Sons, Paris, France 1977).

[12] "Long-Range Forces between Cold Atoms", A. Fioretti, D. Comparat, C. Drag, T. F. Gallagher, and P. Pillet, Phys. Rev. Lett. **82**, 1839 (1999).

[13] "Dipole Blockade and Quantum Information Processing in Mesoscopic Atomic Ensembles", M. D. Lukin, M. Fleischhauer, R. Côté, L. M. Duan, D. Jaksch, J. I. Cirac, and P. Zoller, Phys. Rev. Lett. **87**, 037901 (2001).

[14] "Local Blockade of Rydberg Excitation in an Ultracold Gas", D. Tong, S. M. Farooqi, S. Krishnan, Y. P. Zhang, R. Côté, E. E. Eyler, and P. L. Gould, Phys. Rev. Lett. **93**, 063001 (2004).

[15] "Supression of Excitation and Spectral Broadening Induced by Interactions in a Cold Gas of Rydberg Atoms", K. Singer, M. Reetz-Lamour, T. Amthor, L. G. Marcassa, and M. Weidemüller, Phys. Rev. Lett. **93**, 163001 (2004).

[16] "Spectroscopy of an ultracold Rydberg gas and signatures of Rybderg-Rydberg interactions", K. Singer, M. Reetz-Lamour, T. Amthor, S. Fölling, M. Tscherneck, and M. Weidemüller, J. Phys. B **38** (2005). S295.

[17] "Electric-Field Induced Dipole Blockade with Rydberg Atoms" T. Vogt, M. Viteau, A. Chiota, J. Zhao, D. Comparat, and P. Pillet, Phys. Rev. Lett. **99**, 073002 (2007).

[18] "Dipole Blockade at Förster Resonances in High Resolution Laser Excitation of Rydberg States of Cesium Atoms", T. Vogt, M. Viteau, J. Zhao, A. Chiota, D. Comparat, and P. Pillet, Phys. Rev. Lett. **97**, 083003 (2006).

[19] "Atom Counting Statistics in Ensembles of Interacting Rydberg Atoms", T. Cubel Liebisch, A. Reinhard, P. R. Berman, and G. Raithel Phys. Rev. Lett. **95**, 253002 (2005).

[20] "Rydberg Excitation of Bose-Einstein Condensates", R. Heidemann, U. Raitzsch, V. Bendkowsky, B. Butscher, R. Löw, and T. Pfau, Phys. Rev. Lett. **100**, 033601 (2008).

[21] "Many-body wave function in a dipole blockade configuration", F. Robicheaux and J. V. Hernández, Phys. Rev. A **72**, 063403 (2005).

[22] "Mechanical Effect of van der Waals interactions Observed in Real Time in an Ultracold Rydberg Gas", T. Amthor, M. Reetz-Lamour, S. Westermann, J. Denskat, and M. Weidemüller, Phys. Rev. Lett. **98**, 023004 (2007).

[23] "Strong interaction effects on the atom counting statistics of ultracold Rydberg gases", C. Ates, T. Pohl, and J. M. Rost, J. Phys. B: At. Mol. Opt. Phys. **39**, L233 (2006).

[24] "Many-body theory of excitation dynamics in an ultracold Rydberg gas", C. Ates, T. Pohl, T. Pattard, and J. M. Rost, Phys. Rev. A **76**, 013413 (2007).

[25] "Level shifts of rubidium Rydberg states due to binary interactions", A. Reinhard, T. Cubel Liebisch, B. Knuffman, and G. Raithel, Phys. Rev. A **75** 032712, (2007).

[26] "Simulation of coherent interactions between Rydberg atoms", F. Robicheaux, J. V. Hernández, T. Topçu, and L. D. Noordam, Phys. Rev. A **70**, 042703 (2004).

[27] "Creating aingle-atom and simgle-photon sources from entangled atomic ensembles", M. Saffman and T. G. Walker, Phys. Rev. A **66**, 065403 (2002).

[28] "Rydberg-Rydberg Collisions: Resonant Enhancement of State Mixing and Penning Ionization", A. Reinhard, T. Cubel Liebisch, K. C. Younge, P. R. Berman, and G. Raithel, Phys. Rev. Lett. **100**, 123007 (2008).

[29] "Dephasing of resonant energy transfer in a cold Rydberg gas", W. R. Anderson, M. P. Robinson, J. D. D. Martin, and T. F. Gallagher, Phys. Rev. A **65**. 063404 (2002).

[30] "Spatially resolved observation of dipole-dipole interactions between Rydberg atoms", C. S. E. van Ditzhuijen, A. F. Koenderink, J. V. Hernández, F. Robicheaux, L. D. Noordam, and H. B. van Linden van Heuvell, accepted Phys. Rev. Lett. (2008).

[31] "Back and Forth Transfer and Coherent Coupling in a Cold Rydberg Dipole Gas", M. Mudrich, N. Zahzam, T. Vogt, D. Comparat, and P. Pillet Phys. Rev. Lett. **95**, 233003 (2005).

[32] "Angular Dependence of the Dipole-Dipole Interaction in a Nearly One-Dimensional Sample of Rydberg Atoms", T. J. Carroll, K. Claringbould, A. Goodsell, M. J. Lim, and M. W. Noel, Phys. Rev. Lett **93**, 153001 (2004).

[33] "Resonant electric dipole-dipole interactions between cold Rydbeg atoms in a magnetic field", K. Afrousheh, P. Bohlouli-Zanjani, J. D. Carter, A. Mugford, and J. D. D. Martin, Phys. Rev. A **73**, 063403 (2006).

[34] "Resonance optics of the low-temperature quantum gases H and D", B. V. Svistunov and G. V. Shlyapnikov, Sov. Phys. JETP **70**, 460 (1990).

[35] "Quantum networks: When superatoms talk photons" V. Vuletic, Nature Phys **2**, 801 (2006).

[36] "Echo Experiments in a Strongly Interacting Rydberg Gas" U. Raitzsch, V. Bendkowsky, R. Heidemann, B. Butscher, R. Löw, and T. Pfau, Phys. Rev. Lett. **100**, 013002 (2008).

[37] "Spin Echoes", E. L. Hahn, Phys. Rev. **80**, 580 (1950).

[38] "Rotary Spin Echoes", I. Solomon, Phys. Rev. Lett. **2**, 301 (1959).

[39] "Fast quantum state control of a single trapped neutral atom", M. P. A. Jones, J. Beugnon, A. Gäetan, J, Zhang, G. Messin, A. Browaeys, and P. Grangier, Phys. Rev. A **75**, 040301 (2007).

[40] U. Kreibig and M. Vollmer, *Optical Properties of Metal Clusters* (Springer-Verlag, Berlin, 1994).

[41] "Light-Induced Coherent Interactions between Silver Nanoparticles in Two-Dimensional Arrays", S. Malynych and G. Chumanov, J. Am. Chem. Soc. **125**, 2896 (2002).

[42] "The Bakerian Lecture: Experimental Relations of Gold (and Other Metals) to Light", M. Faraday, Philos. Trans. **147**, 145 (1857).

[43] "Programmable nanolithography with plasmon nanoparticle arrays", A. F. Koenderink, J. V. Hernández, F. Robicheaux, L. D. Noordam, and A. Polman, Nan letters **7**, 745 (2007).

[44] "Self-Similar Chain of Metal Nanospheres as an Efficient Nanolens", K. Li, M. I. Stockman, and D. J. Bergman, Phys. Rev. Lett. **91**, 227402 (2003).

[45] "Surface Plasmon Amplification by Stimulated Emission of Radiation: Quantum Generation of Coherent Surface Plasmons in Nanosystems", D. J. Bergman and M. I. Stockman, Phys. Rev. Lett. **90**, 027402 (2003).

[46] "Local detection of electromagnetic energy transport below the diffraction limit in metal nanoparticle plasmon waveguides", S. A. Maier, P. G. Kik, H. A. Atwater, S. Meltzer, E. Harel, B. E. Koel, and A. A. Requicha, Nature Materials **2**, 229 (2003).

[47] "The Optical Properties of Metal Nanospheres: The Influence of Size, Shape, and Dielectric Environment", K. L. Kelly, E. Coronado, L. L Zhao, and G. C. Schatz, J. Phys. Chem. B **107**, 668 (2003).

[48] "Surface-plasmon dispersion relations in chains of metallic nanoparticles: An exact quasistatic calculation", S. Y. Park and D. Stroud, Phys. Rev. B **69**, 125418 (2004).

[49] "Electromagnetic energy transport via linear chains of silver nanoparticles", M. Quinten, A. Lietner, J. R. Krenn, and F. R. Aussenegg, Opt. Lett. **23**, 1331 (1998).

[50] "Evidence for Coherent Collective Excitation in the Strong Blockade Regime", R, Heidemann, U. Raitzsch, V. Bendkowsky, B. Butscher, R. Löw, L. Santon, and T. Pfau, Phys. Rev. Lett. **99**, 163601 (2007).

[51] "Long-Range Molecular Resonances in a Cold Rydberg Gas", S. M. Farooqi, D. Tong, S. Krishnan, J. Stanojevic, Y. P. Zhang, J. R. Ensher, A. S. Estrin, C. Boisseau, R. Côté, E. E. Eyler, and P. L. Gould, Phys. Rev. Lett. **91**, 183002 (2004).

[52] "Spectroscopic Observation of Resonant Electric Dipole-Dipole Interactions between Cold Rydberg Atoms", K. Afrousheh, P. Bohlouli-Zanjani, D. Vagale, A. Mungford, M. Fedorov, and J. D. D. Martin, Phys. Rev. Lett. **93** 233001 (2004).

[53] "Long-range interactions between alkali Rydberg atom pairs correlated to the *n*s-*n*s, *n*p-*n*p, and *n*d-*n*d asymptotes", K. Singer, J. Stanojevic, M. Weidemüller, and R. Côté, J. Phys. B: At. Mol. Opt. Phys. **38**, S295 (2005).

[54] "Dispersion coefficients for the *n*P-*n*P asymptote of homonuclear alkali-metal dimers", M. Marinescu, Phys. Rev. A **56**, 4764 (1997).

[55] "Millimeter-wave spectroscopy of cold Rb Rydberg atoms in a magneto-optical trap: Quantum defects of the ns, np, and nd series", W. Li, I. Mourachko, M. W. Noel, and T. F. Gallagher, Phys. Rev. A **67** 052502 (2003).

[56] D. M. Brink and G. R. Satchler, *Angular Momentum* Third Edition (Oxford University Press, New York 1993).

[57] "Sub-Poissonian photon statistics in resonance fluorescence", L. Mandel, Opt. Lett. **4**, 205 (1979).

[58] W. H. Press, S. A. Teukolsky, W. T. Vetterling, B. P. Flannery, *Numerical Recipes 3^{rd} Edition* (Cambridge University Press, New York, 2007).

[59] "Level-band problem and many-body effects in cold Rydberg atoms", V. M. Akulin, F. de Tomasi, I. Mourachko, and P. Pillet, Physica D **131**, 125 (1999).

[60] "Resonant processes in a frozen gas" J. S. Frasier, V. Celli, and T. Blum, Phys. Rev. A **59**, 4358 (1999).

[61] E. Merzbacher, *Quantum Mechanics*, 3^{rd} Edition (John Wiley and Sons, New York, 1998).

[62] "Optical pulse propagation in metal nanoparticle chain waveguides", S. A. Maier, P. G. Kik, and H. A. Atwater, Phys. Rev. B **67**, 205402 (2003).

[63] "Direct observation of localized surface plasmon coupling", J. R. Krenn, J. C. Weeber, A. Dereux, E. Bourillot, J. P. Goudonnet, B. Schider, A. Leitner, F. R. Aussenegg, and C. Girard Phys. Rev. B **60**, 5029 (1999).

[64] "Electrically controlled light scattering with single metal nanoparticles", J. Müller, C. Sönnichsen, H. von Poschinger, G. von Plessen, T. A. Klar, and J. Feldmann App. Phys. Lett. **81**, 171 (2002).

[65] "Tailoring the Ultrafast Dephasing of Quasiparticles in Metallic Photonic Crystals", T. Zentgraf, A. Christ, J. Kuhl, and H. Giessen, Phys. Rev. Lett **93**, 243901 (2004).

[66] "Electromagnetic energy tranfer and switching in nanoparticle chain arrays below the diffraction limit", M. L Brongersma, J. W. Hartman, and H. A. Atwater, Phys. Rev. B **62**, R16356 (2000).

[67] "Plasmon Polaritons in Finite-Length Metal-Nanoparticle Chains: The Role of Chain Length Unravelled" D. S. Citrin, Nanoletters **5**, 985 (2005).

[68] "Coherent Excitation Transport in Metal-Nanoparticle Chains", D. S. Citrin, Nanoletters **4**, 1561 (2004).

[69] " Fluorescence resonant energy transfer in the optical near field" G. Colas des Francs, C. Girard, and O. J. F. Martin, Phys. Rev. A **2003**, *67*, 053805.

[70] J. D. Jackson, *Classical Electrodynamics*, 3rd ed. (John Wiley & Sons, Inc., 1999).

[71] We will use an index of refraction $n = 1.5$ (the general phenomena in this chapter do not depend on n).

[72] "Optical Constants of the Noble Metals", P. B. Johnson, R. W. and Christy, Phys. Rev. B **6**, 4370 (1972).